TU Delft

Delft University of Technology

Photonic topological edge states

A nanoscale investigation

Arora, S.

DOI
10.4233/uuid:f9c4d874-92cc-4a45-bd2f-a37f98f8fb78

Publication date
2023

Document Version
Final published version

Citation (APA)
Arora, S. (2023). *Photonic topological edge states: A nanoscale investigation*. [Dissertation (TU Delft), Delft University of Technology]. https://doi.org/10.4233/uuid:f9c4d874-92cc-4a45-bd2f-a37f98f8fb78

Important note
To cite this publication, please use the final published version (if applicable).
Please check the document version above.

Copyright
Other than for strictly personal use, it is not permitted to download, forward or distribute the text or part of it, without the consent of the author(s) and/or copyright holder(s), unless the work is under an open content license such as Creative Commons.

Takedown policy
Please contact us and provide details if you believe this document breaches copyrights.
We will remove access to the work immediately and investigate your claim.

This work is downloaded from Delft University of Technology.
For technical reasons the number of authors shown on this cover page is limited to a maximum of 10.

PHOTONIC TOPOLOGICAL EDGE STATES

A NANOSCALE INVESTIGATION

PHOTONIC TOPOLOGICAL EDGE STATES

A NANOSCALE INVESTIGATION

Dissertation

for the purpose of obtaining the degree of doctor
at Delft University of Technology,
by the authority of the Rector Magnificus, prof. dr. ir. T.H.J.J. van der Hagen,
chair of the Board of Doctorates,
to be defended publicly on monday 13 november 2023 at 17:30 o'clock

by

Sonakshi ARORA

Master of Science in Physics,
Freie Universität Berlin, Germany,
born in Kolkata, India.

This dissertation has been approved by the promotors

promotor: prof. dr. L. Kuipers
promotor: dr. A. Caviglia

Composition of the doctoral committee:

Rector Magnificus,	chairperson
Prof. dr. L. Kuipers,	Technische Universiteit Delft
Dr. A. Caviglia,	Technische Universiteit Delft

Independent members:

Prof. dr. N. Litchinitser	Duke University, Durham
Prof. dr. A. Szameit	University of Rostock, Germany
Dr. M. N. Ali	Technische Universiteit Delft
Dr. S. Conesa-Boj	Technische Universiteit Delft
Prof. dr. S. Gröblacher	Technische Universiteit Delft
Prof. dr. Y. M. Blanter	Technische Universiteit Delft (reserve member)

Keywords: topological photonics, optics, near-field microscopy, silicon-on-insulator

Printed by: Gildeprint, Enschede

Front & Back: *Whispers of the Whole* - Each cover represents experimentally measured Fourier transforms of a photonic crystal emulating valley-Hall effect, with the order indicated by flipbook images placed in the bottom right corner of the thesis pages.

Copyright © 2023 by S. Arora

Casimir PhD Series, Delft-Leiden 2023-33

ISBN 978-90-8593-580-3

An electronic version of this dissertation is available at
http://repository.tudelft.nl/.

To all those who think they aren't good enough.

Sonakshi Arora

Contents

Summary ix

Samenvatting xi

1 Introduction 1
- 1.1 Topology brought to light . . . 2
  - 1.1.1 Photonic crystals . . . 3
  - 1.1.2 Spin/Chirality/Helicity of light . . . 5
  - 1.1.3 Topological Photonic Crystals . . . 6
  - 1.1.4 Spin and Valley Degrees of Freedom . . . 7
- 1.2 Organization of the Thesis . . . 9

2 Engineering and measuring photonic topological insulators 11
- 2.1 A platform for topological photonic crystals . . . 12
- 2.2 Near-field measurements of topological photonic crystals . . . 13
  - 2.2.1 Separating polarisation components: E_x and E_y . . . 17
  - 2.2.2 Probe: fabrication, optimization, and characterization . . . 18
  - 2.2.3 Numerical simulations . . . 19

I Spin degree of freedom 21

3 Breakdown of spin-to-helicity locking at the nanoscale 23
- 3.1 Introduction . . . 24
- 3.2 Transforming near to far field . . . 27
- 3.3 Spatial distribution of spin density . . . 28
- 3.4 Momentum space analysis . . . 30
  - 3.4.1 Filtering out light cone . . . 30
  - 3.4.2 Building a Bloch mode . . . 31
- 3.5 Conclusions . . . 31

II Valley degree of freedom 33

4 Direct quantification of topological protection 35
- 4.1 Introduction . . . 36
- 4.2 Experimental observation of edge state . . . 36
- 4.3 Building the dispersion relation . . . 37
- 4.4 How robust is robust? . . . 38
- 4.5 Quantification of corner reflectivity and loss . . . 42
  - 4.5.1 Transfer matrix model . . . 42
  - 4.5.2 Effective corner reflectivity . . . 44
  - 4.5.3 Single corner reflectivity . . . 45

4.6 Influence of corners on backscattering . . . 47
4.7 Conclusions . . . 49
4.A Numerical calculation of edge state dispersion and eigenmodes . . . 50
4.B Dispersion relation of a W1 waveguide . . . 51

5 Interface dependence of topological edge state 53
5.1 Introduction . . . 54
5.2 glide shift on valley photonic crystal . . . 54
5.3 Robustness against valley-conserving defects . . . 56
5.4 Conclusions . . . 58
5.A Gradual transition of edge states from gapless to gapped . . . 59
5.A.1 Experiment . . . 59
5.A.2 Simulation . . . 59
5.B Proof of valley conservation at the L3 defect . . . 60

6 Multiple backscattering of photonic topological edge states 63
6.1 Introduction . . . 65
6.2 Experimental Results . . . 66
6.2.1 Mapping of the near-field edge state . . . 66
6.2.2 Visualizing real and reciprocal space of the edge state . . . 67
6.2.3 Introducing random intentional disorder . . . 69
6.3 Quantifying backscattering . . . 71
6.4 Group index contribution to backscattering . . . 74
6.A Engineered disorder fabrication . . . 76
6.B Electric field amplitude/intensity . . . 77
6.C Group velocity fits and center wavelengths . . . 77
6.C.1 Degeneracy point determination . . . 78
6.C.2 Subtleties in n_g determination . . . 79
6.C.3 Spatial map . . . 81
6.C.4 Calculated BMFP and mean group indices . . . 82

7 Conclusion 83

Bibliography 103

Curriculum Vitæ 105

List of Publications 107

Quotes Bibliography 109

Acknowledgements 111

SUMMARY

The aim of this thesis is to investigate the impact of symmetry on light and how it alters its characteristics. Our research centers around the examination of complex photonic crystals rooted in the concept of photonic topological insulators, which are analogs of topological insulators initially introduced in condensed matter physics. Unlike typical insulating materials, these possess a unique ability to conduct along their surface or edges. Leveraging this fundamental property, photonic topological insulators have gained attention for designing transport circuits resistant to back-reflection and scattering mechanisms.

To provide a foundation for understanding these concepts, Chapter 1 serves as an introduction. We introduce photonic crystals and the propagation of light as Bloch waves. Additionally, we delve into the vectorial nature of light. As photonic topological insulators, akin to two-dimensional graphene, exhibit diverse degrees of freedom, we explore the spin and valley degrees of freedom, which form the basis for categorizing the thesis into two sections. Before delving into experimental results, Chapter 2 elucidates the crucial concepts of fabrication and measurements for photonic topological insulators. We work with a silicon-on-insulator platform due to its high-refractive index dielectric, enabling the creation of high-quality, low-loss waveguides capable of confining light within the active silicon layer. Our near-field measurements are conducted in the telecom regime. We introduce Fourier transformation, filtering techniques for visualization, and polarization separation to equip readers with terminology essential for navigating subsequent chapters.

The heart of our research revolves around exploring topological phases resembling the Quantum Spin Hall effect (Part I) and the Quantum Valley Hall effect (Part II). These phases reveal critical attributes of photonic edge states, including spin-momentum locking, resilience to sharp corners, valley preservation in the presence of defects, and resistance to backscattering, even when subjected to engineered random disorder.

In Part I, we delve into photonic platforms emulating the quantum spin Hall effect, distinguished by a unique pseudospin. Each topological helical edge state is intrinsically linked to its designated pseudospin, which ideally facilitates coupling to quantum emitters with matching polarization states for on-chip quantum networks. Nevertheless, Chapter 3 uncovers a complexity within the subwavelength structure, as the highly structured field of the edge state results in a spatially varying optical spin density.

Part II explores non-trivial photonic systems possessing a valley degree of freedom, ensuring robust topology-protected transport of optical states in the presence of sharp corners, defects, and random disorder. Chapter 4 presents an experimental study quantifying the robustness of these topologically non-trivial eigenstates within a non-trivial topological waveguide. We observe significantly reduced backscattering along the interface in such crystals compared to conventional photonic crystal waveguides, especially in mirror-symmetric zig-zag interfaces. However, introducing a slight interface shift disrupts

valley-dependent transport, revealing the fragility of these topological photonic systems, as discussed in Chapter 5. Additionally, we explore the reduction in backscattering within topologically non-trivial photonic crystals, a crucial consideration in systems involving slowed-down light and heightened light-matter interaction. Chapter 6 presents a comprehensive analysis demonstrating that adding scatterers may have a more pronounced impact on topological modes than on trivial ones. Nevertheless, specific parameters show that non-trivial modes can still offer robustness, particularly in systems involving slow light. This research into photonic modes and their intriguing behaviors serves as the cornerstone of our thesis. The concluding chapter delves into the significance, implications, and broader contributions of these findings to the field.

SAMENVATTING

Het doel van deze scriptie is om te onderzoeken hoe symmetrie invloed heeft op licht en hoe het de kenmerken ervan verandert. Ons onderzoek draait om de studie van complexe fotonische kristallen die gebaseerd zijn op het concept van fotonische topologische isolatoren, analoge versies van topologische isolatoren die oorspronkelijk werden geïntroduceerd in de gecondenseerde materie fysica. In tegenstelling tot typische isolerende materialen, bezitten topologische isolatoren een unieke eigenschap om te geleiden langs hun oppervlak of randen. Door gebruik te maken van deze fundamentele eigenschap zijn fotonische topologische interessant voor het ontwerpen van transportcircuits die resistent zijn tegen terugreflectie en verstrooiingsmechanismen.

Om een basis te bieden voor het begrip van deze concepten, dient Hoofdstuk 1 als een introductie. We introduceren fotonische kristallen en de voortplanting van licht als Bloch-golven. Daarnaast duiken we in de vectoriële aard van licht. Omdat fotonische topologische isolatoren, vergelijkbaar met tweedimensionaal grafiet, diverse vrijheidsgraden vertonen, onderzoeken we de spin- en valleivrijheidsgraden, die de basis vormen voor de onderverdeling van de scriptie in twee secties. Voordat we dieper ingaan op experimentele resultaten, verduidelijkt Hoofdstuk 2 de cruciale concepten met betrekking tot de fabricage en metingen van fotonische topologische isolatoren. We werken met een silicium-op-isolator platform vanwege het dielectricum met een hoge brekingsindex, dat de creatie van hoogwaardige, laag-verlies golfgeleiders mogelijk maakt die licht kunnen beperken binnen de actieve siliciumlaag. Onze nabijveldmetingen worden uitgevoerd in het telecom frequentiegebied. We introduceren Fourier-transformatie, filtertechnieken voor visualisatie en polarisatiescheiding om lezers uit te rusten met de terminologie die essentieel is voor het begrijpen van de volgende hoofdstukken.

Het hart van ons onderzoek draait om het verkennen van topologische fasen die lijken op het Quantum Spin Hall-effect (Deel I) en het Quantum Valley Hall-effect (Deel II). Deze fasen onthullen cruciale kenmerken van fotonische 'edge states', zoals spin-momentum vergrendeling, weerstand tegen scherpe hoeken, behoud van valleien in aanwezigheid van defecten en weerstand bescherming tegen terugkaatsing, zelfs wanneer zelfs bij geëngineerde geconfronteerd met geëngineerde willekeurige wanorde.

In Deel I duiken we in fotonische platforms die het quantum Spin Hall-effect nabootsen, gekenmerkt door een unieke pseudospin. Elk topologisch helicaal 'edge state' is intrinsiek gekoppeld aan zijn aangewezen pseudospin, wat idealiter de koppeling met quantumemitters met overeenkomstige polarisatiestaten mogelijk maakt voor on-chip quantumnetwerken. Niettemin ontrafelt Hoofdstuk 3 een complexiteit binnen de subwavelength structuur, aangezien het sterk gestructureerde veld van de 'edge state' resulteert in een ruimtelijk variërende optische spinsdichtheid.

In Deel II verkennen we niet-triviale fotonische systemen met een 'edge state', die zorgen voor robuustheid bij topologie-beschermd transport van optische staten in aanwezigheid van scherpe hoeken, defecten en willekeurige wanorde. Hoofdstuk 4 presenteert

een experimentele studie waarin de robuustheid van deze topologisch niet-triviale eigentoestanden binnen een niet-triviale topologische golfgeleider wordt gekwantificeerd. We observeren aanzienlijk verminderde terugkaatsing langs de interface in dergelijke kristallen vergeleken met conventionele fotonische kristal golfgeleiders, vooral in spiegelsymmetrische zigzag-interfaces. Het introduceren van een lichte interfaceverschuiving verstoort echter het vallei-afhankelijke transport, wat de kwetsbaarheid van deze topologische fotonische systemen onthult, zoals besproken in Hoofdstuk 5. Daarnaast onderzoeken we de vermindering van terugkaatsing binnen topologisch niet-triviale fotonische kristallen, een cruciale overweging in systemen met vertraagd licht en verhoogde licht-materie interactie. Hoofdstuk 6 presenteert een uitgebreide analyse waaruit blijkt dat het toevoegen van verstrooiers mogelijk een meer uitgesproken impact heeft op topologische modi dan op triviale modi. Desondanks tonen specifieke parameters aan dat niet-triviale modi nog steeds robuustheid kunnen bieden, vooral in systemen met vertraagd licht. Dit onderzoek naar fotonische modi en hun intrigerende gedrag vormt de hoeksteen van onze scriptie. Het afsluitende hoofdstuk gaat in op de betekenis, implicaties en bredere bijdragen van deze bevindingen aan het vakgebied.

raakvlaktoestanden

1

INTRODUCTION

If I have seen further, it is by standing on the shoulders of giants.

[1]Sir Isaac Newton

1

Communication has played a central role in society since time immemorial enabling the exchange of emotions, ideas, and knowledge [1]. Throughout history, various methods have been employed for long-distance communication, such as the use of smoke and fire as means of signaling [2]. By burning specific materials distinct signals could be generated, creating smoke that could be observed at a distance. Similarly, mirrors were utilized as reflective surfaces to redirect sunlight and transmit messages. These methods involved the transfer of visual signals, i.e., they used light. Over the centuries, technological advancements have improved the efficiency and reach of communication systems, from the development of written languages to the invention of the telegraph, telephone, and the internet [3]. Light forms the backbone of modern telecommunication, from optical fibers to wireless communication systems [4–6]. Traditional systems heavily rely on the use of metallic conductors or dielectric waveguides to guide and manipulate light signals [7–9]. However, these conventional methods are not without limitations. Signal losses, electromagnetic interference, and the need for complex fabrication processes are just a few of the challenges faced by existing technologies [10].

In recent years, a groundbreaking field known as topological photonics has emerged, which holds the promise to revolutionize human communication once again [11–13]. Topological photonics incorporates unique properties of light in structured materials, offering solutions to the challenges faced by traditional communication systems [14–16]. The study of so-called topological photonic crystals allows us to explore the possibility of guiding light without any loss and ensuring the efficient and robust transmission of information. In addition to practical applications, the study of topological photonics stems from scientific curiosity. Understanding the fundamental concepts of light in these unconventional systems can provide insights into the workings of nature and can unveil previously unexplored phenomena [17, 18].

This thesis aims to explore how the symmetry imposed on light changes its behavior. We investigate non-trivial photonic crystals based on the photonic analog of topological insulators. In this introductory chapter, we begin our exploration with the concepts of topology adapted from condensed matter physics to photonic systems, in the realm of photonic crystals. We investigate one-dimensional (1D) photonic crystals and the Bloch wave nature of photons in periodic structures. Understanding the nature of Bloch waves is essential for comprehending the intricate behavior of light within photonic crystals. This work then gradually progresses to two-dimensional (2D) photonic crystals and through examination of their properties, discusses topological photonic insulators and their degrees of freedom. We focus on the topological phases emulating the Quantum Spin Hall effect (QSHE) and the Quantum Valley Hall effect (QVHE). We present an overview of the aspects of light-matter interactions related to spin, helicity, and chirality. Finally, we conclude with an outline of the thesis.

1.1. TOPOLOGY BROUGHT TO LIGHT

Science thrives on analogies. The discovery of a new class of materials known as topological insulators (TI) created major excitement in the scientific community [19–21]. In a TI, electron transport does not suffer back-reflections and is protected against scattering at bends and corners. These materials are insulating in bulk, but support conducting edge states at the interfaces of two materials as a result of certain physical properties that are

invariant under continuous deformations [11]. The concept is often understood at the expense of mathematicians by the example of the buns, bagels, and pretzels [22] *. In this thesis, we concentrate not on condensed matter physics but on its optical analogs. As a geometric concept, topology has progressed from a pure mathematical tool to being used in gauging the existence and robustness of scattering-free optical networks and understanding physical phenomena under smooth perturbations [23].

1.1.1. PHOTONIC CRYSTALS

To envision topologically protected transport in light at the nanoscale, we shift our observation scales from electronics to photonics. The field of photonics has seen tremendous growth in recent years since it offers the ability to manipulate light at the nanoscale using photonic crystals (PhCs). PhCs, also called semiconductors of light, possess a periodic modulation of the refractive index and exhibit frequency ranges where no modes inside the crystal can exist, so-called band gaps. By carefully engineering the band structure of these PhCs, we can control the propagation and localization of light, leading to a wide range of applications, such as filters, mirrors, and lasers [24, 25]. Key applications of PhCs lie in the field of optical waveguides and lattices [26–30]. Waveguides are structures that are modulated along a specific direction to confine and guide light along a specific path, with high efficiency and low loss [31–33]. These waveguides can be used in optical communications and sensing applications [34]. Analogous to electronic lattices [35] in solid-state physics, photonic lattices are structures that can be used to study the behavior of light in periodic systems, including phenomena such as Bloch oscillations [36–39] and Anderson localization [40–43].

PhCs can be fabricated along one, two, or three dimensions, depending on the dimensions along which the refractive index is modulated [44–49]. In this thesis, we investigate 2D photonic crystals, that possess index-guided modes in the plane of the crystal (x and y direction) that are confined in the out-of-plane z direction due to total internal reflection within a high refractive index material [24].

BLOCH NATURE

To comprehend the behavior of light in photonic crystals, we start with the simplest case of 1D photonic crystals. We apply principles of electrodynamics and symmetry [24] to understand the Bloch wave nature of photons in such a structure with a period a along the x direction. For a homogeneous medium, we assume the crystal has an imposed pseudo-periodicity since it possesses a constant dielectric permittivity $\epsilon = n^2$ and continuous translation symmetry. We mathematically express the propagation of light along $+x$ direction using Maxwell's equations, where the solution is a plane wave with the modes taking the form of [50]:

$$\mathbf{E}_k(x) = \mathbf{E}_0 e^{\mathrm{i}k_0 x - i\omega t}, \tag{1.1}$$

where $\mathbf{E}_0$ is an arbitrary constant vector. These plane waves manifest in the dispersion relation as $\omega = ck_0/n$ where ω is the optical frequency, k is the wavevector, n indicates the effective refractive index of the medium and c is the speed of light in vacuum. Therefore,

*A topologist is a mathematician who cannot tell the difference between a doughnut and a coffee cup - so goes the joke

for modes in a medium with pseudo-periodicity a, the dispersion relation is linear and is indicated in Fig. 1.1 with red dashed lines. The shaded blue region is a continuum of states that extends into the medium and for air where $n \approx 1$ is the light line denoted as the blue solid lines given by $\omega = \pm ck$.

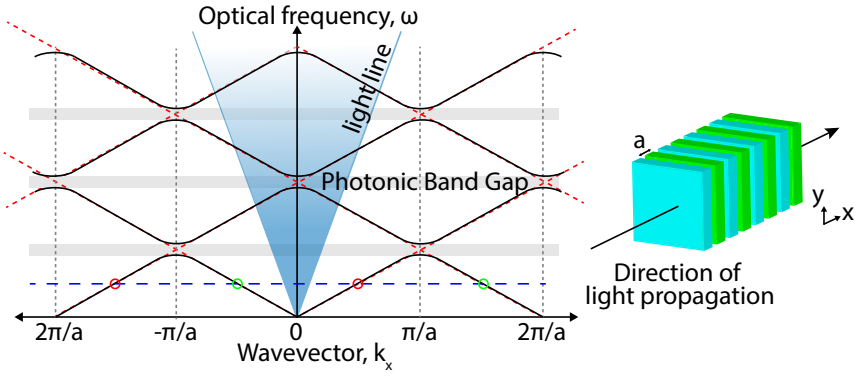


Figure 1.1: Schematic representation of a one-dimensional photonic crystal and its band structure with periodicity a. The direction of light propagation is in the $+x$ direction and is indicated by an arrow through the 1D photonic crystal. When a pseudo-periodicity a is imposed on the 1D crystal, the corresponding Bloch plane waves are denoted as dashed red lines indicating the fundamental and higher-order Bloch harmonics. With a dielectric periodicity a to the 1D crystal, the corresponding Bloch modes are shown as black curves with the grey region denoting a photonic band gap.

Now, we impose a periodic dielectric function $\epsilon(x) = \epsilon(x + ma)$, where m is an integer, to the medium along the $+x$ direction and homogeneous along the in-plane y, z directions. Bloch's theorem states that a wavefunction in a periodic medium can be written as a sum of plane waves, with an amplitude modulated by the periodicity of the underlying medium [35, 51]. Due to discrete translation symmetry along $+x$ direction with a lattice periodicity of a, we can rewrite the above expression as [52]

$$\mathbf{E}_k(x) = \mathbf{u}_k(x)e^{ikx}, \tag{1.2}$$

where $\mathbf{u}_k(x) = \mathbf{u}_k(x + \mathbf{R})$ denotes the discrete periodic envelope function and $\mathbf{R}$ is an integral multiple ($m \in Z$) of the lattice period. The resulting wave solutions E_k are known as Bloch states and are functions of space and time. As such, we can separate the time and spatial dependence by expanding the fields into a set of harmonic modes, and for simplicity, we ignore the time dependence of the plane wave. Therefore, Eq. 1.2 can be rewritten in the form of a Fourier series of plane waves as:

$$\mathbf{E}_k(x) = \sum_{m=-\infty}^{+\infty} A_m(k)\mathbf{E}_0 e^{i(k_x + m\frac{2\pi}{a})x}. \tag{1.3}$$

Here, $A_m(k)$ indicates the amplitude of Bloch harmonics. Eq. 1.3 indicates that all Bloch harmonics collectively make up one Bloch mode and are separated in wavenumber by $2\pi/a$. Computing the eigenvalues of this wave equation results in a band structure (Fig. 1.1). At an exemplary frequency indicated by a horizontal blue dashed line in Fig. 1.1, we

indicate Bloch harmonics with color-coded circles. For $m = 0$, the zero-order harmonic is referred to as the fundamental Bloch harmonic, and all the higher-order harmonics range from $-\infty$ to $+\infty$. In Fig. 1.1 all red-colored Bloch harmonics together form the Bloch mode propagating in the positive direction, while the green Bloch harmonics form the Bloch mode propagating in the negative direction. In the dispersion relation, the slope of the curve is defined as the group velocity $v_g = \frac{\partial \omega}{\partial k}$ and signifies the velocity with which the wave propagates in space. Therefore, each Bloch mode with positive group velocity is a forward propagating mode (red circles in Fig. 1.1), whereas a mode with a negative v_g is a backward propagating mode (green circles in Fig. 1.1). For a periodic modulation, the dispersion relation can, however, feature avoided crossings at either $k = 0$ or at the edges of the Brillouin zones. Around this gap, electromagnetic waves have no accessible modes and result in what is known as a stop-gap (grey shaded region in Fig. 1.1) [46]. It is important to note, that in the context of 1D photonic crystals, stop gaps can be considered band gaps because they represent ranges of frequencies that are prohibited or strongly suppressed in terms of light propagation through the crystal structure [24].

From a 1D photonic system, we move to a next higher-order photonic system, where the dielectric periodicity in the x and y directions ensures Bloch modes propagating in the plane of the crystal and is homogeneous along the third axis (z). Two-dimensional photonic crystals, also known as photonic crystal slabs, confine light in the direction perpendicular to the crystal plane by index guiding as a consequence of total internal reflection inside the high refractive index material [53, 54]. In free space ($n = 1$), we have wavevector $k^2 = k_x^2 + k_y^2 + k_z^2 = \omega^2/c^2$ [55]. However, in the case of a 2D system, the corresponding Brillouin zone is built using only in-plane wavevectors $k_\parallel = k_x, k_y$. Spatial confinement of guided modes in the slabs, therefore, results in $k_\parallel^2 > \omega^2/c^2$, and as a result, $k_x^2 + k_y^2 > \omega^2/c^2$ with k_z acquiring a purely imaginary value [55]. This results in index-guided modes being evanescent in z as they decay exponentially away from the 2D crystal plane. On the other hand, when $k_x^2 + k_y^2 < \omega^2/c^2$, the mode has a real k_z and can couple to far-field radiation. In such a case, the modes lie above the light line [56]. In this thesis, we consider air holes in a silicon-on-insulator platform which gives rise to transverse electric modes, where the magnetic field component H_z is normal to the plane and $\mathbf{E}$ is in the plane with $\mathbf{E}_z = 0$.

1.1.2. SPIN/CHIRALITY/HELICITY OF LIGHT

In the field of nano-optics and photonic crystals, spin, chirality, and helicity of light are distinct concepts that describe different aspects of light-matter interactions. It is important to understand these concepts relating to the rotational direction of light fields and topological photonics.

A beam of light carries both spin and orbital angular momenta in the direction of propagation [57]. The spin angular momentum of light (optical spin) is used to describe the polarization state of light. Light can be linearly polarized (where the electric field oscillates in a fixed direction), circularly polarized (where the electric field rotates in a circular motion), or a combination of the two, leading to elliptically polarized light. Circular polarization has two possible spin states: right-handed and left-handed, corresponding to clockwise and counterclockwise rotation of the electric field, respectively. The Jones matrix formalism is used to describe the polarization state of light as a 2×2 vector and

can be used to represent the transformation of the polarization state through an optical element such as a waveplate or a polarizer. It encodes the polarisation state using the complex amplitude and phase information for each polarisation component.

To facilitate experimental observations, another important formalism that describes the polarisation state of light is known as the Stokes parameters [58]. A set of four equations is derived from the electric field intensity and characterizes the degree of ellipticity and orientation of the polarization state. They are defined as:

$$\begin{aligned} S_0 &= E_x^2 + E_y^2 \\ S_1 &= E_x^2 - E_y^2 \\ S_2 &= 2E_xE_y\cos\Phi \\ S_3 &= 2E_xE_y\sin\Phi \end{aligned} \tag{1.4}$$

where E_x and E_y are the electric field amplitude of the x and y polarisation components, ϕ is the phase difference between the two components, S_0 quantifies the total intensity of polarized and unpolarized light, S_1 represents the degree of linear polarization (horizontal or vertical), S_2 quantifies the intensity of diagonal polarisation ($+45°$ or $-45°$), and S_3 evaluates the intensity of right or left circular polarisation.

The third Stokes parameter (S_3) is known as the helicity parameter and is defined in a two-dimensional system as $\sigma_z = \mathrm{Im}[\mathbf{E}\times\mathbf{E}]_z$. For perfectly left or right-handed circularly polarized light the helicity parameter takes a unit value $\sigma_z = \pm 1$ [59, 60]. Therefore, helicity is the component of spin angular momentum of circularly polarized light projected onto the propagation direction. Right-handed helicity corresponds to the spin angular momentum aligned with the direction of propagation, while left-handed helicity corresponds to the opposite direction as defined from the point of view of the source. In the context of photonic crystals, the helicity of light can be manipulated by the crystal structure, leading to various polarization-dependent optical effects.

An object that cannot be superimposed onto its mirror image is said to be chiral [61]. In the context of nano-optics and photonic crystals, chirality is often associated with the handedness of the structure. It can describe the arrangement of certain nanoscale structures, such as nanoparticles or helical nanostructures, that exhibit a specific handedness. Chirality plays a crucial role in the interaction of light with chiral materials and can result in interesting optical phenomena, such as circular dichroism and optical activity. In the context of topological photonics, the chirality of a photonic structure is often associated with the Berry curvature, which is a key quantity in the study of topological effects. For example, in the photonic quantum Hall effect systems, chirality can be used to control the sign of Berry curvature [62].

1.1.3. TOPOLOGICAL PHOTONIC CRYSTALS

Topological photonic crystals (TPCs) are a subset of photonic crystals that possess a nontrivial band structure [12, 63]. The topology of the bands is characterized by a quantity known as topological invariants. If a photonic band has an integer-valued topological invariant or Chern number, the system is said to be a Chern photonic insulator [19]. If the topological invariant takes up binary values, the topologically nontrivial systems are said to have $\mathbb{Z}_2$ topological invariants. These invariants are defined over the momentum space

as the integral of the Berry curvature within the first Brillouin zone [64]. Chern numbers can essentially be thought to be the same as the acquired Berry phase or geometric phase of a state that undergoes an adiabatic change in the momentum space of a 2D system when it returns to its initial position [65]. In conventional trivial bands, this geometric phase has a zero acquired phase, whereas in non-trivial bands the acquired non-zero phase is an integer multiple of 2π [66].

The physical significance of these topological invariants arises from their direct manifestation in the bulk-edge correspondence which dictates that the number of edge states depends on the difference of topological invariants [11, 67–70]. When two insulators with gapped band structures featuring distinct topological invariants are brought close together to form an interface, this must give rise to a gapless edge state and these invariants cannot change its value under continuous perturbations [71]. Topological invariants are a global property of the crystals' momentum space and ensure that the TPCs are robust against certain types of defects and disorders [72, 73], making them promising candidates for photonic applications where high tolerance to fabrication errors is required. The properties of TPCs can be engineered to suit specific applications to ensure unidirectional routing [56, 73] and have specific topological properties, such as the presence of topologically protected slow modes, which can be used in high-performance sensors [74, 75].

1.1.4. SPIN AND VALLEY DEGREES OF FREEDOM

Internal degrees of freedom (DoF) of light such as frequency, polarization, phase, spin, and orbital angular momentum can be independently manipulated to modulate the flow of light [76, 77]. Borrowing topological concepts from condensed matter physics to photonics allows us to control these DoF which results in unique properties of light propagation [78]. An essential condition for TPC is the requirement to break time-reversal symmetry. There are several ways to do so, for example, in gyromagnetic crystals using an external magnetic field [73, 79–82] where the wavefunction is characterized by a binary topological invariant ($\mathbb{Z}_2$). In the absence of a large magneto-optical response at optical frequencies, one can break pseudo-time-reversal symmetry and ensure robust edge state propagation and protection against specific types of disorders [83]. The two main DoFs that allow us to achieve a non-trivial topological invariant are discussed in this thesis - spin and valley - which can be used to categorize 2D nontrivial topological photonic systems that are time reversal symmetric but have broken spatial symmetries. These DoFs give rise to the photonic analog of QSHE and QVHE which are used to describe analogous phenomena related to the control of polarization states and the manipulation of light propagation in different momentum space regions.

We employ the electronic band structure of graphene [84] (schematically shown in Fig. 1.2(a)) to discuss the context of DoF in photonic systems. The band structure of graphene features a doubly degenerate Dirac cone where the conduction and valence band become degenerate at the corners of the first Brillouin zone (a set is labeled with K and K′ in Fig. 1.2)(b)) [84]. A planar surface of graphene has inversion and time reversal symmetry that protects the degeneracy of the Dirac points. For graphene, this degeneracy can be lifted by doping or strain which breaks inversion symmetry [85–87].

Analogous to the graphene lattice, we consider a photonic lattice with hexagonal

1

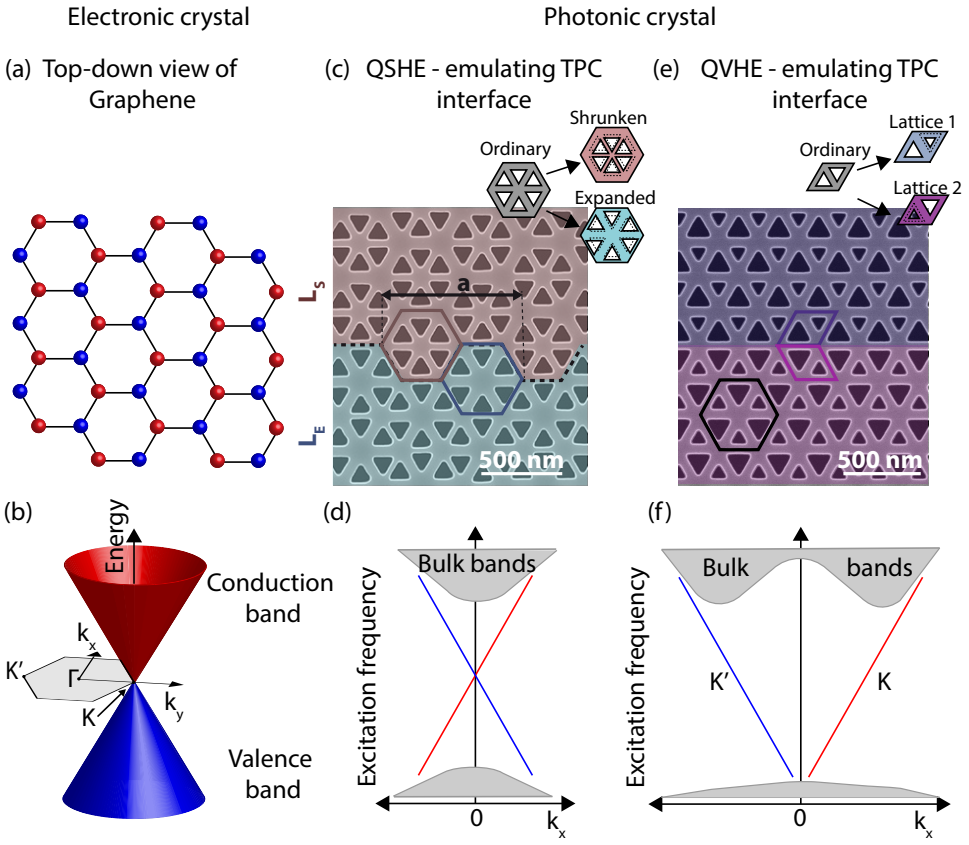


Figure 1.2: Schematic representation of an electronic and photonic lattice and their corresponding band structure. (a) Top-down view of graphene with two lattice sites forming a honeycomb structure. (b) The electronic band structure of graphene features a Dirac cone at the K and K′ valleys of the hexagonal Brillouin zone such that the conduction and valence band are degenerate at the Dirac point. Scanning electron micrograph of a topological photonic crystal interface emulating (c) quantum spin Hall effect and (e) quantum valley Hall effect. The schematic in (c) shows an ordinary unit cell with an arrangement of equilateral triangles in a hexagon. Continuous deformation of this arrangement results in the corresponding shrunken or expanded lattice. The schematic in (e) shows a rhombohedron ordinary unit cell that deforms to lattice 1 and lattice 2 possessing opposing valley Chern invariants. Dashed lines indicate the initial ordinary lattice arrangement. (d) The photonic diagram of the interface features two counter-propagating edge states at the Γ point for the QSHE emulating interface, with the red and blue lines indicating edge states with opposite group velocities. (f) Two degenerate edge states at the K and K′ (red and blue) with opposing group velocity traverse the bandgap of the QVHE-emulating interface.

symmetry and treat it as equivalent to a triangular lattice of hexagonal unit cells each containing six sites (see a schematic of an ordinary lattice in the inset of Fig. 1.2(c)). The resulting 2D lattice has a C_6 crystal symmetry with 60° rotational symmetry. Band folding results in a 4-fold degenerate Dirac cone at the center of the Brillouin zone at the Γ point [88, 89]. While maintaining the triangular lattice C_6 symmetry, we can deform the

hexagonal sites by concentrically moving them closer or apart. In the inset of Fig. 1.2(c), the ordinary lattice is deformed into the shrunken lattice (L_S; top) with the holes concentrically brought closer and the expanded lattice (L_E; bottom) as a result of triangular holes concentrically pulled apart. The different coupling strengths between neighboring sites in the two lattices impart a non-trivial nature to the expanded lattice with the band gap possessing an integer topological invariant $\mathbb{Z}_2 = \pm 1$ [90], whereas the shrunken lattice leads to a gapped but trivial topological invariant $\mathbb{Z}_2 = 0$. The interface of L_S and L_E supports two counter-propagating edge states that traverse the band gap around the Γ-point [88, 89]. A cross-band results in two counter-propagating edge states with opposing group velocities that indicate the presence of two pseudospin states (red and blue lines in Fig. 1.2(d)) within the bandgap [88]. These edge states exhibit spin-to-propagation direction locking and form the basis of quantum spin Hall effect emulating edge states which are further discussed in Ch. 3 [83, 91, 92]. In the analogy with graphene, this effect can be observed at the edges of graphene and is said to be topologically protected against non-magnetic defects as long as the disorder does not induce a spin flip [93].

In contrast to the spin DoF which supports edge states around the Γ point where $k = 0$, the valley DoF refers to the propagation of light at higher wavevectors, analogous to the K and K′ valleys in graphene [12, 82, 94–96]. We consider again the case of photonic graphene to have a hexagonal lattice with two sites forming a rhombohedron unit cell (see schematic of ordinary lattice in Fig. 1.2(e)). The crystal possesses C_3 group symmetry and results in the band structure featuring a doubly degenerate Dirac cone at the K and K' valleys in the irreducible Brillouin zone [95, 97, 98]. Breaking spatial inversion symmetry by adiabatically changing the side length of the sites lifts the degeneracy at the high symmetry points and opens a photonic bandgap. These high-symmetry points K and K′ acquire a valley Chern number $C_v = \pm 1/2$. Following the bulk-edge correspondence [67, 68, 99], an interface with two lattices (Lattice 1 and Lattice 2 in the schematic of Fig. 1.2(e) with distinct C_v results in one helical edge state crossing the bandgap region at each valley (red and blue linear dispersion shown in Fig. 1.2(f)). A simple case of such an interface is known as a zigzag interface, which has mirror symmetry and is further discussed in Ch. 4. Introducing a glide symmetry along the mirrored interface can give rise to a mode gap and can result in a breakdown of valley-dependent transport (see Ch. 5). Another type of glide symmetry includes transforming one of the sites into another which results in a bearded interface and gives rise to two distinct modes, trivial and non-trivial that are degenerate at the BZ edge due to glide symmetry. This type of interface is further discussed in Ch. 6 with respect to engineered random disorder and slow light behavior. We will further explore the nature of these degrees of freedom resulting from symmetry operations in detail and how their practical implementation contributes to the robustness of light propagation in the following chapters.

1.2. ORGANIZATION OF THE THESIS

A rigorous understanding of various aspects of these TPCs for describing novel physics is essential to build a complete picture of the value topological photonics holds in potential applications. The remainder of this first section is devoted to introducing the experimental tool that will allow one to fully understand the techniques that were employed in this research work. This thesis focuses on the design, fabrication, and characterization of

1

TPCs with nontrivial topological properties. We will also explore the effects of defects and disorder on the topological properties of TPCs. The thesis is organized in two sections: The first section is devoted to the Quantum Spin Hall effect emulating photonic crystals and the second half delves deep into nontrivial photonic crystals that emulate the Quantum Valley Hall effect.

- In **Chapter 2**, we outline the fabrication procedure to engineer photonic crystals on a silicon-on-insulator (SOI) platform. We also elucidate the experimental technique implemented to generate and detect topologically nontrivial fields at telecom wavelengths.
- In **Chapter 3**, we investigate the influence of the Bloch nature of QSHE emulating topological photonic crystals. We explore the spatial distribution of spin density in the near field and evaluate the measured and calculated global spin.
- In **Chapter 4**, we quantify the degree of topological robustness in QVHE emulating photonic crystals.
- In **Chapter 5**, we explore the interface-dependent behavior of the topological edge state in QVHE emulating TPCs. We assess the degree of robustness of these edge states in the presence of defects that preserve valley DoF.
- **Chapter 6**, we examine the extent of topological protection exhibited by QVHE emulating TPCs in the context of engineered disorder. This chapter focuses on assessing the impact of random disorder on the ability of the topological system to maintain its unique properties.
- In **Chapter 7**, we present the conclusions drawn from our research and provide an outlook for future studies aimed at unraveling the novel physics of topological photonic crystals. We delve into the potential impact of topological photonics in the telecom region and propose their adoption in the optical regime, specifically focusing on light-matter interactions with 2D semiconductors. This chapter serves to summarize the key findings of our work and highlight the exciting prospects for further exploration in this field.

2

ENGINEERING AND MEASURING PHOTONIC TOPOLOGICAL INSULATORS

The world is simple. It's miserable, solid all the way through. But if you can fool them, even if just for a second, then you can make them wonder, and you get to see something very special.

[2] Robert Angier

With near-field microscopy, we extract the complete vectorial and subwavelength information of topologically trivial and non-trivial photonic crystal edge states exploiting direct access to amplitude, phase, and polarisation resolution. We map the complex field profile and detailed structure of these edge states by coupling light into symmetry-protected two-dimensional photonic crystals. With an aperture-based probe, we raster scan in the vicinity of the sample surface. Using various data processing and visualization techniques, we extract a complete account of robustness, local helicity, and multiple scattering of edge states.

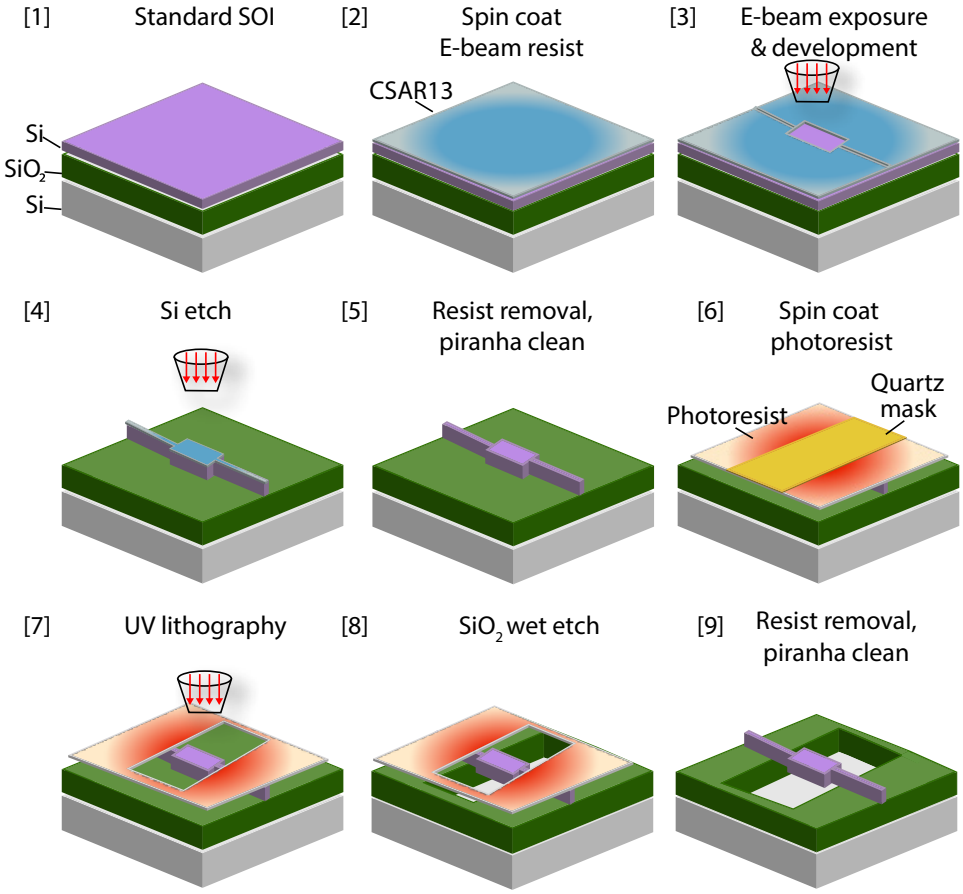


Figure 2.1: Fabrication process overview for a suspended photonic crystal.

In this thesis, we fabricate suspended photonic crystals (PhCs) and measure and evaluate their full complex mode behavior. We first introduce in detail the methods to fabricate these PhCs. Then we discuss the near-field scanning optical microscope investigations of the PhCs and elaborate on the techniques that equip us to understand the subsequent chapters. We also give an overview of the types of numerical simulations that were employed to support our experimental results.

2.1. A PLATFORM FOR TOPOLOGICAL PHOTONIC CRYSTALS

The technology of silicon-on-insulator (SOI) platforms has taken the world by storm over the last few decades. This platform combines the benefits of silicon-based electronics with the advantages of photonic devices, paving the way for high-performance optical communication and sensing networks. Integrating nanophotonic components onto SOI platforms has enabled high-speed optical communication and resulted in a drastic

improvement in the performance of on-chip photonic devices [100–103]. The work presented in this dissertation is based on the technologically mature silicon-on-insulator platform using a standard layer arrangement. The starting substrate of our PhCs is a 220 nm thick silicon layer supported by a 3 μm thick thermal oxide layer (SiO_2) and 700 μm thick Si substrate. The fabrication technique, independent of the precise lateral structure of the suspended PhCs, involves two lithography steps (see process flow in Fig. 2.1):

1. A positive electron-beam resist from the AR-P 6200 series is spin-coated between a monolayer of adhesion reagent HMDS and a conductive layer E-spacer 300Z (Fig. 2.1(2)). Please note that the adhesion and conductive layers are not used for samples investigated in Ch. 6 and Ch. 5. The thickness of the electron-beam resist is 240 nm. The desired PhC design is patterned using e-beam lithography on a Raith Voyager with 50 kV beam exposure (Ch. 4 and Ch. 3), and a Raith EBPG5200 with 100 kV beam exposure (Ch. 6 and Ch. 5). The resist is developed in pentylac- etate/O-Xylene/MIBK:IPA(9:1). The intermediate device is schematically shown in Fig. 2.1(3). The chip is then exposed to a reactive-ion etching plasma of HBr:O_2, to transfer the patterned design on the device layer (see Fig. 2.1(4)). The resist is removed in a hot DMF solution at 80°C for 10 minutes and the device is carefully cleaned in a hot acid piranha solution for 8 minutes and subsequently super critically dried.

2. Photolithography resist AZ1518 (Ch. 4 and Ch. 3) and S1813 (Ch. 6 and Ch. 5) of thickness 1.3 μm is patterned with a pre-designed quartz rectangular mask to define a selective wet-etch window to expose only the PhC region 2.1(6-7). After development in AZ400K:H_2O and MF321:H_2O (Fig. 2.1(7)), the thermal oxide layer is locally removed in a buffered solution 5:1 and 7:1 of hydrofluoric acid, respectively (Fig. 2.1(8)). The PhC is then subjected to careful cleaning in hot acid piranha solution and super-critically dried (shown in Fig. 2.1(9) [97].

Thus, a free-standing membrane with a photonic crystal, comprising air holes is obtained.

2.2. NEAR-FIELD MEASUREMENTS OF TOPOLOGICAL PHOTONIC CRYSTALS

We employ near-field microscopy, a powerful tool to map the evanescently decaying complex electromagnetic field confined to the Si-slab. This technique has been extensively discussed in literature [104–106]. In this chapter, we discuss the techniques specifically modified to measure and investigate non-trivial topological fields in two-dimensional photonic crystals. In the subsequent chapters of this thesis, schematic diagrams of the experimental technique are included, highlighting the aspects employed to obtain the specific chapter-related experimental results. In general, we employ a heterodyne detection scheme to obtain amplitude and phase information [107]. The method is based on a Mach-Zehnder interferometer, in which the excitation laser beam is divided into two paths: a reference and a signal path. The former is shifted in frequency by 40 kHz using a pair of acousto-optic modulators. In the latter, the free-space light is coupled into the photonic structure under investigation using a high numerical aperture (NA = 0.8)

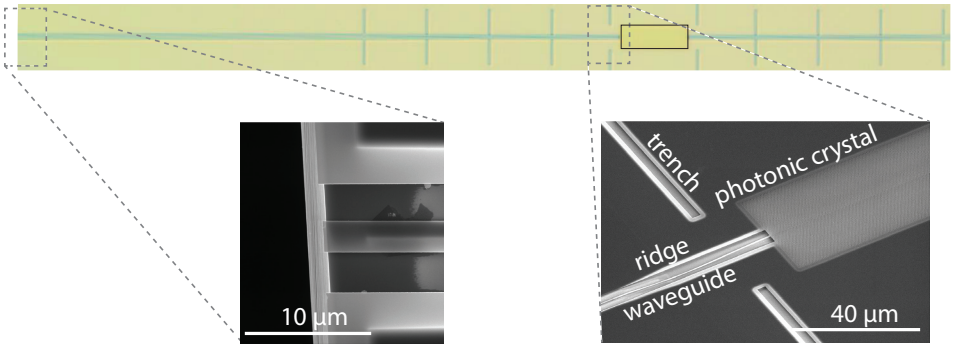


Figure 2.2: An overview optical image of an exemplary topologically non-trivial photonic crystal interface. Left inset: A zoom-in SEM view of the free-space incoupling waveguide with the arrow indicating the direction of light. To ensure optimum coupling efficiency, it is essential to obtain a clean cleave along the Si crystal axis. Right inset: A zoom-in view of the termination of the photonic crystal. Side trenches are introduced to scatter potential, excited slab modes in the Si membrane outside of the ridge waveguide.

microscope objective and is subsequently picked up by a near-field probe. Combining the light from both paths leads to a beating signal at the above-mentioned frequency shift. This allows us to extract the amplitude and phase of the signal via a lock-in amplifier (here a pair of Stanford Research Systems SR830 were used).

In collection mode [108, 109], a near-field probe with an optical aperture with a subwavelength diameter is scanned above the sample surface, at a constant height of ca. 20 nm. The typical aperture diameter used in this thesis is 150 nm. Constant height is maintained with a shear-force feedback mechanism [110]. Maintaining a constant height is crucial to keep the amplitude constant, but also to prevent image distortions owing to the three-dimensional structure of the evanescent field of the eigenstates of photonic crystal waveguides [111, 112]. A larger separation between the probe and sample surface would also lead to a reduction of k-space information since higher spatial frequencies decay faster away from the surface, eventually smearing out the electric field profile. The evanescent decaying field in the z-direction couples to the aperture using frustrated total internal reflection [113]. A fraction of the evanescent wave is then converted into a propagating wave guided through the optical fiber. The detected signal is divided into the signal received by the two detectors L_1 and L_2 using standard polarization optics which includes a polarizing beam splitter, thereby providing polarisation resolution to the measured in-plane E field [104] (see also 2.2.1 for more on the characterization of the polarisation components).

COUPLING LIGHT INTO THE CRYSTAL

We couple monochromatic light at telecom wavelengths using a tunable continuous wave laser (Santec TSL-710) into a carefully cleaved SOI substrate through a ridge waveguide (left inset in Fig. 2.2) that supports multiple transverse electromagnetic (TE) modes. Multi-mode light travels for a distance of 2 mm along the $+x$-direction until the waveguide

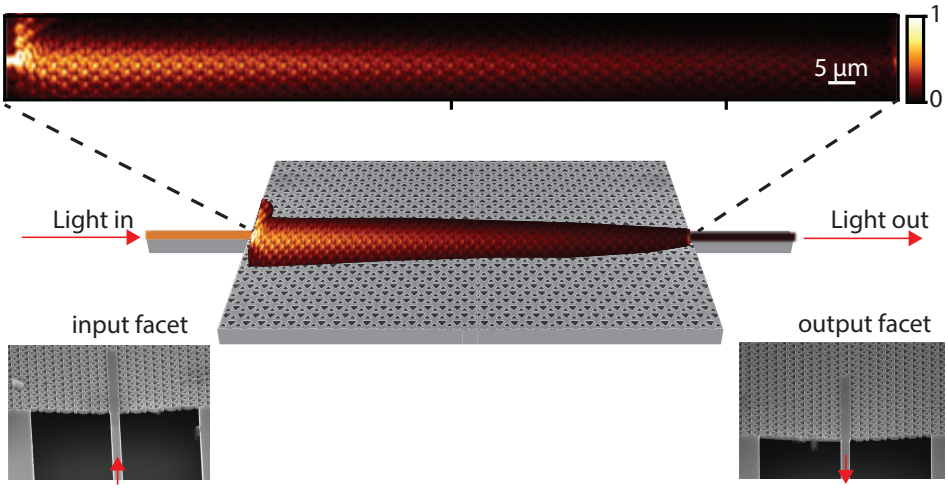


Figure 2.3: Example of a near-field map of light in a topological photonic crystal. The color map represents the normalized electric field amplitude of light in the photonic crystal after it has entered through the left (depicted by the red arrow labeled Light In) through the feed waveguide, propagating through the entire length of the crystal until it leaves from the output facet (depicted by the red arrow labeled Light Out). Inset: A zoom-in SEM image of suspended input and output facets and the corresponding feed waveguides.

eventually tapers a width of 400 nm supporting a single fundamental TE mode (right inset in Fig. 2.2). Trenches along the ridge waveguide are designed as out-couplers for scattering light coupled into the slab modes of the surrounding silicon at the entrance facet and bouncing around all different boundaries in this 2D waveguide. An incoupling PhC feed waveguide is designed inside the PhC to ensure better index-matching of the modes from the single TE-like mode in the suspended ridge waveguide into the PhC edge mode (see Fig. 2.3) [97]. With a thickness of 220 nm and refractive index $n_{Si} = 3.48$, at a wavelength $\lambda = 1550$ nm, the suspended ridge waveguide supports a fundamental transverse electric $TE_{0,0}$ mode with an effective refractive index $n_{\text{eff}} = 1.84$. The electric field of the TE mode lies completely in-plane (x, y), with the oscillating electric field E perpendicular to the propagation direction, and the wave vector given by k_x. The in-plane E is separated into two Cartesian components E_x and E_y, and the field has an out-of-plane magnetic field component H_z. Since the out-of-plane wavevector k_z is purely imaginary, the resulting evanescent field decays exponentially away from the surface.

VISUALIZING ELECTRIC FIELDS

In this thesis, we typically map the PhC interface in the excitation wavelength range $\lambda = [1480\,\text{nm} - 1640\,\text{nm}]$. An example in Fig. 2.4(a)-(c) shows the experimentally measured near-field amplitude of a topological photonic crystal emulating spin hall effect (discussed in detail in Ch. 3) at an excitation wavelength $\lambda = 1540$ nm. The near-field maps depict the real space electric field amplitude $|E|(x, y)$ in Fig. 2.4(a) and its Cartesian components $E_x(x, y)$ and $E_y(x, y)$ in Fig. 2.4(b) and (c), respectively. We observe a subwavelength modulation of the field profile of the edge state which follows the periodicity of the

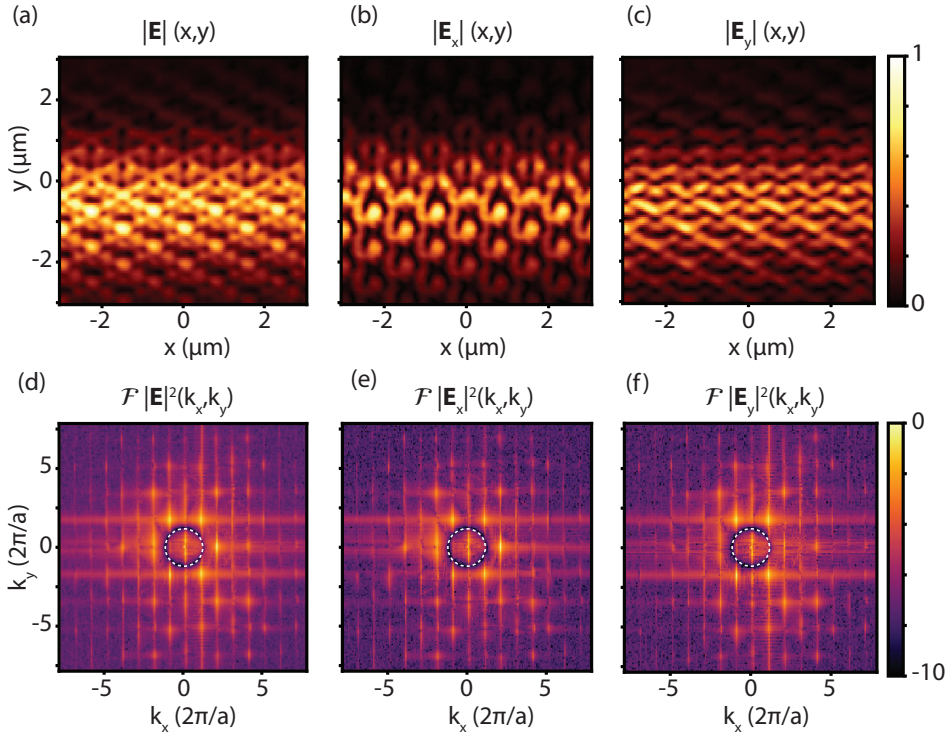


Figure 2.4: Experimentally measured real and reciprocal space of a topological edge state at an exemplary wavelength $\lambda = 1540\,\text{nm}$. The first row (a) - (c) presents the normalized electric field amplitude $E_{\parallel}$ and the corresponding in-plane x and y field components. The second row shows the amplitude of the corresponding spatial frequencies obtained through a Fourier transformation of the real space maps. The white dashed circle depicts the light cone in the air.

underlying lattice.

The phase resolution of the experimental setup gives access to the full complex in-plane field amplitude to extract the real and imaginary components of the field. We subsequently apply a two-dimensional Fourier transform to the real-space field maps to obtain the reciprocal wavevectors shown in Fig. 2.4(d)- (f). In the reciprocal space, we observe a hexagonal pattern of high-intensity regions. This pattern is a direct consequence of the PhC lattice symmetry. An exemplary reciprocal space map is shown in logarithmic scale to highlight the high signal-to-noise ratio (SNR) and dynamic range achievable via the described near-field microscope.

TREATMENT OF RECIPROCAL SPACE DATA

- Filtering out the light cone - A common feature in all Fourier images at a chosen excitation frequency (ω) in Fig. 2.4(d)-(f) is the circular ring with a radius of $\sqrt{k_x^2 + k_y^2} = \omega/c$ indicated by the white dashed line. This ring in two-dimensional space, with amplitude in all directions, corresponds to a horizontal cut through the

light cone in the three-dimensional plane. Its presence indicates light grazing the surface of the PhC and picked up by the probe. Hereafter, we filter this ring pattern to ensure that we obtain only the light in the photonic eigenstates of the structure under investigation. Furthermore, this filtering technique allows us to separate the spatial frequencies of the eigenstate that couple to the far field (everything inside the light cone ring) and the near-field of the underlying mode. In addition to filtering out the far-field, we slightly modify this filtering technique to separate the fundamental and the higher-order Bloch harmonics (BH). The fundamental BH corresponds to the part of the edge state lying in the first Brillouin zone and includes all information in the transverse direction k_y. On the other hand, higher Bloch harmonics are separated in incremental units of $2\pi/a$ along the x-axis, where a is the lattice constant of the periodic photonic crystal along the x-direction. These techniques will be discussed in detail in Ch. 3.

- Zero-padding - To ensure that the measured dispersion images do not exhibit a Fourier artifact in the form of a breathing pattern due to abrupt ends of the measurement data, we add zeros to increase the number of points for the decomposition. It is essential to note, that zero-padding is only added for visual purposes. An alternative way to present dispersion curves without altering any of the measured data is by using a window function such as a Hanning window [114]. This involves reducing the amplitude at the boundaries of a finite data set to prevent sharp features in the Fourier-transformed image.

- Separating forward and backward propagating modes - Propagating modes in a finite length PhC can suffer reflections at a defect or the end-facet (right inset of Fig. 2.3). To decouple a forward propagating mode from a backward propagating one, we isolate the modes as determined by their group velocity. With a mode propagating along the x-direction, modes with a positive slope are indicative of forward propagation, whereas the modes with a negative slope are the reflected backward propagating ones. This will be further discussed in Ch. 4 in Fig. 4.2.

2.2.1. SEPARATING POLARISATION COMPONENTS: E_x AND E_y

A rigorous calibration of the polarization resolution of the near-field detection system is essential to unambiguously discuss the near-field helicity of the topological fields in Ch. 3. While a cylindrical symmetric aperture, in principle, allows for a separate pickup of E_x and E_y [104], birefringence effects due to the bending of optical fibers in the collection path can result in a (slight) modification of the polarization of the collected light in the detection fiber. This can lead to cross-talk of the field components extracted via the near-field probe and transmitted to our detection optics. To account for this mixing, we use a quarter and half waveplate before far-field detection to separate two polarisation components in the same Cartesian reference frame as at the near-field probe position. To ensure proper calibration, we use the field symmetry of a known fundamental TE_{00} mode in the photonic ridge waveguide (see right inset of Fig. 2.2) to infer any additional rotation angle needed for the waveplates, following le Feber et al., 2014 [115]. This procedure allows us to compensate for the unwanted cross-talk. We, subsequently, use symmetry considerations to calculate the extent of polarisation mixing in the probe which typically

results in <1% mixing of the signals in the two detectors. The process is repeated for the entire excitation wavelength range to account for the frequency dependence of our optical measurements. The obtained additional rotation compensation is multiplied via a rotation matrix onto the experimentally obtained E field map for each excitation wavelength.

We acknowledge that our near-field microscope does not only detect purely electric fields but also the magnetic component of the electromagnetic field [106, 115–118]. Taking into account a cylindrical aperture probe and propagating mode behavior, we always assume that the detectors detect a combination of electric and magnetic fields which are related to each other by a proportionality constant. Therefore, throughout the thesis, we denote the measured maps of optical electric fields only.

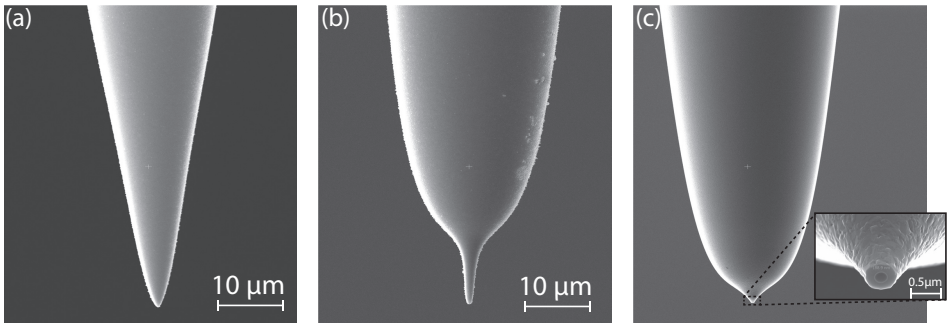


Figure 2.5: SEM images showing the optimization of the metal-coated aperture probes. (a) The probe with unoptimized parameters that provide a straight pencil-like shape to the apex. (b) The optimized probe with a dumbbell shape, with a long taper. (c) After buffered HF dipping to ensure isotropic etching to remove the long taper, and obtain a large pick-up angle. Right inset: An example of an optimized probe with an aperture diameter of 150 nm and pick-up angle of 42°.

2.2.2. PROBE: FABRICATION, OPTIMIZATION, AND CHARACTERIZATION

The single-mode optical fiber used as the basis for our near-field probes is Corning SMF-28 and is designed for wavelength $\lambda = 1550$ nm with a core diameter 8.2 μm. The fiber is pulled with a laser-based micro-pipette puller system P-2000. The pulling parameters were chosen to guarantee a dumbbell shape (see Fig. 2.5(b) and (c)) and not a straight shape (see Fig. 2.5(a)) to ensure a higher throughput [119]. To create a high pick-up angle (see right inset of Fig. 2.5(c)), we immerse the probes in buffered oxide etch (BOE) comprising a volume ratio 7:1 of ammonium fluoride, hydrofluoric acid, and water for 20 mins to ensure an isotropically etch of the glass fiber core [120]. The diameter of the probe's apex is critically determined by a combination of pulling and BOE etch time. A uniform coating of a metal, in our case, aluminum of thickness 100 nm – 200 nm is evaporated onto the fiber dielectric surface, to prevent the fields from leaking to the far field through the walls of the probe. An aperture is created at the apex using focused ion-beam milling [121]. The probe diameter of $\lambda/7$ at the apex determines two quantities: the sub-wavelength resolution and the measured SNR.

Each probe is characterized to ensure a high transmission and polarisation resolution

before introducing them in the near-field setup. We use a far-field characterization technique to examine the quality of the prepared probes. We image the focal and back-focal plane of the probe with a laser wavelength $\lambda = 1550\,\text{nm}$ on an Infrared CCD camera. An ideal probe's transmission focal image is a concentric spot indicating a perfect Airy pattern and a perfectly circular back-focal image without any defects or spots. This indicates that no additional pinholes are present in the probe. A three-paddle polarisation controller in combination with a linear analyzer is introduced to characterize the polarisation sensitivity of the probe. The paddle controller uses stress-induced birefringence that alters the polarization of the transmitted light in the fiber and allows us to map the polarization over the full Poincaré sphere.

2.2.3. NUMERICAL SIMULATIONS

We use both COMSOL [122] and MPB [123] software packages to simulate the electromagnetic fields of a periodic photonic structure and determine the eigenfrequencies of its modes. They use different numerical methods and algorithms for solving the underlying equations.

In Ch. 3 and Ch. 5 we use COMSOL which uses a finite element method to solve the electromagnetic wave equation. This involves dividing the simulation domain into small sub-regions and approximating the solution to the partial differential wave equations of each sub-region using a polynomial expansion. This approach can be accurate for complex geometries and materials with arbitrary refractive indices.

For Ch. 4 and Ch. 6 we use MPB which uses a plane wave expansion method. This method involves expanding the electromagnetic fields in terms of plane waves and solving for the eigenfrequencies using a matrix eigenvalue equation. This approach is efficient for periodic structures with a high degree of symmetry, such as photonic crystals, and assumes materials without losses.

I

SPIN DEGREE OF FREEDOM

3

BREAKDOWN OF SPIN-TO-HELICITY LOCKING AT THE NANOSCALE

Things we lose have a way of coming back to us in the end.
If not always in the way we expect.

[3]Luna Lovegood

In this chapter, we investigate the local near-field optical spin in topological edge state waveguides that emulate the quantum spin Hall effect. We reveal a highly structured spin density distribution that is not linked to a unique pseudospin value from experimental near-field real-space maps and numerical calculations. We confirm that this local structure is essential in understanding the properties of optical edge states and light-matter interactions. The measured global spin in the far field is reduced in the near field and, for certain frequencies, flipped compared to the pseudospin measured in the far field. We experimentally reveal the influence of higher-order Bloch harmonics in spin inhomogeneity, leading to a breakdown in the coupling between local helicity and global spin.

Parts of this chapter have been published in Physical Review Letters **128**, 290303 (2021) [124]

3.1. INTRODUCTION

Unidirectional photon emission is achieved, by strong coupling of a quantum emitter supporting a circularly polarized dipole moment to photonic states with a corresponding local polarisation orientation (helicity) [59, 125–127]. The resulting chiral quantum optical interface is a consequence of spin-momentum locking [128] and serves as a luring proposition for large-scale on-chip quantum networks [129, 130]. However, a finite spin-to-direction coupling and susceptibility to disorders and defects [131] invokes the demand for an explicit account of the local structure of the edge state's optical spin density profile to achieve high directional coupling [127, 132–141].

In this chapter, we employ the photonic crystal-based analog of topological insulators which emulate the quantum spin Hall effect (QSHE) [19]. Experimental as well as numerical realizations have shown that the two edge states at the interface between a topologically trivial and non-trivial lattice [88, 89] each exhibit a unique pseudospin due to the different topological invariants of the supporting bulk bands. Such an interface offers robust photonic transport against defects and sharp corners [133, 142, 143]. This transport relies on pseudospin coupling to the far-field (FF) helicity to ensure and maximize photon unidirectionality [144]. Leveraging the helicity supported by these systems has enriched applications for quantum entanglement [135] and quantum spin circuits [91, 145–148]. However, it is essential to determine the exact relation between field helicity and edge state pseudospin.

With that intent, we examine the near field of edge states in topological photonic crystals (TPCs) to comprehensively study the (local) chiral information. With aperture-based phase- and polarisation-resolved near-field optical microscopy [106], we collect the orthogonal in-plane polarisation components of the electric field using a heterodyne detection scheme and determine the underlying spatially varying spin density. We experimentally verify that the inhomogeneity in optical spin density follows the Bloch periodicity of the lattice. By experimentally accessing the different Bloch harmonics (BHs) that together form the symmetry-protected edge state, we show that accounting for the individual contribution of each higher-order BH breaks the coupling between pseudospin and helicity of the edge state.

Following the shrink-and-grow design [88, 89, 149], we realize a TPC interface on a silicon-on-insulator platform by deforming a graphene-like hexagonal lattice with six equilateral triangular holes. While the unperturbed lattice features a doubly degenerate Dirac cone at the Γ-point in the dispersion diagram, this degeneracy is lifted in two ways (see Fig. 3.1(a)): on one side of the interface, the holes are concentrically shifted inwards, called the shrunken lattice (L_S), while on the other side, the holes are shifted concentrically outwards, labeled as expanded lattice (L_E). The geometrical transformations emulate a synthetic gauge field and keep the global C_6 symmetry of each lattice unaltered. The band structure of L_S and L_E both reveal a direct bandgap at the Γ-point. For L_S, the shape of the electric field in the lower band resembles 'p'-like orbitals and the upper band resembles 'd'-like orbitals, whereas for L_E, the mode symmetries of the upper and lower band are inverted [88]. The different intra- and inter-cell coupling strengths between neighboring sites in the two lattices impart a non-trivial nature to the expanded lattice with the band gap possessing integer spin-Chern numbers ($C = \pm 1$) [90], whereas the shrunken lattice leads to a gapped but trivial band ($C = \pm 0$). The interface of L_S and L_E supports two

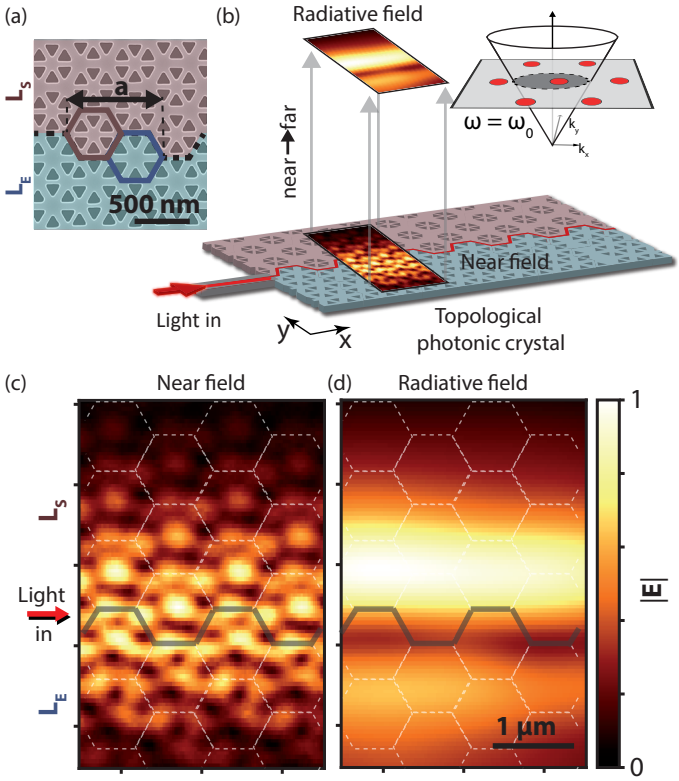


Figure 3.1: (a) Scanning electron micrograph (SEM) of the topological interface in the fabricated sample with the color-coded regions depicting the shrunken L_S (red) and expanded L_E (blue) lattices. The lattice periodicity is a=880 nm. (b) Schematic representation of the TPC lattice with overlaid near- and far-field amplitudes of the electromagnetic field. Inset: Schematic representation of the reciprocal space of an edge state (frequency $\omega = \omega_0$) with its typical hexagonal pattern of intensity peaks together with the 3D light cone of air (ω = c k). The dashed circle at the intersection of the light cone and the reciprocal space of the edge states represent the largest spatial frequencies of the edge state that can couple to the far field. Close-up of the normalized in-plane electric (c) near-field and (d) radiative field amplitude in the TPC featuring an armchair interface at λ = 1520 nm with the light launched into the structure from the left (indicated by the red arrow). The dashed hexagonal pattern outlines the underlying crystal lattice.

counter-propagating edge states that traverse the band gap around the Γ-point [88, 89]. These edge states are robust against back-scattering and offer unidirectional transport, provided no scattering between pseudospins occurs. The TPC reported in this chapter is different from a photonic crystal emulating the quantum valley Hall effect [95, 97, 150–152], as the latter supports edge states that lie around the high-symmetry points K and K' of the Brillouin zone. Since the QSHE TPC edge states traverse the Γ-point, the counter-propagating modes lie above the light cone and therefore couple to FF radiation. This makes them accessible to far-field spectroscopic investigations [142, 149, 153]. Here, the polarization of the light scattered to the FF shows a near-unity optical spin and can be directly linked to the state's pseudospin [79, 149, 154]. However, the radiative FF does

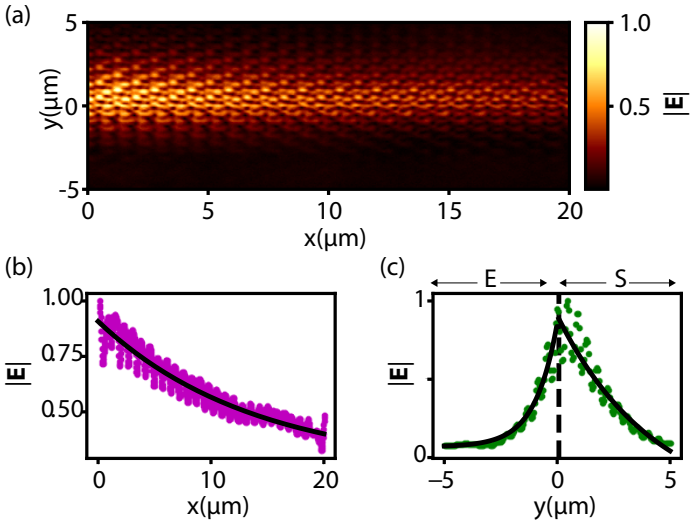


Figure 3.2: Near-field map of a photonic crystal with an armchair edge: (a) Experimentally measured electric field amplitude ca. 20 nm above the surface of the photonic crystal at an excitation wavelength $\lambda = 1560$ nm. (b) Normalized integrated amplitude over the longitudinal extent of the edge state in the direction of propagation along the interface. The solid line corresponds to an exponential decay fit to the data. (c) Normalized integrated amplitude from the transverse area. The two solid black lines indicate the exponential decay fit away from the interface into the bulk of the lattices (expanded on the left and shrunken on the right)

.

not contain the full complex information of the evanescent electromagnetic field since it only takes into account the plane waves within the light cone [155, 156] and a detailed account of the full local field is imperative for ensuring chiral light-matter interactions on the nanoscale.

To experimentally investigate the spin character of the TPC interface rigorously, we fabricate a lattice featuring an armchair (AC) interface. Fig. 3.1(a) shows the unit cell structure on both sides of the interface. We measure the complex in-plane electric field distribution E using a phase- and polarization-resolving near-field scanning optical microscope. Fig. 3.2a shows the real space scan of the full electric field distribution at an exemplary wavelength of $\lambda = 1560$ nm. The mode is confined to the armchair interface and decays exponentially along the propagation direction (see Fig. 3.2b). The mode amplitude diminishing while propagating from left to right is associated with radiative coupling to the FF [79, 149, 154]. We fit an exponential function to extract a decay length of $L = 13.73\,\mu$m. Fig. 3.2c shows the transverse extent of the edge state away from the armchair interface into the expanded and shrunken lattices. The extracted penetration length in the expanded lattice is $D_E = 0.98\,\mu$m whereas the extracted penetration length in the shrunken lattice is higher with $D_S = 4.31\,\mu$m, which is consistent with the relative width of the photonic bandgap. As a result, the field extends further into the L_S bulk than in L_E. This asymmetry in evanescent tails is consistent with the relative width of the photonic bandgap of the lattices, which is larger for L_E.

3.2. TRANSFORMING NEAR TO FAR FIELD

Light propagation along the interface is schematically visualized in Fig. 3.1(b). Here, we distinguish the two typical evaluation regimes of the electromagnetic (EM) field: near (NF) and radiative far (FF). The former defines the EM field directly above the crystal surface, constituting both the decaying evanescent field and the radiative field ($\mathbf{E_{rad}}(x, y)$) of the propagating edge state. It is important to note, that $\mathbf{E_{rad}}(x, y)$ is the spatial distribution of the Bloch modes mapped at the near field of the interface, however, only contains spatial frequencies that radiate to the far field (where $k_\parallel = k_x^2 + k_y^2 < \frac{\omega^2}{c^2}$). In Fig. 3.1(c), we depict the measured electric field amplitude over 2 unit cells at an excitation wavelength of $\lambda = 1520\,\text{nm}$. A highly structured field is visible. A zoom-in of the full near- and radiative field is shown in Fig. 3.1(c) and (d). The field profile around the AC interface (indicated by the solid gray line in Fig. 3.1c) resembles a Bloch wave [157] with pockets of high and low field amplitude forming a hexagonal pattern that repeats with lattice periodicity a along the propagation direction $+x$. The dominant part of the field is confined to the interface. The structured NF information is transformed to the radiative FF of the edge state by limiting the collected wavevector range to lie within the light cone using Fourier filtering. This is depicted in the inset of Fig. 3.1(b) which shows a schematic of the reciprocal space of the edge state with intensity peaks in a hexagonal pattern for an exemplary excitation frequency ω_0. The single peak inside the dashed circle on the $2D$ projection of the light cone for ω_0 constitutes the radiative FF. In contrast to Fig. 3.1(c), where the amplitude antinodes follow the underlying crystal structure, the FF amplitude is homogeneous along the TPC interface (see Fig. 3.1(d)). For a Bloch mode propagating in the x-direction, an infinite set of BHs in reciprocal space (with spatial frequencies separated by multiples of $2\pi/a$, where $a/\sqrt{3} = 800\,\text{nm}$ is the lattice periodicity) together form the detailed near-field structure of an edge state in real space. Each BH contributes to the mode amplitude with a certain weight that leads to the field variations in each unit cell. In the y-direction, the periodicity of the lattice causes peaks in reciprocal space with the same spacing, corresponding to the lateral mode profile of the edge state [158]. Only spatial frequencies within the so-called light cone (dashed circle in inset Fig. 3.1(b)) can couple to the FF. Here, this fundamental BH radiates to the FF as it couples with the continuum of free-space air modes. We obtain it by filtering to the single in-plane k-vector inside the light cone. A Fourier transform of these spatial frequencies yields the radiative field (Fig. 3.1d). Predictably, the dominant field energy in the FF lies more on the shrunken side of the interface, consistent with NF observations and the corresponding size of the bulk band gaps. An evanescent field strongly confined to the interface, propagating in the $+x$ direction and decaying in y-direction, implies the existence of transverse spin [60, 159–161] with positive and negative helicity mirrored at the interface. For our C_6 symmetric lattice, this results in the dominance of one designated helicity that is locked to the direction of mode propagation. The calculated transverse optical spin of the evanescent field is therefore a non-zero value. However, the spin distribution of the mode in the NF and FF differs greatly, well beyond a simple smoothening of the near-field pattern.

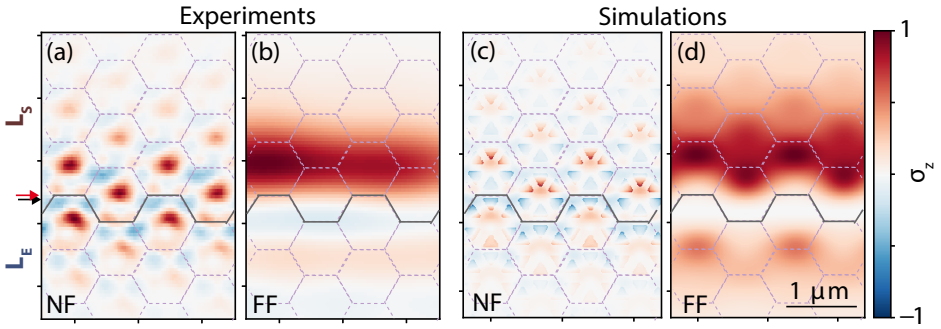


Figure 3.3: (a) Experimentally measured NF spin density σ_z of the AC-edge mode over two unit cells for an excitation wavelength of $\lambda = 1520\,\text{nm}$. (b) Experimentally measured FF spin density over the same extent as in (a), realized by filtering out the non-radiative wavevectors of the field shown in (a). (c) Numerically calculated spin density for $k_x = 0.08\,(\pi/a)$ with (d) displaying the spin density for numerical simulations in the FF. The solid gray line indicates the armchair interface while the dashed hexagonal pattern outlines the underlying crystal lattice.

3.3. SPATIAL DISTRIBUTION OF SPIN DENSITY

From the experimentally measured in-plane complex electric field, we reconstruct the spin density distribution $\sigma_z(x,y) = \text{Im}\,[\mathbf{E}^*(x,y) \times \mathbf{E}(x,y)]_z$ [159], where $\mathbf{E}^*(x,y)$ is the complex conjugate of the electric NF and Im indicates that only the imaginary part of the resultant complex vector field is extracted. The derived quantity is visualized in Fig. 3.3 which depicts the experimentally measured ((a),(b)) and numerically calculated ((c),(d)) $\sigma_z(x,y)$. For the evanescent field, σ_z is the expectation value of the helicity of light and it directly translates to the *local* field polarization state of the photonic TE-like mode as a result of spin-orbit interactions. The NF σ_z depicted in Fig. 3.3(a) reveals a highly structured σ_z distribution. A periodic pattern of $+\sigma_z$ and $-\sigma_z$ is observed, that repeats with a periodicity of a in the propagation direction and $a/\sqrt{3}$ in the transverse direction. Close to the center of any given unit cell indicated by dashed lines in Fig. 3.3(a), antinodes of $+\sigma_z$ are prominent, whereas around the outlines of the unit cell, the sign of σ_z flips. This spin flip within a unit cell confirms that the local handedness of a topological edge mode's polarization state is non-uniform. The local inhomogeneity of the spin density $\sigma_z(x,y)$ in the NF

$$\mathbf{E}_{\mathbf{NF}}(x,y) = \iint_{-\infty}^{\infty} \widetilde{\mathbf{E}}(k_x,k_y)\, e^{i[k_x x + k_y y]}\, dk_x\, dk_y,$$

which takes into account all spatial frequencies, completely vanishes in the FF

$$\mathbf{E}_{\mathbf{rad}}(x,y) = \iint_{k_x^2+k_y^2<k_0^2} \widetilde{\mathbf{E}}(k_x,k_y)\, e^{i[k_x x + k_y y]}\, dk_x\, dk_y$$

(shown in Fig. 3.3(b)), where $k_0 = \omega/c$. For an excitation wavelength of $\lambda = 1520\,\text{nm}$, only $+\sigma_z$ is visible close to the interface. This is in perfect agreement with reports of near-unity spin density in FF measurements [149]. Comparing both regimes to numerical

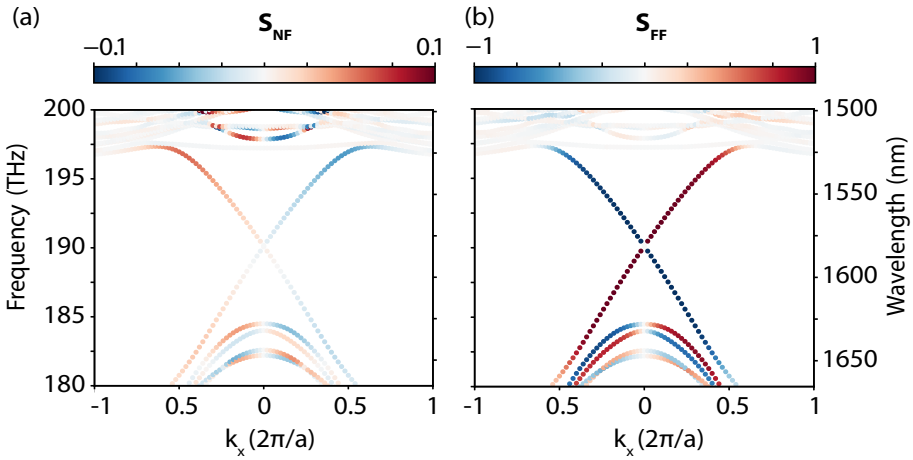


Figure 3.4: Numerically simulated dispersion relation where the edge state eigenfrequencies are color-coded with the estimated (a) near-field and (b) far-field optical spin S.

simulations in Fig. 3.3(c) and (d) reveals an excellent agreement of the σ_z distribution for the NF as well as the FF case, respectively. To understand the origin of the observed spatial variations and differences in NF and FF, we undertake a detailed analysis of the edge states in momentum space.

We investigate the dissimilarity in the NF and FF optical spin density distribution by analyzing the *global* optical spin $S = \iint \sigma_z(x,y)\,dx\,dy$ of the edge state for its full band dispersion, representing the integrated helicity of the interface mode. The global spin is calculated for a simulation region of $15\,\mu\text{m} \times 13\,\mu\text{m}$. Fig. 3.4 shows the calculated eigenmodes of the AC interface for both regimes. Figures 3.4(a) and (b) both show a linear dispersion for the edge states that lie within the band gap and cross at the $\Gamma-$point. The edge states are disconnected from the top and bottom bulk bands and recombine at the Brillouin zone edge. We notice an anti-crossing of 0.1 THz, predicted by the extended tight-binding model [162] and observed in experiments [149]. This is a result of spin-spin scattering due to the coupling of the counter-propagating edge states governed by the local C_6 symmetry breaking at the interface of the TPC. For Fig. 3.4(a) and (b) the color scale represents the sign of the optical spin S. The minimum and maximum extent of the scale for the two subplots are distinctly different. Fig. 3.4(a) shows the dispersion obtained by calculating S from the in-plane field distributions and is referred to as the NF optical spin (S_{NF}). As expected, the degenerate counter-propagating edge states exhibit opposing helicity. However, we observe that this helicity is flipped in Fig. 3.4(b), where we plot the FF spin (S_{FF}) of the edge states. The linear state with negative S_{NF} possesses positive S_{FF} and vice versa. Moreover, the S_{FF} exhibits a near-unity value, more than an order of magnitude larger than the maximum $S_{\text{NF}} = \pm 0.056$. The tight-binding approach predicts that the pseudospin for each edge state is uniquely linked to its FF helicity. On the other hand, the much lower S_{NF} and the spin-flip suggest that the pseudospin of the full electromagnetic mode of the edge state is not uniquely linked to a designated S_{NF}. The principal difference between NF and FF observations stems from the fact that the

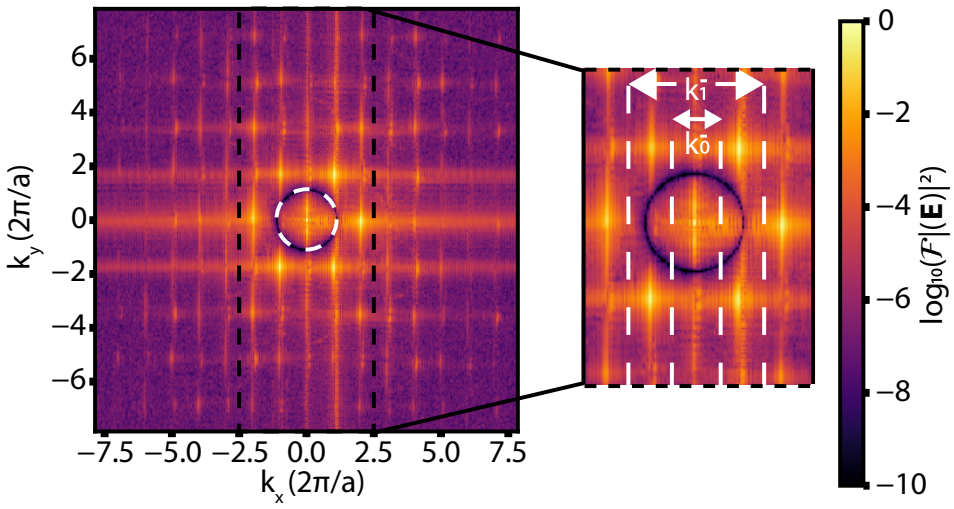


Figure 3.5: Two-dimensional Fourier representation of the experimentally measured electric field amplitude of the TPC edge mode at a wavelength of $\lambda = 1560\,\text{nm}$, with the amplitude shown in logarithmic scale. The reciprocal lattice vectors are periodically separated in the propagation direction (k_x) in units of $2\pi/a$, where a is the lattice constant of the armchair edge. The white dashed circle represents the light cone in the air. Inset: Zoom-in of momentum space restricted to show the fundamental ($k_{\bar{0}}$) and first higher-order BH ($k_{\bar{1}}$).

evanescent NF contains information from all higher-order BHs, which are unaccounted for in the FF. To better understand this intriguing spin-flip transition, we investigate the spin of the individual BHs.

3.4. MOMENTUM SPACE ANALYSIS

3.4.1. FILTERING OUT LIGHT CONE

The origin of the spatially varying spin distribution of the Bloch periodic structure is confirmed by performing a two-dimensional Fourier transform $\mathscr{F}(k_x, k_y)$ (shown in Fig. 3.5) of the measured complex field amplitude as visualized in Fig. 3.2, for an excitation wavelength $\lambda = 1560\,\text{nm}$. The high-intensity peaks arranged in a hexagonal pattern in reciprocal space are the result of the underlying C_6 symmetry. A small amount of air-guided, unwanted stray light that is not part of the edge state mode, skims along the surface of the photonic crystal. Because it propagates parallel to the surface, its spatial frequency lies exactly on the circular ring originating from the light cone (indicated as the white dashed circle in Fig. 3.5) and can therefore easily be removed by Fourier filtering. For the chosen wavelength, within this light cone lies a central peak at $k_y = 0$ that corresponds to the part of the Bloch mode radiating to the FF. Along k_x at multiples of $2\pi/a$, clusters of peaks are seen that correspond to the different BHs building up the intricate NF subwavelength structure of the edge state. An excellent signal-to-background ratio (S/B) of 40 dB is obtained in our experiment which allows us to resolve seven different BHs. These BHs, each contributing with different weights, together form the edge state mode which obeys Bloch's theorem [158]. Individual contributions of individual BH to S

hold the utmost significance in understanding the inhomogeneity in the underlying spin structure.

3.4.2. BUILDING A BLOCH MODE

We restrict our analysis to building up BH contributions by increasing the Fourier filter width in momentum space along k_x. In Figures 3.6(a) and (b), the first column represents the S originating from the fundamental BH ($k_{\bar{0}}$) which extends from $k_x = [-0.5, 0.5]$, while the consecutive columns represent S corresponding to all higher-order BHs up and including the BH indicated in the horizontal axis label, i.e. the wavevector range $k_{\bar{n}} \widehat{=} [-1, 1] * (n+0.5)$ (see right inset of Fig. 3.5). The frequency of the Γ-point crossing (denoted by dashed gray line) differs in Fig. 3.6(a) and (b) due to slight variations in the geometric parameters of the fabricated photonic crystal device. The quantitative analysis of the BH contribution to the optical spin is performed by first isolating BHs of certain width along k_x, applying an inverse Fourier transform to obtain the real-space field amplitude, and subsequently calculating S. For $k_{\bar{0}}$, S reflects the near-unity value that has previously been reported in FF measurements [149]. Taking an exemplary frequency of 188.92 THz in simulations, the radiative FF helicity $S_{k_{\bar{0}}} = 0.53$. As the filter width in k_x increases along the x-axis in Fig. 3.6, the optical spin S of the edge state reduces drastically (at an exemplary frequency the integrated NF spin $S_{k_{\bar{5}}} = -3.931 \times 10^{-4}$). We acknowledge that the distinct difference between exact values of S for experiment and numerical calculation arises partly from the polarization sensitivity of the NF probe [163]. Nevertheless, $S_{k_{\bar{x}}}$ undergoes a clear reduction from the fundamental BH column represented as $k_{\bar{0}}$ to the first higher-order BH represented as $k_{\bar{1}}$, as shown in Fig. 3.6. For simulations, the calculated average reduction factor of S in the near-field is 30. This means that S cannot be a deterministic helicity parameter of the edge interface when including more than the fundamental BH since a one-on-one relation between local spin and helicity is no longer valid. For every additional higher BH contribution starting at $k_{\bar{1}}$ and above along the x-direction, the spin-momentum coupling breaks down to such an extent that it results in a sign flip as is evident from the sign switch (positive to negative value) with increasing frequency in the right inset of Fig. 3.6(b). It is important to note that the color bar for the inset was saturated to ±0.1 to make the sign flip for $k_{\bar{1}}$ and above visible. The extrema of the numerically simulated S is ±0.57. Therefore, we observe that already adding the first higher-order BH contribution to that of the fundamental BH completely breaks down pseudospin-momentum coupling.

3.5. CONCLUSIONS

In summary, we experimentally visualize the intricate spin density distribution of symmetry-protected edge states in topologically non-trivial photonic crystals that lie above the light line, using a NF microscope. We demonstrate that spin in such photonic systems no longer retains its unique handedness in comparison to electronic systems, where **s** must always be a good quantum number. We report that even the contribution of the first-order BH unambiguously flips the sign for certain excitation frequencies. Consequently, a *priori* knowledge of detailed high spin density locations obtained from NF information will improve the chances of precise positioning of quantum emitters

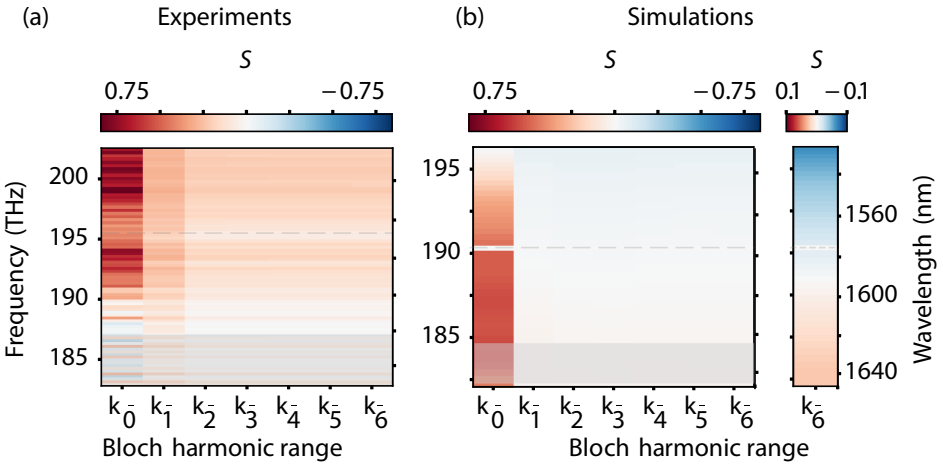


Figure 3.6: Build-up of spin-dependent contributions of the BHs from (a) experiment and (b) numerical simulations, evaluated over several higher-order BH ranges. Right inset: Spin-dependent contribution for the largest evaluated BH range which extends from $k_x = [-6.5, 6.5]$ with a saturated color scale. The gray dashed line indicates the frequency of the Γ-point crossing. The grayed-out region extending below 184.4 THz depicts the lower band edge.

along chiral interfaces. Without this knowledge, spin-polarised emission will result in the mixing of pseudospin edge states, and therefore reduce the desired network efficiency. Thus, this finding needs to be accounted for in the architectures of future topological photonic quantum networks and it provides a pathway towards engineering truly robust topologically protected chiral interfaces.

II

VALLEY DEGREE OF FREEDOM

4

DIRECT QUANTIFICATION OF TOPOLOGICAL PROTECTION

I was wise enough never to grow up while fooling people into believing I had.

[4]Margaret Mead

In this chapter, we divert our attention to tailored photonic crystals (PhCs) that emulate quantum valley-Hall effects. We present a direct quantitative evaluation of topological photonic edge eigenstates and their transport properties in the telecom wavelength range using phase-resolved near-field optical microscopy. Experimentally visualizing the detailed sub-wavelength structure of these modes propagating along the interface between two topologically non-trivial mirror-symmetric lattices allows us to map their dispersion relation and differentiate between the contributions of several higher-order Bloch harmonics. Selective probing of forward- and backward-propagating modes as defined by their group velocities enables direct quantification of topological robustness. Studying near-field propagation in controlled defects allows us to extract the upper limits of topological protection in on-chip photonic systems in comparison with conventional PhC waveguides. We find that protected edge states are two orders of magnitude more robust than modes of conventional PhC waveguides. This direct experimental quantification of topological robustness comprises a crucial step toward the application of topologically protected guiding in integrated photonics, allowing for unprecedented error-free photonic quantum networks.

Parts of this chapter have been published in npj, Light: Science & Applications **10**, 9 (2021) [150]

4.1. INTRODUCTION

The promise of photonic topological insulators (PTIs) [79, 164–167], supporting unhindered transport around defects and sharp corners as large as 120° bends without optimization is interesting for protected light-matter interactions [168] and integration of robust quantum devices [169]. In the linear [83, 88, 142, 149] and nonlinear regimes [170], topological robustness against backscattering at corners has been inferred by high transmission [97, 151]. This is in sharp contrast to conventional nanophotonic systems with low backscattering at sharp bends. Additionally, these conventional systems pose a great design challenge owing to the need to balance high bandwidth, low reflectance, and modest footprint. A ubiquitous quantification of robustness as the defining quality of scattering-free propagation has remained elusive. Potential interference effects and out-of-plane scattering losses at local disorder render this quantification challenging.

In this chapter, we report a rigorous robustness evaluation of valley photonic edge eigenstates at telecom wavelengths. Local investigation of the states' transport properties via phase-resolving near-field microscopy provides direct insight into topological protection, through the distinction between forward and backward modes. We find that protected edge states are two orders of magnitude more robust to backscattering at corners as compared to conventional waveguides.

We realize valley-Hall PhCs (VPCs), which rely on the valley degree of freedom linked to the breaking of a specific lattice symmetry [12, 97, 171–173]. Similar to the valley-selective polarization caused by spin-orbit coupling in transition metal dichalcogenides [174], these PhC lattices exhibit a non-vanishing Berry curvature at the K and K' points of the Brillouin zone [95]. In contrast to the quantum spin-Hall effect emulating PhCs that support edge states at the Γ-point, the edge states in the following VPCs occur below the light line and thus feature negligible radiative losses. Since each valley is associated with an intrinsic magnetic moment, the valley-Chern invariant $C_{K,K'} = \pm 1/2$ signifies a *pseudo-spin* [175], rendering the bulk band structure topologically non-trivial. An interface formed by two parity-inverted copies of the PhC lattice results in two degenerate and robust edge-state eigenmodes confined to the interface that linearly traverse the photonic band gap (PBG), each with a unique *pseudo-spin* [176]. As long as the lattice symmetry is preserved and no inter-valley scattering occurs to flip the *pseudo-spin*, these edge states are predicted to be immune to reflection from local disorder along the interface [82, 95].

4.2. EXPERIMENTAL OBSERVATION OF EDGE STATE

To determine the experimentally achievable robustness against back-scattering, we fabricate a VPC working at telecom wavelengths on a silicon-on-insulator (SOI) platform following the design of [97] (see Fig. 4.1a). Light is coupled into the PhC structure in the $+x$ direction from an access waveguide. This system supports edge modes of opposite group velocity $\pm v_g$ (see Sec. 4.A, Fig. 4.10) propagating along the interface between two parity-transformed lattices (VPC_1 and VPC_2). We visualize the spatial wavefunction of the mode with a phase-sensitive near-field scanning optical microscope [106, 158]. Fig. 4.1b shows the measured two-dimensional in-plane field amplitude map at a wavelength of $\lambda = 1600\,\text{nm}$. The detected transverse-electric (TE)-like field pattern confined to the interface of VPC_1 and VPC_2 extends laterally over roughly five unit cells, revealing an

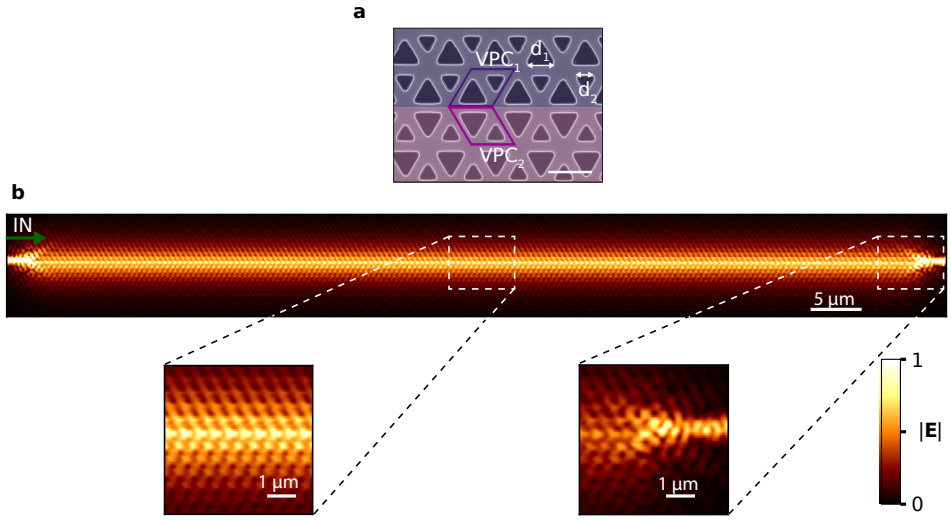


Figure 4.1: Experimental visualization of a topological edge state in a valley photonic crystal. (a) SEM of the fabricated structure with two pseudo-colored regions depicting the two lattices VPC_1 and VPC_2, with opposite valley-Chern invariants. The unit cell with lattice constant $a = 503\,\text{nm}$ consists of equilateral triangular holes of side lengths $d_1 = 0.7a$ and $d_2 = 0.45a$. Scale bar: 500 nm. (b) Measured normalized amplitude of the in-plane field components at a laser excitation wavelength of $\lambda = 1600\,\text{nm}$ over the extent of 165 unit cells, with the scale bar corresponding to $5\,\mu\text{m}$. Light is launched from a feed waveguide at the left side of the crystal, with the direction indicated by the green arrow. Left inset: zoom-in of the detected field amplitude pattern along the interface. Right inset: Zoom in on the out-coupling flank of the access waveguide.

intricate sub-wavelength mode structure (left inset of Fig. 4.1b). The measured fields show close correspondence to the numerical calculations (see Sec. 4.A, Fig. 4.10). At the locations of the access and exit waveguides, the influence of broken lattice symmetry and the adjacent feed waveguide becomes evident in the distorted field pattern (right inset of Fig. 4.1b).

4.3. BUILDING THE DISPERSION RELATION

The heterodyne detection configuration of the employed near-field microscope gives access to the complex in-plane optical fields of the edge mode [107]. As a direct consequence of Bloch's theorem, the two-dimensional spatial Fourier transformation $\mathcal{F}(k_x, k_y)$ of the measured field amplitude allows the individual analysis of Fourier components with positive and negative group velocities. An illustrative Fourier map at $\lambda = 1600\,\text{nm}$ is displayed in Fig. 4.2a. By repeating the near-field scans and corresponding Fourier analysis for $\lambda = [1480\,\text{nm} - 1640\,\text{nm}]$ and integrating $\mathcal{F}(k_x, k_y)$ over k_y, we extract the mode dispersion shown in Fig. 4.2b. The numerically simulated edge- and bulk-bands show excellent overlap with the experimentally measured dispersion, as can be seen in the overlaid enlarged view presented in Fig. 4.2c. We achieve an excellent signal-to-background (S/B) ratio $\approx 56\,\text{dB}$. The achieved spatial resolution, combined with the high S/B, enables

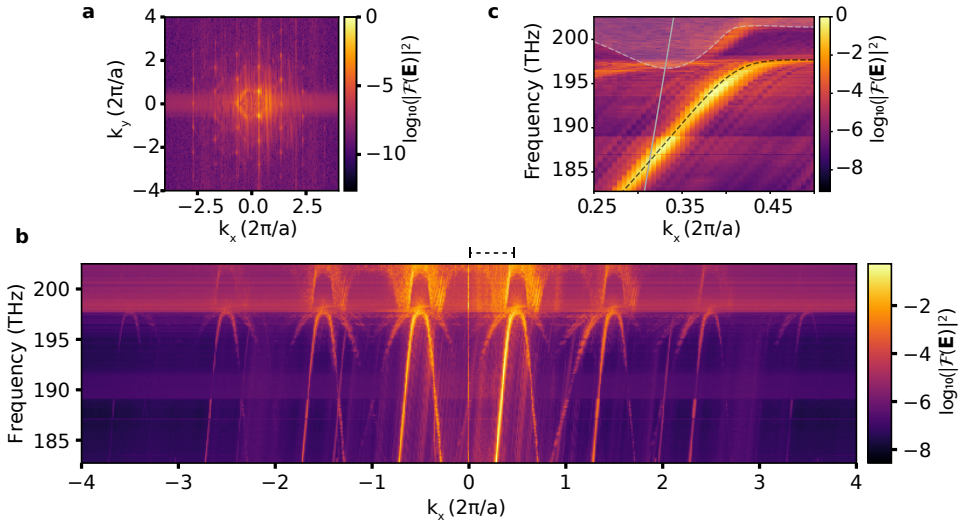


Figure 4.2: Momentum space of the VPC edge state. (a) Two-dimensional Fourier transform of the real space amplitude distribution of the PhC mode. High-intensity points are periodically separated by the reciprocal lattice vector $2\pi/a$ in the direction of propagation k_x along the edge and by $4\pi/\sqrt{3}a$ in the transverse direction k_y, representing the bulk reciprocal symmetry. (b) Experimentally retrieved dispersion diagram. Bright lines of positive slope indicate a positive group velocity (forward propagating modes), while lines with negative slope indicate a negative group velocity (backward propagating modes). Consecutive Bloch harmonics are separated by the size of a single Brillouin zone ($2\pi/a$). Frequencies above 197.5 THz correspond to bulk bands. The Fourier intensity for each excitation frequency is normalized to the overall maximum value. In addition to the dominant modes in the forward and backward directions, lines with half and a third of the dispersion slope appear. These are attributed to a nonlinear interaction with the scanning near-field probe (see Sec. 4.B) (c) A close-up of the experimentally retrieved dispersion diagram limited to the first Brillouin zone edge, denoted by black dashed brackets. The black dashed lines indicate the numerically simulated values for the edge state (See Ch. 2.2.3 for details). The solid gray line denotes the light line and the gray dashed lines with grayed-out regions indicate the onset of the bulk bands.

us to resolve at least six higher-order Bloch harmonics over multiple Brillouin zones. The lines with a positive slope correspond to a single forward-propagating mode with group velocity $v_g = c/6$. Closer inspection reveals negatively-sloped lines corresponding to a single backward propagating mode with $-v_g$ [104, 177]. This separation of forward- and backward-propagating Bloch modes allows the local monitoring of back-scattering along the interface.

4.4. HOW ROBUST IS ROBUST?

Using this local phase and amplitude information, we probe a straight edge interface, as shown in Fig. 4.1b. We obtain the quantities W_F and W_B representing the forward and backward energy, by integrating over the full Fourier intensity of the forward and backward modes, respectively. The ratio $\eta_e = W_B/W_F \approx 0.03$ unambiguously yields the conversion from forward to backward propagation, a result of scattering events occurring at and beyond the VPC end facet. Thus, η_e includes coupling of the forward-to-backward

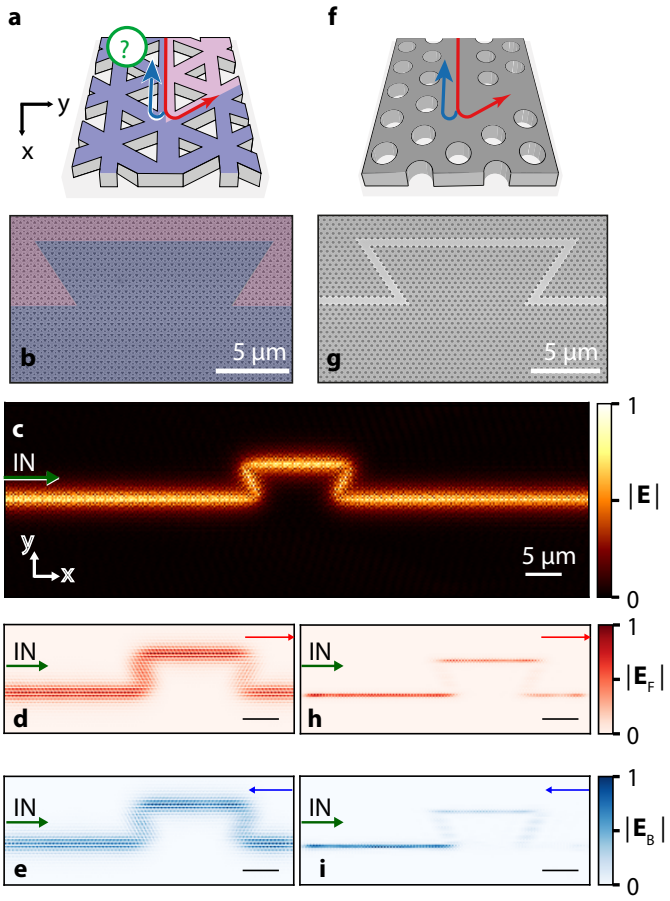


Figure 4.3: Directional transport along defects. For the topologically non-trivial VPC waveguide, (a) shows the schematic of the probed 120° corner. (b) Top-view SEM image of the fabricated Ω-shaped defect. Two-dimensional real-space amplitude maps showing the (c) full mode amplitude distribution, (d) forward propagating mode amplitude only, and (e) backward propagating mode amplitude only. The amplitude maps are normalized independently to their maximum value. For a topologically trivial W1 waveguide, (f) schematically shows the mode propagation around a 120° corner, and (g) shows a top-view SEM image of the device. The two-dimensional amplitude maps of the filtered forward and backward propagating modes are shown in (h) and (i) respectively. The direction of in-coupling is indicated by the green arrows. All scale bars correspond to 5 μm.

mode energy away from the topologically protected regime. This initial examination of the straight edge with the observed back-propagation energy dominated by contributions of the end facet, calls for a more intricate analysis of topological protection.

To quantify protection without the aforementioned contributions, we introduce a trapezoidal (Ω-shaped) structure along the interface comprising four sharp corners (Fig. 4.3). This structure is expected to be topologically protected since $n \times 120°$ bends respect the underlying C_3 lattice symmetry. Reflections characterized by energy coupled between the degenerate forward (F) and backward (B) propagating modes are indicated by red and

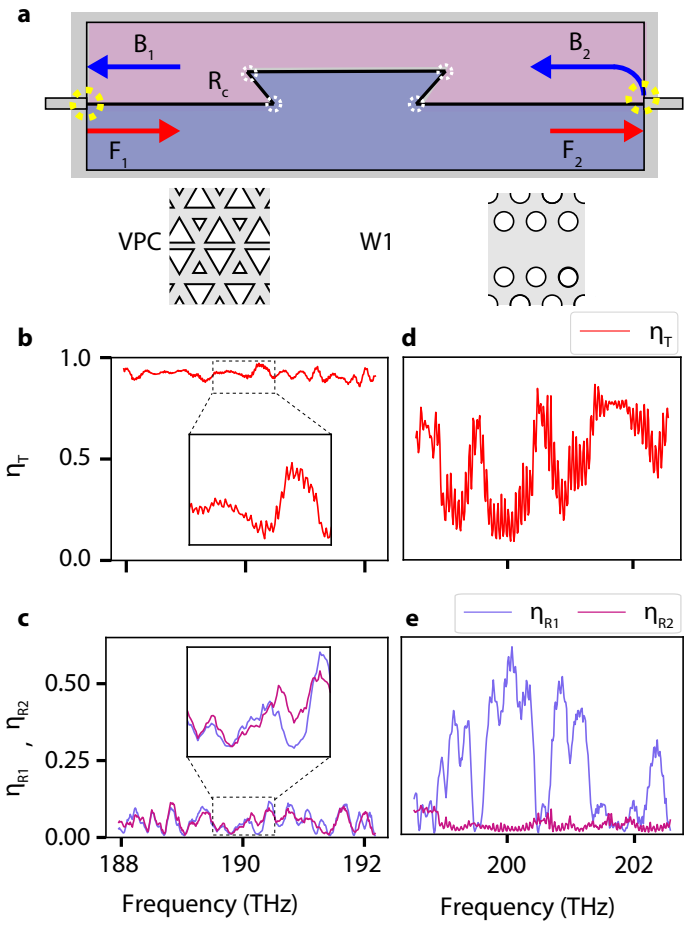


Figure 4.4: Degree of topological protection. (a) Schematic of the mode contributions in a Ω-shaped defect VPC waveguide. Red arrows indicate the forward propagating modes, with $F1$ and $F2$ denoting the modes before and after the defect, respectively. Blue arrows indicate backward propagating modes before ($B1$) and after ($B2$) the defect. Yellow dashed circles show the locations of in- and outcoupling- facets. White dashed circles indicate the four 120° corners. (b) Plot of the transmission coefficient η_T, with the inset demonstrating transmission over a small region ([189.5 THz – 190.5 THz]). (c) Backward/forward energy ratio before (η_{R1}) and after (η_{R2}) the Ω-shaped defect in the VPC interface. The inset shows how the back-propagation energies before and after the defect are almost indistinguishable over the considered frequency range. (d) and (e) show the corresponding plots of (b) and (c) for the W1 waveguide, respectively.

blue arrows, respectively, in schematic Fig. 4.3a. Fig. 4.3c shows a map of the measured amplitude of the VPC edge mode. By first separating the forward and backward modes through Fourier filtering in k-space based on the group velocity of the edge mode and then performing an inverse Fourier transform, we obtain Fig. 4.3d and e. Fig. 4.3d qualitatively demonstrates that the forward propagating mode exhibits a near-unity transmission through the four bends. The constant amplitude of the backward propagating mode (Fig.

4.3e) also indicates near-unity transmission. This demonstrates that we may attribute the coupling of the forward and backward modes to the termination of the exit PhC waveguide. Put differently, light is seemingly perfectly guided around the Ω-shaped interface, with the transmission being independent of the presence of the defect itself.

This observation is quantified by translating the locally measured amplitudes into mode energy ratios. We filter the Fourier intensity distribution to obtain the forward and backward propagating mode energy before (W_{F1}, W_{B1}) and after the Ω-bend (see Fig. 4.4a). Locally determined transmission through the defect for the linear part of the dispersion is shown in Fig. 4.4b. A mean transmission value $\eta_T = W_{F1}/W_{F2}$ of ≈ 0.92 is obtained for the chosen frequency range. Additionally, the mode energy ratios calculated for the regions before ($\eta_{R1} = W_{B1}/W_{F1}$) and after ($\eta_{R2} = W_{B2}/W_{F2}$) the defect are shown for a frequency range of 4 THz in Fig. 4.4c. We notice that $\eta_{R1}(f)$ and $\eta_{R2}(f)$ are almost indistinguishable. This strongly suggests that the contribution of the four symmetry-protected corners to the back-propagation energy is insignificant with respect to back-scattering at the end facet.

Although expected, one can fully appreciate that the remarkably large transmission over the mode's full frequency range [80, 95, 151] is reasonably atypical by comparing it with the transmission of a topologically trivial standard "W1" PhC waveguide (see Methods for fabrication details). We again introduce a trapezoidal structure in the "W1" waveguide (Fig. 4.3f, g). It is worth mentioning that the fabricated W1 waveguide corners are not optimized for unity transmission at any given frequency [178]. In stark contrast to the forward and backward modes for a VPC (Fig. 4.3d, e), the W1 modes (Fig. 4.3h, i) show significant loss across the defect. Moreover, the normalized backward amplitude map in Fig. 4.3i demonstrates that the dominant reflections already occurred at the first 120° corner. The mode energy here is converted to a back-reflected wave and additionally experiences out-of-plane scattering loss. The η_T measured through the Ω-structure in the W1 PhC, shown in Fig. 4.4d, is on average one-third the η_T observed for the VPC. The strong reflection from the first corner is confirmed by the η_R shown in Fig. 4.4e, where η_{R1} on average is four times higher than η_{R2} in the W1 PhC waveguide. The amplitude oscillations in η_{R1} are a result of Fabry-Perot type modulations and are further discussed in Sec. 4.6 for increasing number of corners.

In addition to the back-reflection from the individual corners, a proper evaluation of propagation along the Ω-shaped defect also takes into account other aspects: out-of-plane scattering losses, scattering at the end facet, and interference due to multiple reflections along the interface. We notice rapid oscillations in $\eta_{R1,2}(f)$ before and after the defect (Fig. 4.4c, e). To disentangle the back-scattering contribution from the aforementioned aspects, we consider the complex scalar mode amplitude of the Bloch wave at different points along the interface. With the assumption of a perfectly mirror-symmetric device, we treat the defect as a single effective interface in a transfer-matrix model (TMM). Using η_R and η_T as input parameters to the model, we quantify the mean reflectance $\overline{R_c}$ of the full defect. Details of the model and the precise extraction method can be found in Sec. 4.5. Applying the model to the data for the topologically protected edge states shown in Fig. 4.4b,c yields a mean effective reflectance for the full defect $\overline{R_c} = 0.002 \pm 0.001$ and an out-of-plane scattering loss $\overline{A_c} = 0.080 \pm 0.002$ for the topologically protected edge states. Furthermore, we determine the average single-corner reflectance $R_c^{\text{single}} = 0.0007$

from the TMM (see Sec. 4.5.3).

The same approach applied to the data in Fig. 4.4d, e for the W1 PhC waveguide reveals a reflectance $\overline{R_c} = 0.191 \pm 0.010$, two orders of magnitude larger than that observed for the VPC, and an out-of-plane scattering coefficient $\overline{A_c} = 0.304 \pm 0.017$. These values for the W1 structure are in good agreement with values in the literature [179–181]. A topologically protected PhC lattice thus reduces the experimentally achievable back-reflection from individual sharp corners by two orders of magnitude over the entire frequency range of the edge state. We confirm this finding and the applicability of the introduced TMM using finite-difference time-domain simulations for the same lattice designs with increasing numbers of corners (see Sec. 4.5), further corroborating the discovered experimental limits to topological protection. The observation that the numerically extracted corner reflectance for the VPC is even lower than the experimentally determined reflectance suggests that we measure the effect of C3 symmetry-breaking disorder in the fabricated structure.

4.5. QUANTIFICATION OF CORNER REFLECTIVITY AND LOSS

We quantify the back-scattering of topologically protected edge states - bound to a VPC interface - from an Ω-shaped defect of four 120° corners (cf. Fig. 4.3b of Sec. 4.4) by comparing the measured forward and backward propagating energies before and after the defect to an analytical model. We introduce a transfer matrix model (TMM) approach and compare its results to the back-scattering observed in a similarly shaped W1-type photonic crystal waveguide, which is based on one missing row of holes in a hexagonal lattice. We extract the reflection coefficient R_c^{single} of an individual corner in the waveguide as a quantitative measure of back-scattering and quantify the associated loss A_c^{single} which is dominated by out-of-plane scattering.

4.5.1. TRANSFER MATRIX MODEL

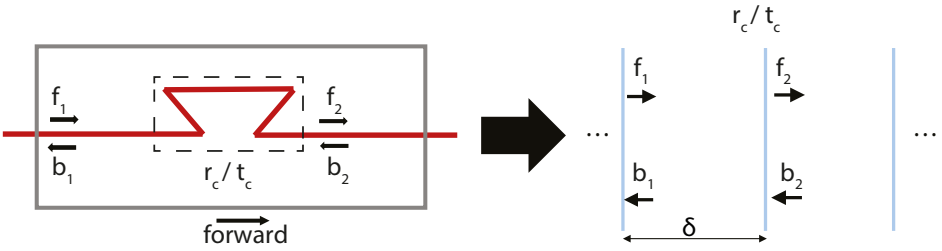


Figure 4.5: Sketch of the experimentally investigated VPC with an Ω-shaped interface defect, as well as its representation within a transfer matrix model. The effect of the Ω-shaped defect on the field amplitudes is approximated by complex reflection and transmission coefficients r_c and t_c, and the distance between the detection points is associated with a propagation phase δ.

To compare the mode at different positions along the interface, we separate a complex

scaling amplitude a_k from the Bloch mode's periodic distribution, resulting in

$$\mathbf{E}_{k_x}(\mathbf{r}) = a_k e^{\imath k_x x} \cdot \mathbf{u}'_{k_x}(\mathbf{r}), \tag{4.1}$$

with $\mathbf{u}'_{k_x}$ a fixed function, independent of the unit cell or time at which the mode field is evaluated. The full spatial information in each unit cell is thus effectively reduced to the scalar complex amplitude value a_k. The complex amplitude together with the reciprocal nature of the employed photonic crystals enables us to describe back-scattering sites along the interface with complex amplitude reflection and transmission coefficients r_c and t_c, respectively. Furthermore, we introduce a loss channel A_c, incorporating out-of-plane scattering losses, via

$$R_c + T_c = 1 - A_c\,, \tag{4.2}$$

where $R_c = |r_c|^2$, $T_c = |t_c|^2$.

Without loss of generality, we consider the forward and backward propagating field amplitudes f_1, f_2, and b_1, b_2 to denote the value of a_k at specific positions on the sample as shown in Fig. 4.5 and get

$$b_1 = r_c f_1\, e^{i2\delta} + t_c b_2\, e^{i\delta} \tag{4.3}$$

$$f_2 = t_c f_1\, e^{i\delta} + r_c b_2\,, \tag{4.4}$$

with the propagation phase $\delta = k \cdot d$ given by the wavenumber k and distance d between the two detection points 1 and 2, which are placed immediately after an interface. Eq. (4.3) and Eq. (4.4) can be cast into the compact form

$$\begin{pmatrix} f_1 \\ b_1 \end{pmatrix} = \mathbf{M}_c \begin{pmatrix} f_2 \\ b_2 \end{pmatrix}, \tag{4.5}$$

where

$$\mathbf{M}_c = \frac{1}{t_c} \begin{pmatrix} e^{-i\delta} & 0 \\ 0 & e^{i\delta} \end{pmatrix} \begin{pmatrix} 1 & -r_c \\ r_c & t_c^2 - r_c^2 \end{pmatrix} \tag{4.6}$$

is the transfer matrix describing light propagation from position 1 to 2 in the multilayer stack. The propagation through a series of N layers can then be written as a single matrix $\tilde{M}$, given by

$$\tilde{\mathbf{M}} = \prod_{i=1}^{N} \mathbf{M}_i\,. \tag{4.7}$$

Here, $\mathbf{M}_i$ is the transfer matrices of the individual layers (with corresponding distances and reflection/transmission coefficients).

It is straightforward to relate any field amplitudes in a TMM to each other by appropriate transfer matrix multiplications. The experimentally determined energy densities on which we base our analysis are given by $F_n = |f_n|^2$, $B_n = |b_n|^2$ $(n = 1, 2)$ and are repeated from Fig. 4.4b-e of the main manuscript in Fig. 4.6 over an excitation frequency window

of ca. 4 THz. If we want to achieve a full overlap of these energy densities with predictions from the TMM model, we not only need to take into account the four 120° corners of the tailored topologically protected defect but additionally all scattering sites after the defect. These include scattering at the transition from the VPC interface to an intermediate PhC waveguide, the subsequent transition to a silicon strip waveguide, and scattering at potential fabrication defects. Since these additional interfaces are not protected by the mirror symmetry of the VPC lattice, it is expected that their reflection coefficients dominate the entire system.

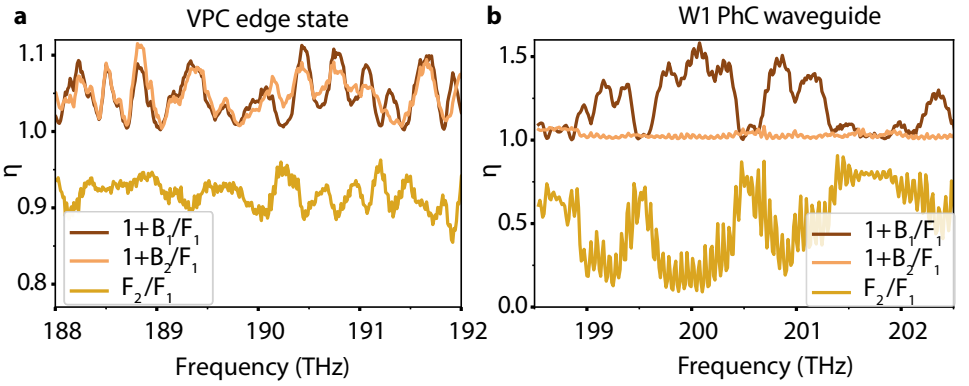


Figure 4.6: Experimentally retrieved energy of the forward (F_2) and backward (B_1, B_2) propagating modes before and after the Ω-shaped defect, normalized to F_1. The backward mode intensities are shifted by 1 for better visibility. (a) VPC edge state. (b) W1 waveguide.

4.5.2. EFFECTIVE CORNER REFLECTIVITY

Our aim is to arrive at a relation between the measured energy densities before and after the defect, and the intensity reflection coefficient R_c and loss A_c. If we, in fair approximation, assume our devices to be mirror-symmetric (as by design), reciprocity dictates equal coefficients for forward and backward propagation through the full Ω-shaped defect. We can thus combine the four individual corners into a single effective interface with complex amplitude reflection and transmission coefficients r_c and t_c (see Fig. 4.5). We divide Eq. (4.3) and Eq. (4.4) by f_1 and take the absolute square to obtain

$$\frac{B_1}{F_1} = R_c + \frac{B_2}{F_1}\,T_c + \left(\sqrt{R_c}e^{-i\theta_{r_c}}\,\sqrt{T_c}e^{i\theta_{t_c}}\,\sqrt{\frac{B_2}{F_1}}e^{i\theta_{b_2}}\,e^{-i\theta_{f_1}} + c.c.\right)$$

$$= R_c + \frac{B_2}{F_1}\,T_c + 2\sqrt{R_c\,T_c\,B_2\,F_1}\cos(\theta_c - \theta) \tag{4.8}$$

$$\frac{F_2}{F_1} = T_c + \frac{B_2}{F_1}\,R_c + 2\sqrt{R_c\,T_c\,\frac{B_2}{F_1}}\;\cos(\theta_c + \theta)\,. \tag{4.9}$$

Here, $c.c.$ denotes the complex conjugate and we express complex quantities in their polar form ($z = \sqrt{Z}e^{i\theta_z}$), with the phase differences $\theta_c = \theta_{r_c} - \theta_{t_c}$ and $\theta = \theta_{b_2} - \theta_{f_1}$. Using

Eq. (4.2), we cast Eq. (4.8) and Eq. (4.9) into the form

$$\frac{B_1 - B_2}{F_1 - B_2} = R_c - \frac{A_c B_2 - 2\sqrt{R_c(1-R_c)F_1 B_2}}{F_1 - B_2}\cos(\theta_c - \theta) \tag{4.10}$$

$$\frac{F_1 - F_2}{F_1 - B_2} = R_c + \frac{A_c F_1 - 2\sqrt{R_c(1-R_c)F_1 B_2}}{F_1 - B_2}\cos(\theta_c + \theta)\,. \tag{4.11}$$

Eq. (4.10) and Eq. (4.11) represent the central result of the TMM analysis, and the corresponding data is presented in Fig. 4.7.

Due to the expected strong influence of scattering events from outside the topological photonic crystal, as seen by the strong correlation between the signals B_1/F_1 and B_2/F_1 in Fig. 4.6a, we utilize an effective averaging approach. Such an approach is based on the linear slope of the VPC edge state dispersion. We can then disentangle the reflection at the tailored Ω-shaped defect from any subsequent back-scattering events by averaging over a frequency range where the interference effects between the latter lead to cosine-like intensity modulations with multiple full periods. Both θ_c and θ in Eq. (4.10) and Eq. (4.11) are oscillatory functions of frequency since they incorporate the propagation phases (cf. Eqs. (4.3), (4.4)). Therefore, by applying a frequency average over the experimental range of ca. 4 THz (denoted by $\langle\cdot\rangle$) to Eq. (4.10) and Eq. (4.11), we average out the cosine modulation and solve for the mean effective defect reflectivity and loss,

$$\langle R_c\rangle = \frac{(\overline{B_1 - B_2})\overline{F}_1 - (\overline{F_1 - F_2})\overline{B_2}}{\overline{F_1} + \overline{B_2}} \tag{4.12}$$

$$\langle A_c\rangle = \frac{(\overline{F_1 - F_2}) - (\overline{B_1 - B_2})}{\overline{F_1} - \overline{B_2}}\,, \tag{4.13}$$

where we defined the operator

$$\bar{\cdot} \equiv \left\langle \frac{\cdot}{F_1 - B_2} \right\rangle, \tag{4.14}$$

and assume no correlation in the spectral behavior of A_c and F_1, B_2. The resulting averages are displayed as straight lines in Fig. 4.7, with their standard deviation indicated by the shaded regions.

4.5.3. SINGLE CORNER REFLECTIVITY

From the mean effective interface values $\langle R_c\rangle$ and $\langle A_c\rangle$ via Eq. (4.12) and Eq. (4.13), we infer an estimate for the coefficients of the individual corners, i.e., when representing each of the four waveguide bends by a single interface in the TMM. The distances between the interfaces are set to the design parameters, as indicated in Fig. 4.5. We model a waveguide with four identical corners, then search for an $\left\langle R_c^{\text{single}}\right\rangle$ such that the mean effective $\langle R_c\rangle$ given by Eq. (4.12) reproduces the value extracted from the experiment. The single corner absorption is subsequently given by

$$\left\langle A_c^{\text{single}}\right\rangle = 1 - \left\langle R_c^{\text{single}}\right\rangle - \sqrt[4]{1 - \langle R_c\rangle - \langle A_c\rangle}\,. \tag{4.15}$$

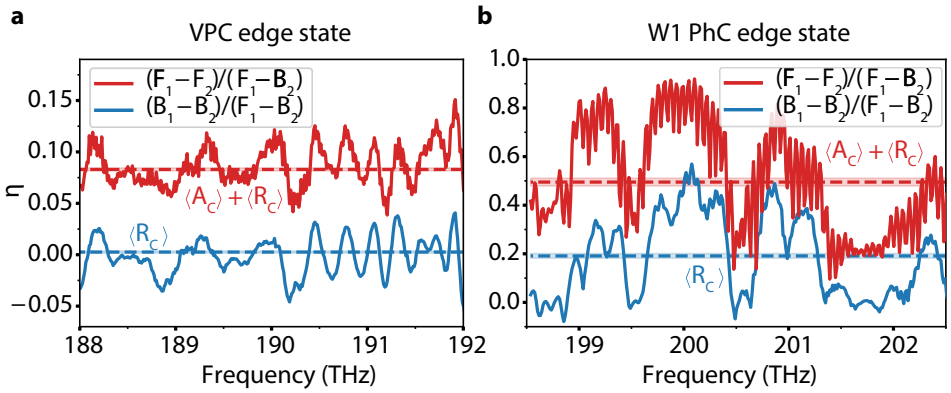


Figure 4.7: Evaluation of Eqs. (4.10), (4.11) for the data shown in Fig. 4.6, where $\langle R_c \rangle$ and $\langle R_c \rangle + \langle A_c \rangle$ according to Eqs. (4.12), (4.13) are indicated as red and blue dashed lines, respectively. The shaded region around the lines corresponds to the standard deviation of the extracted mean values. (a) VPC edge state. (b) W1 waveguide.

	VPC edge state	W1 waveguide
$\langle R_c \rangle$	0.0026 ± 0.0010	0.191 ± 0.010
$\langle A_c \rangle$	0.0804 ± 0.0014	0.304 ± 0.017
$\left\langle R_c^{\text{single}} \right\rangle$	0.0007	0.052
$\left\langle A_c^{\text{single}} \right\rangle$	0.0208	0.105

Table 4.1: Comparison of extracted effective mean corner reflectivity and loss for the Ω-shaped defect within the studied photonic crystal waveguides, as well as the estimates for single corners.

The mean effective parameters extracted from our measurements of the VPC interface and W1 waveguide are displayed in Fig. 4.7 and listed together with the single corner parameters in Tab. 4.1. For the VPC edge state defect, we obtain $\left\langle R_c^{\text{single}} \right\rangle \approx 0.1\%$ and $\left\langle A_c^{\text{single}} \right\rangle \approx 2\%$. While the value of $\left\langle A_c^{\text{single}} \right\rangle$ might seem large for a topological photonic insulator, topological protection is only given for in-plane propagation, with out-of-plane confinement in the silicon slab solely provided by total internal reflection. If we apply the described model to the experimentally measured mode amplitudes of a topologically trivial W1 photonic crystal waveguide, we obtain a corner reflectivity that is two orders of magnitude higher with respect to the topologically protected system ($\left\langle R_c^{\text{single}} \right\rangle \approx 5\%$), while we also see roughly a four-fold increase in out-of-plane scattering ($\left\langle A_c^{\text{single}} \right\rangle \approx 11\%$). Such an increase in losses matches well with the expected scaling behavior with the modes' group velocity of v_g^{-2} [182], with $v_g \approx c/5.8$ for the VPC edge state and $v_g \approx c/10.1$ for the W1 waveguide mode. In consequence, the extracted reduction of back reflection between the two waveguide systems suggests an advantage of topological photonic systems in experimentally achievable conditions.

4.6. INFLUENCE OF CORNERS ON BACKSCATTERING

In order to validate the experimental retrieval of the best estimate for corner reflectivity from the introduced transfer matrix model, we calculated the back-reflected energy densities for different numbers of corners using finite difference time domain simulations (Lumerical FDTD). We construct a VPC interface and W1 photonic crystal waveguide with the same dimensions and a similar in-coupling scheme as used in the experiment. The lattice constant a and sizes of the triangular holes in the unit cell of the VPC were thus chosen as $a = 500\,\text{nm}$, $d_1 = 0.70a$ and $d_2 = 0.45a$, while the W1 waveguide was constructed with a lattice constant of $a = 420\,\text{nm}$ and hole radius of $r = 120\,\text{nm}$. To reduce the computational cost for the simulations, 2D calculations were performed with effective refractive indices adapted to approximately match the experimentally retrieved band gaps around $190 - 200\,\text{THz}$. In this configuration, out-of-plane scattering is absent in the simulations in contrast to the experiment. We utilize a broadband source in the feed waveguide to launch a pulse with a spectral range of $1450\,\text{nm} - 1650\,\text{nm}$ and temporal width of $\Delta t \approx 40\,\text{fs}$. The simulation domain was encapsulated by perfectly matched layers (PMLs) with sufficient thickness to minimize unwanted reflections at the domain boundaries, and the simulation was performed for 10 ps to allow for the pulse energy to adequately decay in the PMLs.

The in-plane electric field components over an area of 20×20 unit cells along the interface/waveguide before the corner(s) were subsequently extracted (see Fig. 4.8a-c for the different defect configurations) and used to calculate the mode energy of the forward (F_1) and backward (B_1) traveling edge state or waveguide mode via their dispersion relation, analog to the experimental realization. The resulting energy ratio $\eta_{R_1} = B_1/F_1$ is shown for the three different configurations in Fig. 4.8a-c on a logarithmic scale to compare the QVHE-emulating VPC and W1 PhC waveguide for each configuration, as well as in Fig. 4.8d,e on a linear scale to follow the evolution of the two modes with an increasing amount of corners. In the case of two and four 120° corners, the field energies F_2, B_2 were additionally extracted from a similar area after the defect.

Looking at the variation in the energy ratio, we observe that the oscillation amplitude of the back-reflected mode energy increases as the amount of interface corners is increased. In addition, the interference between the different corners leads to a distinct Fabry-Perot-type modulation pattern for the W1 waveguide (Fig. 4.8e), while an increase of contributing oscillation periods can be seen for the VPC edge (Fig. 4.8d). The nearly flat reflection coefficient for a single corner in the W1 waveguide of $\langle \eta_{R_c} \rangle = 0.288$ highlights the dominating influence of the W1 corner over other sources of backscattering, while the modulation seen in the VPC edge data for a single corner hints at a comparable backscattering strength from the corner and the PMLs terminating the simulation domain.

Further evaluating the determined energy ratios via the transfer matrix model of Sec. 4.5, we retrieve an effective full reflectivity of $\langle R_c \rangle = [0.2, 1.4, 3.9] \cdot 10^{-5}$ for a system containing 1, 2 and 4 corners along the VPC interface, respectively. The W1 waveguide system exhibits $\langle R_c \rangle = [0.288, 0.443, 0.571]$ for the same configurations. The relative low reflectivity for the VPC suggests that in addition to backscattering caused by the introduced defects, the backward propagating mode energy is affected by numerical as well as meshing artifacts in the simulations. These are negligible for the W1 simulations,

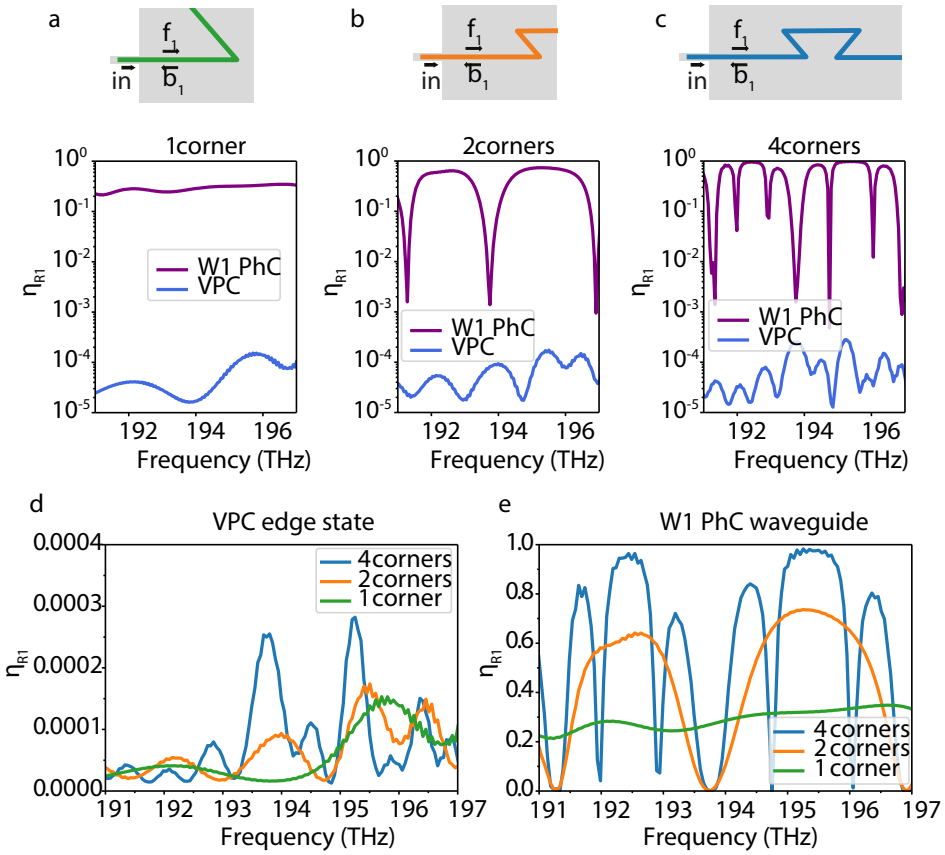


Figure 4.8: Numerically calculated energy ratio $\eta_{R_1} = \frac{B_1}{F_1}$ of the backward (B_1) and forward (F_1) propagating mode for different configurations of the guiding channel. A schematic of the simulation setup is shown above the corresponding ratio of a VPC edge state and W1 waveguide mode for (a) a single 120° corner, (b) two corners (Z-shaped defect) and (c) four corners (Ω-shaped defect), where the mode amplitudes f_1 and b_1 are extracted from an area of 20×20 unit cells. To visualize the four orders of magnitude difference, the retrieved energy ratio is plotted on a logarithmic scale. (d) Comparison between the three different scenarios in (a-c) for the VPC edge state, and (e) the W1 PhC waveguide mode.

which show a clear trend of increasing system reflectivity with a number of corners. Using the reflectivity $\langle R_c \rangle$ for the W1 waveguide structures with 2 and 4 corners, we can estimate the single-corner reflectivity with the approach of Sec. 4.5.3. This results in $\langle R_c^{\text{single}} \rangle = [0.285, 0.284]$ for the two- and four-corner system. This is in good agreement with the reflectivity $\langle R_c \rangle = 0.288$ that was calculated directly for a single-corner system, corroborating the approach of Sec. 4.5.3 to estimate single-corner from full-defect reflectivity as we perform in the main text.

The extracted four orders of magnitude difference in reflectivity between the VPC edge state and the W1 waveguide mode highlights the robustness of the former against the

designed four 120° corner defects. While these 2D simulations achieve an additional two orders of magnitude decrease in backscattering as compared to the experiment, we want to emphasize here that no disorder in the position and size of the triangles constituting the VPC unit cells was taken into account in the simulations. Typical state-of-the-art manufacturing techniques allow for the disorder as small as $\sigma \approx 1\,\text{nm}$ [183], which is an order of magnitude larger than the grid size chosen in the shown numerical calculations. The discrepancy between experimentally determined and numerically extracted corner reflectivity can thus be understood as an indirect measure of the C_3 symmetry-breaking disorder in the experimental system.

4.7. CONCLUSIONS

In summary, a direct experimental quantification of topological protection in VPC-based PTIs at telecom frequencies was achieved by accessing the full complex wavefunction of the edge state via phase-resolved near-field microscopy. This allows for the determination of the back-reflection from topologically protected defects as well as for quantification of the experimentally unavoidable out-of-plane scattering losses. We unambiguously determined an experimental upper limit to the back-scattering contribution from symmetry-protected defects in PhC-based topological edge states. This evaluation opens a direct pathway toward applied quantum topological photonic networks for secure and robust communications.

APPENDIX

4.A. NUMERICAL CALCULATION OF EDGE STATE DISPERSION AND EIGENMODES

The edge state eigenfrequencies $f(k)$, as well as eigenmodes Ek(r) that are localized at the interface between two mirror-symmetric valley photonic crystals (VPCs), were calculated for an in-plane wavevector k with the freely available MIT Photonic Bands solver [184]. It determines the Bloch eigenmodes of the full three-dimensional photonic crystal structure using a plane-wave basis set and periodic boundary conditions. We used a simulation supercell of dimensions $a \times 28a \times 10h$, where h is the thickness of the free-standing silicon slab and a is the lattice constant of the VPC patterned therein. This supercell was sufficiently large to avoid interactions between neighboring supercells in y and z. The calculations used an in-plane grid size of $a/32$ and an out-of-plane grid size of $a/16$, which ensured convergence of the eigenvalues to better than 0.1%. To account for surface passivation effects of the experimentally employed silicon membrane of height $h = 220\,\text{nm}$ and to adapt the resulting eigenfrequencies to the experimentally determined dispersion relation, the effective refractive index of silicon was modeled to be 3.36.

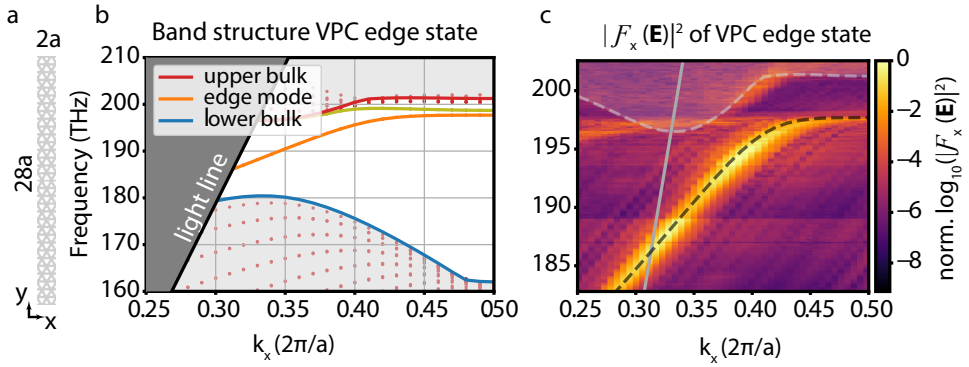


Figure 4.9: Band structure calculations. (a) Geometry of the photonic crystal membrane used in the eigenmode calculations, with grey and white representing silicon and air, respectively. For better visibility, two unit cells are shown along the interface. (b) Numerically calculated band structure of the edge state eigenmode (orange) as well as the upper and lower bulk bands (red and blue, respectively) of the photonic crystal. The light cone is displayed as dark grey shading, while the bulk band region has been shaded light grey. In addition to the topologically non-trivial edge mode, there exists a second mode confined to the edge at large k_x, shown in ochre. (c) Comparison of the fundamental Brillouin zone of the experimentally retrieved dispersion relation and the numerically calculated edge state eigenfrequencies (black dashed line) as well as bulk bands (grey dashed line and shaded region), highlighting the excellent overlap between experiment and simulation. The light line is given by the solid grey line.

The lattice constant was chosen as $a = 503\,\text{nm}$, and the base length of the triangular holes in each unit cell, determined from SEM images, was $d_1 = 0.70a$ and $d_2 = 0.45a$ for the large and small triangles, respectively. Both triangular holes were modeled with a corner rounding of $r = 42\,\text{nm}$ to account for fabrication-related deviations from their ideal structure. We construct a bridge-type interface between two mirror-symmetric

sub-lattices VPC_1 and VPC_2 in the supercell, with the base of the large triangles facing each other. The periodic nature of the simulation subsequently dictates the additional occurrence of the complementary interface (base of small triangles facing each other) at the boundary of the supercell (see Fig. 4.9a). The calculated edge state eigenmodes located at this complementary interface were filtered out, and the resulting band structure for the topologically protected edge state as well as the bulk VPC eigenfrequencies determining the system's band gap are shown in Figure 4.9b. The latter were calculated for a single unit cell of one of the sub-lattices and subsequently mapped to the chosen interface orientation by projecting the resulting bulk frequencies onto the k_x direction. In addition to the edge state traversing the band gap with a linear dispersion around the K-point, a second mode confined to the central interface is found branching off the top bulk band for high in-plane k-values (shown in ochre in Fig. 4.9b). Comparing the calculated band structure to the fundamental Brillouin zone of the experimentally retrieved dispersion relation, an excellent agreement in both position of the band edge as well as edge state dispersion is found, with the mode dispersion of the edge state extending into the light cone for $k_x < 0.31 \cdot 2\pi/a$ (see Fig. 4.9c).

To verify the experimentally determined near-field structure of the edge mode (shown for a wavelength of $\lambda = 1600\,\text{nm}$ in Fig. 4.10a), the field distribution of the eigenstate was extracted from the simulation 20 nm above the silicon membrane. The in-plane field amplitude distribution is displayed for an illustrative k-point of $k_x = 0.32 \cdot 2\pi/a$ in Fig. 4.10b. The corresponding eigenfrequency of the edge state at this k-point is $f = 187.0\,\text{THz}$. It can be seen that the mode symmetries of this numerically determined eigenmode match the mode's in-plane electric field amplitude and the experimentally measured mode distribution.

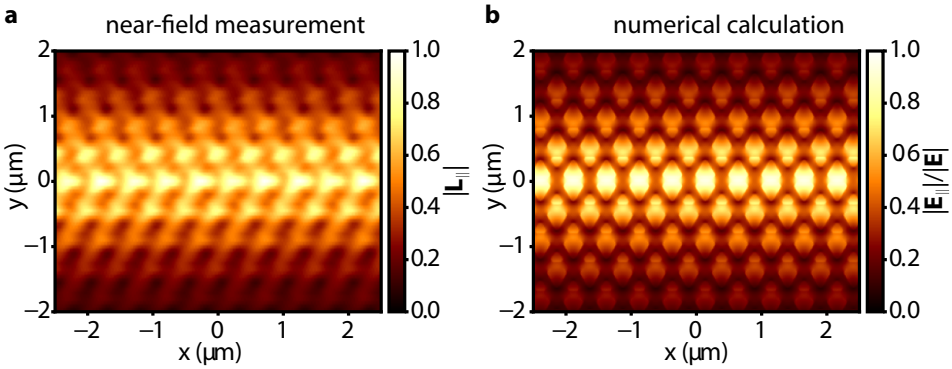


Figure 4.10: Comparison between (a) the experimentally retrieved near-field amplitude map for $\lambda = 1600\,\text{nm}$ ($f = 187.4\,\text{THz}$) and (b) the numerically calculated in-plane electric field distribution of the edge mode at $k_x/(2\pi/a) = 0.32$ ($f = 187.0\,\text{THz}$).

4.B. DISPERSION RELATION OF A W1 WAVEGUIDE

To compare the robustness against reflection from a corner defect between the VPC edge state and a W1-type photonic crystal waveguide, both modes need to be considered at

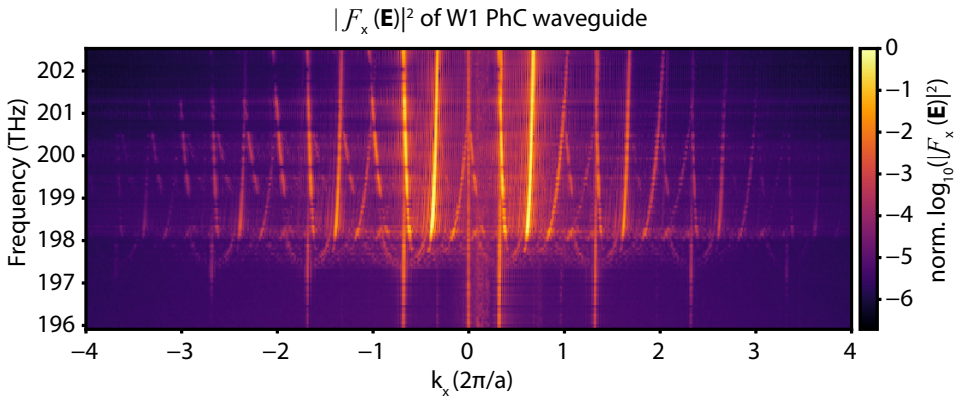


Figure 4.11: Dispersion relation of the fundamental mode of a W1-type photonic crystal waveguide, retrieved via Fourier transforms of near-field maps of the mode while scanning the excitation wavelength. The lattice constant of the investigated photonic crystal is $a = 420\,\text{nm}$, with a hole of radius $r = 120\,\text{nm}$ constituting the unit cell of the hexagonal lattice.

comparable group velocities v_g, since backscattering loss scales with v_g^{-2} [182]. Thus, we experimentally determine the dispersion relation of the W1-type photonic crystal waveguide (analogous to the VPC edge state dispersion from the main manuscript, shown in Fig. 4.2b), and show the bands of forward and backward propagating Bloch modes spanning several Brillouin zones (BZs) in Fig. 4.11. One key observation here is that the forward propagating mode in the fundamental BZ is located at negative k_x, in accordance with the mode's expected behavior [182]. In addition to the predicted band in the forward and backward direction, bands with half and a third of the dispersion slope of the fundamental mode appear. These were already observed in a GaAs-based photonic crystal and attributed to a nonlinear interaction with the scanning near-field probe [185].

5

INTERFACE DEPENDENCE OF TOPOLOGICAL EDGE STATE

There is always light. If only we were brave enough to see it. If only we're brave enough to be it.

[5]Amanda Gorman

In this chapter, we study the effect of edge geometry transformation on topological edge states in Valley Hall effect emulating photonic crystals. We experimentally show that a glide transformation of the interface can open a finite mode gap and lead to slow light inside the Brillouin zone close to the Dirac point. Simulation results indicate that the transformation also weakens the robustness of the edge state against valley-conserving disorder. This work suggests that interface geometry in addition to the bulk-edge correspondence has a direct influence on the existence of valley-polarized edge modes.

Parts of this chapter have been published as a preprint [186]

5.1. INTRODUCTION

A fundamental property of a topological photonic crystal (TPC) interface is the occurrence of a photonic eigenmode with its electric field localized transversely along the interface of two semi-infinite lattices with the dispersion of the mode traversing a nontrivial band gap [11, 80, 88]. The number of topological edge states (TES) is governed by the bulk-boundary correspondence [11, 67–70]. By engineering the bulk of a TPC, TES associated with various topological orders has been realized with different levels of robustness [88, 95, 165, 187–190]. For nonreciprocal TPCs, such as gyromagnetic photonic crystals [73, 79], the existence of TES is guaranteed by the topological order in bulk [79, 164]. For C_6-symmetric TPCs [88, 149], the topological protection of TES is conditional on the conservation of pseudo-spin [88]. When an interface mixes counter-propagating edge states, such as in the case of broken C_6-symmetry at the interface in spin Hall effect emulating TPCs [150, 191], spin-spin scattering results in a gapped dispersion and thereby, is detrimental to the robustness of TES [88]. A similar argument applies to the valley Hall effect emulating photonic crystals (VPCs), where the valley degree of freedom plays the role of pseudo-spin [95, 152, 192, 193]. From the bulk-boundary correspondence, it is widely accepted that a valley-conserving interface should exhibit TES as long as it separates two regions with distinct valley-dependent topologies [95, 194]. Recent studies show that the interface geometry of TPCs can also significantly impact the TES [26, 195–197]. One can, for example, design a chiral interface [133] or ensure broadband low-loss waveguides [198, 199]. However, the bulk-boundary correspondence doesn't fully take into account the relationship between the geometry of the interface and the occurrence and robustness of the edge state [67, 68, 79, 99, 200].

In this chapter, we study the impact of gradually changing the geometry of a VPC interface on edge states in a valley photonic crystal, with a specific focus on the transformation from a zigzag into a glide plane interface. By experimentally measuring the mode dispersion of the glide plane, we observe a finite gap between the upper bulk modes and the edge states (mode gap). Below the mode gap, a region of slow light exists inside the Brillouin zone (BZ), distinct from the slow light regions that occur either at the center or the edge of the BZ [124, 133, 149, 150, 196, 201]. Next, we examine the valley-dependent transport of these edge states by simulating their propagation through a specially designed valley-conserving defect. The calculated transmittance of this defect experiences a significant drop as the geometry of the interface is transformed. This observation suggests that the transformation of the VPC interface disrupts the valley-dependent transport of the edge states.

5.2. GLIDE SHIFT ON VALLEY PHOTONIC CRYSTAL

We start with a VPC interface, similar to the one depicted in Fig. 4.1 (Ch. 4). Here, two distinct VPCs are patterned on a silicon-on-insulator slab. Each unit cell of these VPCs comprises two inequivalent triangular holes, with side lengths of $d_1 = 0.6a$ and $d_2 = 0.4a$, respectively with a lattice constant of $a = 500\,\text{nm}$. The two VPCs are mirror images of each other. As a consequence of bulk-edge correspondence, a difference of $\Delta C_\nu = 1$ in the valley-dependent topological invariant [95, 97, 194] results in an edge state traversing the non-trivial band gap and is robust against perturbations that disallow inter-valley

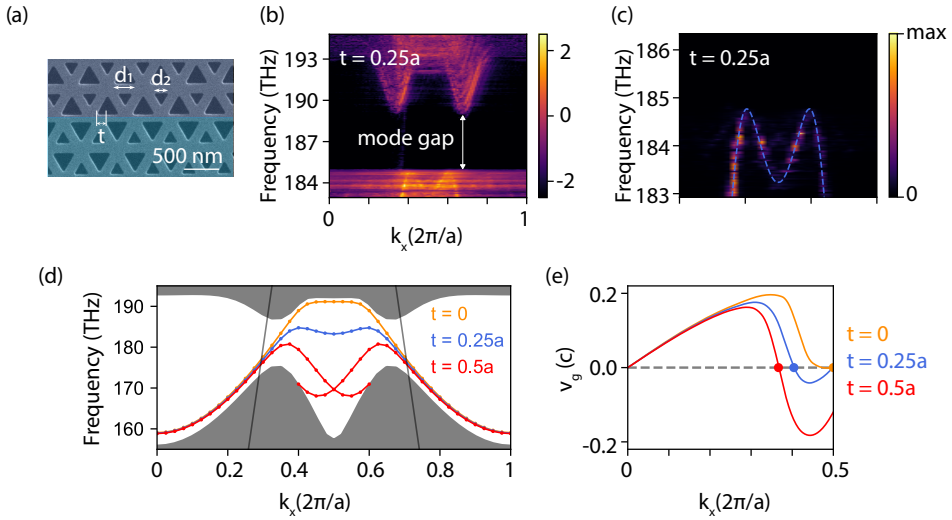


Figure 5.1: Interface geometry and dispersion diagrams. (a) An SEM image of a shifted interface of two distinct VPCs for $t = 0.25a$, with $a = 500\,\text{nm}$ the lattice constant of both VPCs. (b) Experimentally retrieved dispersion diagram of photonic modes of the shifted interface, where $\log_{10}|\mathscr{F}(\mathbf{E})|^2$ is plotted versus k_x and the frequency of excitation. A mode gap arises between the edge states (bottom of graph) and the bulk modes (top of graph). A close-up of the measured dispersion curve of the edge states for a shift of $0.25a$ is shown in (c), where $|\mathscr{F}(\mathbf{E})|^2$ is plotted in a linear scale. The measured dispersion has an M-shape and is consistent with the simulation result (blue-dashed line). Remarkably, there is a slow light region around $k_x = 0.8\pi/a$, which is inside the Brillouin zone rather than at its edge. As a result, the edge state also exhibits both a positive and negative group velocity within half a Brillouin zone. (d) Numerically simulated dispersion curves of edge states for $t = 0$ (orange), $0.25a$ (blue), and $0.5a$ (red). The grey regions represent bulk modes, and the dark line corresponds to the light line $\omega = ck$. As t increases from 0 to $0.5a$, the edge states transform from gapless to gapped. (e) The group velocity of edge states. With an increase in t, a slow-light edge state with $v_g = 0$ transitions from the Brillouin zone edge towards its interior.

scattering [11, 67, 95]. Such an interface between two semi-infinite lattices is known as the zigzag interface with no shift along the direction of the interface ($t = 0$). The maximum achievable shift is $t = 0.5a$ and at this shift, the interface geometry becomes perfectly glide-plane symmetric. To investigate the interface dependence on topological robustness, it is important to consider intermediate shifts as well. Therefore, we examine a mid-point transformation $t = 0.25a$. It is worth noting that shifting the VPC preserves the conservation of valleys since this perturbation does not affect the wavefunction overlap between states at different valleys. Therefore, valley-dependent gapless edge states are still expected to appear at both the shifted interface and the glide plane.

We fabricate three VPC interfaces, corresponding to $t = 0, 0.25a$, and $0.5a$, respectively. The in-plane electric field distribution $\mathbf{E}$ of edge states along these interfaces is measured with phase-sensitive near-field scanning optical microscopy [106]. We apply a spatial Fourier transform $\mathscr{F}(k_x)$ to the measured complex electric field $\mathbf{E}$ for a wavelength range $\lambda = [1480\,\text{nm} - 1640\,\text{nm}]$ to obtain the dispersion relation of the photonic modes [150]. For $t = 0$, we observe edge states with a gapless dispersion curve for the zigzag interface (see Fig. 5.3(a)), as expected from the previous chapter (Ch. 4) [97, 150]. However, as t is

increased the dispersion curve changes dramatically. The measured dispersion diagram of the shifted interface $t = 0.25a$ is shown in Fig. 5.1(b), where $|\mathscr{F}(\mathbf{E}(k_x))|^2$ is plotted with a logarithmic color scale versus k_x for a range of excitation frequencies. We observe that a mode gap opens between 185 THz and 189 THz, which is absent in the dispersion of the zigzag interface [150]. A close-up of the dispersion curve is displayed in Fig. 5.1(c), where $|\mathscr{F}(k_x)|^2$ is also shown with a linear scale. The measured dispersion curve has an M-shape centering at the BZ edge, which is consistent with the simulation result indicated by the white dashed line. This dispersion curve has a zero slope at approximately $k_x = 0.8\pi/a$, demonstrating that slow light occurs within the BZ, where $k_x < \pi/a$. This slow light region is distinct from the typical ones in a photonic crystal waveguide, which usually lies either at the edge ($k_x = \pi/a$) or in the middle ($k_x = 0$) of the BZ [195, 202, 203]. A simple interface deformation with a glide shift can transform gapless edge states into gapped ones. In addition, we present the measured dispersion diagram of photonic modes of the glide plane for $t = 0.5a$ (Fig. 5.3), where edge states are not observed as they fall below the operating frequency range of our laser.

To investigate how the dispersion relation of edge states changes for a glide shift between the VPC interfaces, we numerically simulate the dispersion relations of edge states using finite-element simulations [122], as shown in Fig. 5.1(d). We also present the calculated group velocities of the edge states in Fig. 5.1(e). When $t = 0$ (the zigzag interface), the edge states exhibit a gapless dispersion curve, which becomes almost linear near the valley at $k_x = 2\pi/3a$. The gapless dispersion is a feature of TES and indicates that a change of bulk band topology occurs at the interface [11, 165]. For a shift of $t = 0.25a$, a mode gap appears between the top of the edge states and the bottom of the upper bulk modes. The edge states shift down in frequency towards the BZ edge ($k_x = \pi/a$), creating a slow light region distinctly different from the typical slow light regions in photonic crystals, which occur either at the BZ edge or at the Γ point [195, 202]. The decrease of the group velocity here is due to the emergence of energy vortexes, rather than standing waves [203]. As t increases further to $0.5a$, the mode gap widens, and the slow light region moves closer to the valley at $k_x = 2\pi/3a$. To underpin the gradual change from gapless to gapped edge states, we numerically simulate various interfaces with $t = [0.1 - 0.5] \times a$, and is shown in Fig. 5.4.

5.3. ROBUSTNESS AGAINST VALLEY-CONSERVING DEFECTS

We found that the edge states at the shifted interface have a dispersion relation distinct from those of typical valley-dependent edge states, which cross the band gap around valleys. Usually, valley-dependent transport is demonstrated with backscattering-free propagation through a valley-conserving defect, such as a sharp 120° interface bends [97, 150, 151]. However, in the case of a shifted interface, a sharp bend cannot be realized while preserving the interface geometry. To examine the valley-dependent transport of edge states at interfaces with a glide shift, we propose a valley-conserving lattice defect called an L3 defect. This defect is introduced into a VPC interface by replacing three small triangular holes with three larger ones, as depicted in Fig. 5.2(a). According to first-order perturbation theory, the L3 defect conserves the valley degree of freedom. It is thus ideally suited for testing valley-dependent transport (a mathematical proof is provided in Sec. 5.B).

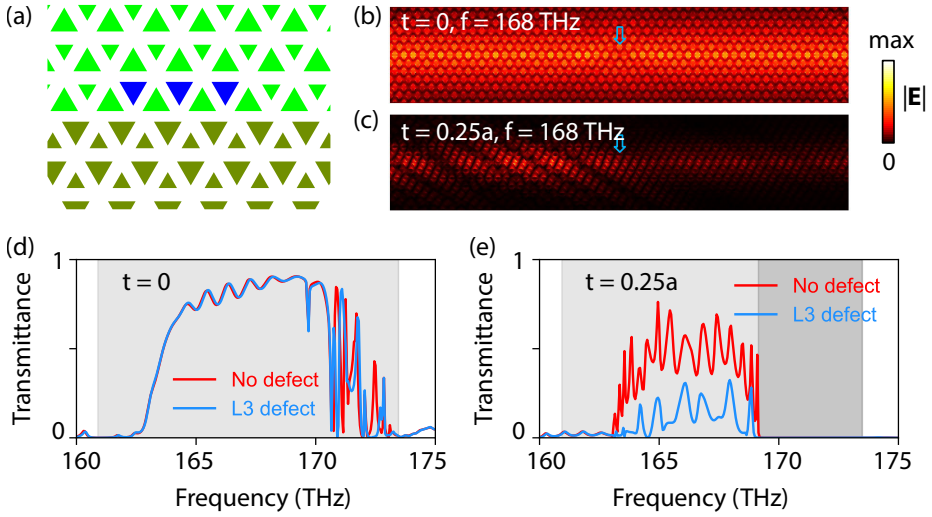


Figure 5.2: Defect and transmittance. a) The geometry of a valley-conserving L3 defect introduced into a shifted interface, with three small triangles replaced by three large ones (blue). b) & c) Simulated electric field amplitude **E** on the zigzag interface ($t = 0$) and the shifted interface ($t = 0.25a$), respectively, at an excitation frequency of 168 THz. The blue arrow indicates the position of the L3 defect. Light enters the VPC interface from the left side and exits from the right side. A decrease in |**E**| at the L3 defect and an interference pattern is observed in c) but not in b), indicating a significant contrast in transmittance before the defect between the two VPC interfaces. The simulated transmittance spectra of the zigzag and shifted interface are presented in d) & e), respectively. The grey domain indicates the band gap, while the dark domain represents the mode gap. The zigzag interface has a transmittance spectrum almost unaffected by the L3 defect. In contrast, the shifted interface exhibits a significant decrease in its transmittance after introducing the L3 defect.

We simulate light propagation along various VPC interfaces using COMSOL Multiphysics® software [122], both with and without an embedded L3 defect. Figs. 5.2(b) and (c) depict the amplitude of the simulated normalized electric field |**E**| of the edge state in the zigzag and shifted interfaces, respectively, for an excitation frequency of $f = 168$ THz. The input port and output ports are located on the left and right sides, respectively. The blue arrow indicates the position of the L3 defect. For the zigzag interface, the electric field amplitude remains almost unchanged after the L3 defect. However, for the shifted interface, the electric field amplitude reduces significantly after light crosses the L3 defect. The interference pattern in Fig. 5.2(c) before the L3 defect is the first indication that light suffers back-reflection at the defect.

The transmittance spectra of the VPC interfaces for two cases, namely $t = 0$ (zigzag interface) and $t = 0.25a$ (shifted interface), are presented in Fig. 5.2(d) and (e), respectively. In these figures, the red line represents the transmittance of the VPC interfaces without the L3 defect, while the blue line corresponds to the transmittance with the L3 defect. The grey region represents the band gap, whereas the dark gray region represents the mode gap. It is worth mentioning that the band gap, which spans from 161 THz to 173 THz, does not match the one displayed in Fig. 5.1(d). This inconsistency can be attributed to

the numerical errors in the two-dimensional simulations for Fig. 5.2. Furthermore, all transmittance curves exhibit frequency-dependent oscillations that stem from inefficient coupling input and output ports (not shown in the figure). For the zigzag interface, in Fig. 5.2(d), the transmittance with and without the defect is near-unity for both cases (red and blue curves), indicating near-perfect light propagation along the interface, even in the presence of a local perturbation. The backscattering of light at the L3 defect is negligible, highlighting the robustness of the edge states along such a valley-conserving defect. In contrast, the transmittance spectra of the shifted interface in the presence of an L3 defect exhibit a significant reduction, as shown by the blue curve in Fig. 5.2(e). Substantial backscattering occurs at the defect suggesting that the edge states at the shifted interface are less robust against this lattice defect. By comparing the transmittance spectra of the zigzag and shifted interfaces, we conclude that the deformations in the VPC interface lead to a reduction in the robustness of the edge state against valley-conserving defects and therefore disrupt valley-dependent transport of the edge states. Our study suggests that the robustness of the edge state against valley-conserving defects is reduced by geometrically deforming the VPC interface even if the bulk and its topological invariants remain the same.

5.4. CONCLUSIONS

In conclusion, the existence of valley-dependent gapless edge states depends not only on the bulk invariants but also on the interface geometry of VPCs. By deforming a VPC interface while preserving the conservation of valleys, through the introduction of a glide shift we observe a transition of the edge states from gapless to gapped. Furthermore, we observe the occurrence of slow light within the Brillouin Zone (BZ), which is distinct from the typical resonant zero-group-velocity modes found at the BZ edge. We demonstrate that the valley-dependent transport of these edge states is disrupted as well. Our results indicate that the valley-dependent gapless edge states are not protected by valley-dependent topology alone. Instead, interface geometry is a critical factor in engineering edge states in VPCs.

APPENDIX

5.A. GRADUAL TRANSITION OF EDGE STATES FROM GAPLESS TO GAPPED

Here, we present additional experiments and simulation results to demonstrate the transition from gapless to gapped as we shift the interface.

5.A.1. EXPERIMENT

Figure 5.3 shows the experimentally measured dispersion relation of the edge state of three VPC interfaces obtained with near-field optical microscopy. For a glide shift $t = 0$, the zigzag interface (in Fig. 5.3(a)), the edge state traverses the full band gap. Around 191.3 THz, we observe a cut-off where the edge mode seemingly stops, as above this frequency lie the upper bulk bands. The zigzag interface exhibits a gapless dispersion as expected [97, 150]. For a shift $t = 0.25a$, Fig. 5.3(b), shows the existence of a mode gap ($\nu = [185\,\text{THz} - 189\,\text{THz}]$), separating the bulk modes (at the top) and the edge states (at the bottom). As the shift increases $t = 0.5a$, the mode gap widens even further, as depicted in Figure 5.3(c). In this case, two valleys reside at the top, representing the bulk modes, while the edge states are not observed since their frequencies fall below the accessible frequency window of the excitation laser.

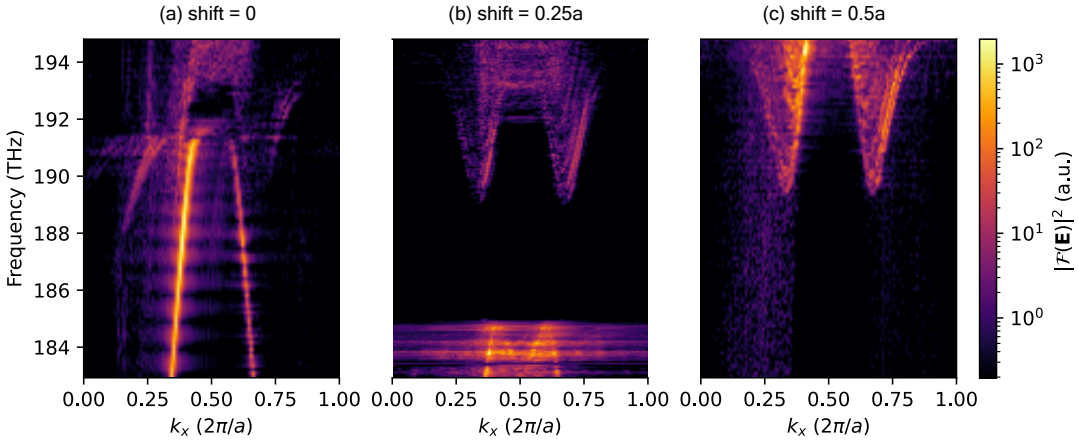


Figure 5.3: Measured mode dispersion of interfaces with three different shifts. As the shift increases, a mode gap opens between the bulk modes (at the top) and the edge states (at the bottom).

5.A.2. SIMULATION

In Fig. 5.4, we present numerically simulated dispersion curves of the edge mode along a glide interface for incremental shifts. The calculations were performed using the COMSOL Multiphysics® software (version 6.1) [122]. The colored lines represent the edge states, while the grey regions correspond to the bulk modes. For a shift of $t = 0$, the numerically simulated dispersion curve of the edge states (blue) overlaps with the upper and lower

bulk modes, indicating a closed gap in the dispersion. However, as the shift of the VPC interface increases to $t = 0.1a$, the edge mode (orange) is pulled down, albeit maintaining the gapless mode. A further increment in the shift results in a mode gap emerging between the edge states (green) and the upper bulk modes (grey). This mode gap becomes more pronounced as the shift is increased to $t > 0.2a$. At the maximum shift $t = 0.5a$, for the perfect glide-plane-symmetric VPC interface, the direction of k_x and the sign of v_g no longer coincide along the edge mode away from the BZ edge. The edge mode becomes degenerate with the lower bulk modes and features a forward and backward propagating mode within the first BZ. These simulation results are consistent with the observations we made in Fig. 5.3. Moreover, we observe two independent edge modes for the glide plane, which is a direct consequence of glide-plane symmetry [204].

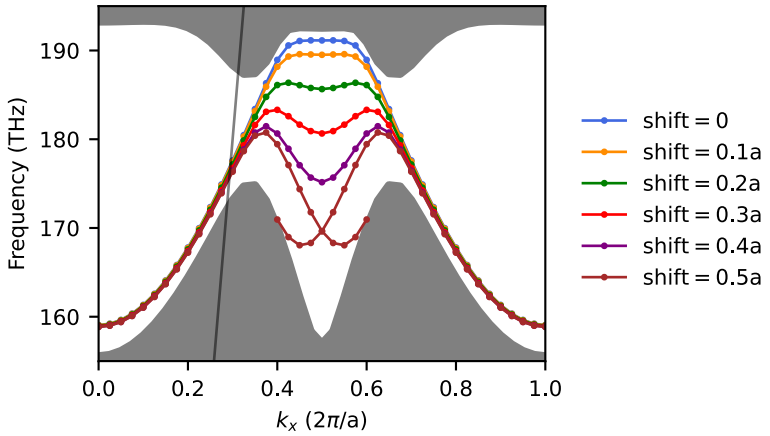


Figure 5.4: Calculated dispersion diagrams of edge modes occurring along VPC interfaces for different shifts. The dark line represents the light line. The grey areas denote the bulk bands.

5.B. PROOF OF VALLEY CONSERVATION AT THE L3 DEFECT

Here, we show that the L3 defect decouples the bulk modes at different valleys. We denote a bulk mode at valley K/K' by $\psi_{K/K'}$. According to Bloch's theorem, these bulk modes can be expressed as the product of a plane wave and a periodic function: $\psi_K = \exp(iK\cdot r)u_K$ and $\psi_{K'} = \exp(iK'\cdot r)u_{K'}$. The coupling strength between ψ_K and $\psi_{K'}$ by the L3 defect, denoted by its perturbation on permittivity $\Delta\epsilon$, is [95]

$$\langle\psi_K|\Delta\epsilon|\psi_{K'}\rangle = \int_V \Delta\epsilon \exp(i(K'-K)\cdot r)u_K^* u_{K'}\,dV = \int_V \Delta\epsilon \exp\left(-i\frac{4\pi}{3a}x\right)u_K^* u_{K'}\,dV. \quad (5.1)$$

We divide the region where $\Delta\epsilon \neq 0$ into three parts, corresponding to the three triangles in the L3 defect: $V = V_1 + V_2 + V_3$. For any $r \in V_1$, note that $\Delta\epsilon u_K^* u_{K'}(r) = \Delta\epsilon u_K^* u_{K'}(r + a\hat{x}) = \Delta\epsilon u_K^* u_{K'}(r + 2a\hat{x})$. Therefore, the expression of coupling strength can be reduced to an

integral over V_1:

$$\begin{aligned}\langle\psi_K|\Delta\epsilon|\psi_{K'}\rangle &= \sum_{n=1}^{3}\int_{V_n}\Delta\epsilon\exp\left(-i\frac{4\pi}{3a}x\right)u_K^* u_{K'}\,dV \\ &= \sum_{n=1}^{3}\int_{V_1}\Delta\epsilon\exp\left(-i\frac{4\pi}{3a}x\right)u_K^* u_{K'}\,dV\exp\left(-i\frac{4\pi(n-1)}{3}\right) \\ &= \int_{V_1}\Delta\epsilon\exp\left(-i\frac{4\pi}{3a}x\right)u_K^* u_{K'}\,dV\sum_{n=1}^{3}\exp\left(-i\frac{4\pi(n-1)}{3}\right) \\ &= 0.\end{aligned} \tag{5.2}$$

This equation shows that the L3 defect does not contribute to the inter-valley coupling. Consequently, the backscattering of valley-polarized edge states by the L3 defect is suppressed. And the converse is also true: any backscattering of edge states by the L3 defect indicates that the edge states are not valley-polarized.

6

MULTIPLE BACKSCATTERING OF PHOTONIC TOPOLOGICAL EDGE STATES

It is paradoxical that tragedy stimulates the spirit of ridicule; because ridicule, I suppose is an attitude of defiance: we must laugh in the face of our helplessness against the forces of nature - or go insane.

[6]Charlie Chaplin

In this chapter, we present an experimental investigation of multiple scattering in photonic-crystal-based topological edge states with and without engineered random disorder. We map the spatial distribution of light as it propagates along a so-called bearded interface between two valley photonic crystals which supports both trivial and non-trivial edge states. As the light slows down and/or the disorder increases, we observe the photonic manifestation of Anderson localization, illustrated by the appearance of localized high-intensity field distributions. We extract the backscattering mean free path (BMFP) as a function of frequency, and thereby group velocity, for a range of geometrically engineered random disorders of different types. For relatively high group velocities (with $n_g < 15$), we observe that the BMFP is an order of magnitude higher for the non-trivial edge state than for the trivial. However, the BMFP for the non-trivial mode decreases rapidly with increasing disorder. As the light slows down the BMFP for the trivial state decreases as expected, but the BMFP for the topological state exhibits a non-conventional dependence on group velocity. Due to the particular dispersion of the topologically non-trivial mode, a range of frequencies exist where two distinct states can have the same group index but exhibit a different BMFP. While the topological mode is not immune to backscattering at the disorder that breaks the protecting crystalline symmetry, it displays a larger robustness

Parts of this chapter have been published as a preprint [205]

than the trivial mode for a specific range of parameters in the same structure. Intriguingly, the topologically non-trivial edge state appears to break the conventional relationship between slowdown and the amount of backscattering.

6.1. INTRODUCTION

Slow light has been known to benefit on-chip photonics through the concomitant increase in light-matter interactions [202, 206, 207]. The much-wanted increased light-matter interaction itself is, however, accompanied by fundamental side effects. No real-life photonic structure is perfect and as the light slows down, imperfections increasingly scatter the propagating light both into the far field and into the counter-propagating mode [208, 209]. Moreover, the fraction of light being backscattered will grow with increased slowdown, inevitably resulting in Anderson localization for one-dimensional systems like waveguides [210, 211]. The advent of crystalline topological insulators in electronic as well as photonic and acoustic systems spurred an investigation into robust transmission channels that are inherently protected from scattering [11, 19]. These systems offer the possibility of topological transport without a magnetic field that breaks time-reversal symmetry. Instead, the protection is directly linked to crystalline symmetry. The realization of photonic analogs consisting of topologically non-trivial photonic crystals (PhCs) [11, 13, 83, 88, 142, 149, 164, 165, 212] with reduced backscattering [73, 213–216] offer passive implementation and the ability for on-chip, nanoscale integration. In the specific case of quantum valley Hall effect emulating systems [95, 97, 150, 151, 217] that operate below the light line, robustness against backscattering relies fully on geometric symmetries. This immediately raises the question to what extent the topological protection holds in the presence of random disorder, which by its very nature destroys the underlying and required symmetry [131, 218].

To address this intriguing question, one must simultaneously consider photonic slowdown and topological robustness. As the propagating light slows down, light becomes more susceptible to backscattering due to a combination of an increase in light-matter interaction and local density of states (proportional to the slow down) that increases the overall scattering at imperfections, and increases the fraction of scattered light into the backward direction which is also proportional to the density of states of the mode and slowdown [209, 219, 220]. Recently, a design called bearded interface has been introduced that offers both a topologically trivial and non-trivial mode within the bandgap of the same silicon-on-insulator device, i.e., with the same unavoidable fabrication-induced disorder [195]. Moreover, this interface offers the prospect of achieving two topologically distinct modes over an extended range of achievable group velocities. Initial transmission measurements have found that the transmission along straight and symmetry-preserving corners of the non-trivial mode was indeed higher than for the trivial mode [133, 195, 221], with losses increasing for slower light. A more recent study on scattering losses due to intrinsic fabrication disorder found no appreciable difference between the robustness of topologically trivial and non-trivial edge states [201] with all losses being enhanced by the slowdown of the propagating light. By observing indications of the onset of Anderson localization, the study suggested the presence of multiple (back)scattering. In all cases, the determination of the group velocity came from simulations. It is important to note that, interestingly, due to small differences in the exact geometrical parameters (relative hole sizes and corner rounding) of the realized photonic crystals, the frequency for which the group velocity is lowest is not equivalent in both investigations: in one it is located inside the non-trivial frequency range [221] and in the other, inside the trivial frequency range [201]. This highlights, that for probing the limits of topological protection, investigations

that use engineered disorder, combined with a local determination of the group velocity would be highly valuable.

In this chapter, we experimentally quantify the robustness of edge states propagating along a bearded interface using a universal metric known as backscattering mean free path (BMFP) [41, 222, 223]. We directly map the spatial distribution of the complex electric field of the edge states with phase-resolved near-field scanning optical microscopy [106, 158]. We first investigate the bearded interface without induced disorder and systematically compare the BMFP of the trivial and non-trivial modes for the same range of group velocities. Subsequently, we study the effect of intentionally induced positional or hole size disorders of various magnitudes. While both trivial and non-trivial waveguides show scattering losses, we observe a different qualitative and quantitative response for the topologically trivial and non-trivial edge states, which depends on the type and magnitude of the disorder. For the largest magnitudes of the disorder, we observe the photonic manifestation of Anderson localization, illustrated by the appearance of localized high-intensity states. Interestingly, we find that the onset of Anderson localization is different for the distinct edge states. We also observe that the conventional direct relation between the slowdown factor and backscattering seemingly breaks down for the topologically non-trivial mode.

6.2. EXPERIMENTAL RESULTS

6.2.1. MAPPING OF THE NEAR-FIELD EDGE STATE

We experimentally investigate edge states at the interface of topological PhCs mimicking the quantum valley Hall effect. A non-vanishing Berry curvature at the valleys is associated with an intrinsic magnetic moment, resulting in a valley Chern number $C_{K,K'} = \pm\frac{1}{2}$ [82, 91, 95, 97, 172, 173, 175, 224, 225]. This gives rise to photonic bulk bands of a topologically non-trivial nature. For a unit cell with underlying C_3 symmetry, there are several ways to realize valley-protected edge state interfaces, akin to edge terminations in a honeycomb lattice structure such as graphene. Edge state modes appear at K and K′ points of the Brillouin zone (BZ) as a consequence of broken lattice symmetry [91, 95, 172, 173, 225] by mirror inversion of the PhC lattices at the interface where $y = 0$. The two valley-protected degenerate eigenmodes traverse the photonic band gap with a linear dispersion. This is referred to as a zigzag interface [82, 97]. The bearded interface combines parity inversion and glide symmetry [195] and the resulting interface enforces a degeneracy at the BZ edge [204] resulting in two eigenmodes in each valley with a slow-light region around the BZ edge. The high-energy eigenmode is attributed to have a trivial nature as it can be observed to 'drop down' from the conduction band when holes at the interface are adiabatically reduced in size [195]. At the same time, the low-energy eigenmode is attributed to be non-trivial. It is observed to exhibit higher transmission through sharp bends in comparison to the high-energy eigenmode, as is expected for a non-trivial edge state [221]. From this point on, the low-energy mode is thus referred to as the non-trivial mode, whereas the high-energy mode is called the trivial mode. The continuous deformation of the interface holes and the resulting glide plane symmetry gives rise to the two eigenmodes bending towards the BZ edge. This results in a slow-light region for both the trivial and non-trivial modes enabling access to different backscattering regimes

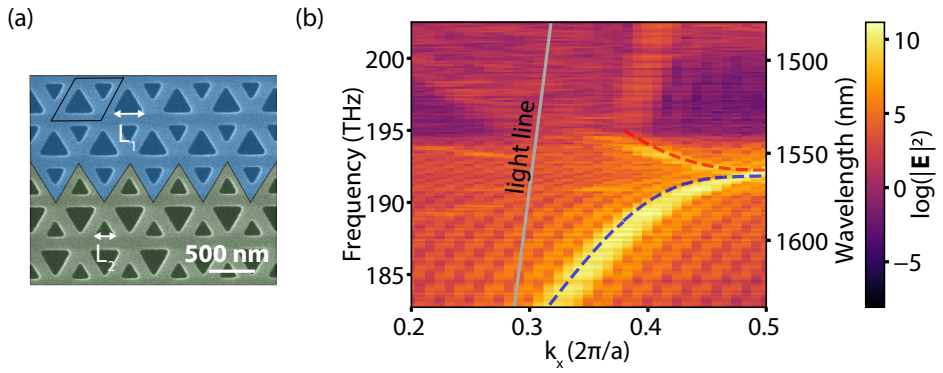


Figure 6.1: (a) Scanning electron micrograph (SEM) of the bearded interface in the fabricated sample with the color-coded regions depicting the two mirror-inverted lattices with glide symmetry (blue and green). The lattice periodicity is $a = 510\,\text{nm}$. (b) Schematic representation of the experimental setup employed to study the near-field of the bearded interface with amplitude and phase resolution. (c) The experimentally measured dispersion diagram of the first Brillouin zone of the edge state in a pristine PhC with two edge modes: at lower frequencies, non-trivial and at higher frequencies, a trivial mode that is degenerate at 1558 nm or 192.4 THz. The blue and red dashed lines indicate the numerically calculated dispersion curves of the non-trivial and trivial modes, respectively.

[226].

We fabricate the bearded interface in a silicon-on-insulator platform (pseudo-colored in SEM image Fig. 6.1(a)). The unit cell with lattice constant $a = 510\,\text{nm}$ consists of equilateral triangular holes with side lengths $L_1 = 0.6a$ and $L_2 = 0.4a$. An interface is created by transforming the triangular holes at the interface of one lattice from L_1 to L_2. We measure the complex in-plane optical fields propagating along the length of the PhC spanning 180 unit cells as a function of laser excitation wavelength $\lambda = [1480\,\text{nm} - 1640\,\text{nm}]$ using phase-sensitive near-field scanning optical microscopy [106]. The employed heterodyne detection scheme allows us to decompose each spatial field map into its Fourier components $\mathcal{F}(k_x, k_y)$. Thus, we obtain the mode dispersion. Figure 6.1(b) shows the dispersion of a bearded interface without any engineered disorder as an example. The region above 194.5 THz represents the start of top bulk bands. Rather than a linear dispersion as supported by the zigzag interface [150], we observe both predicted modes each with a steep linear slope around $k_x = 2\pi/3a$, and also a slow light region close to the Brillouin zone edge ($k_x = \pi/a$). The red (trivial) and blue (non-trivial) dashed outline indicates an excellent correspondence with numerically simulated dispersion curves for the two modes.

6.2.2. VISUALIZING REAL AND RECIPROCAL SPACE OF THE EDGE STATE

We measure the electric field of light that enters the crystal through a feed waveguide and propagates along the interface until it leaves at the end-facet, which serves as a termination of the PhC. An exemplary measured electric field amplitude of a bearded interface without engineered disorder is shown in Fig. 6.7. The end-facet in addition to fabrication

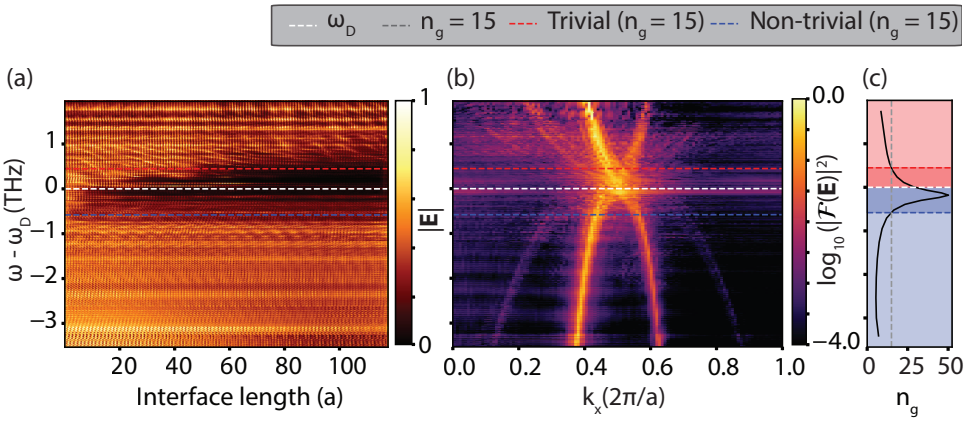


Figure 6.2: Real and reciprocal space of an electromagnetic field of an ensemble-averaged realization of a bearded interface without the intentional disorder. (a) Near-field spatial-spectral amplitude map normalized to the incoupling region collected as a function of frequency and position along the interface. Light propagates the TPC from the left. (b) Ensemble-averaged dispersion curve. The white dashed horizontal line denotes where trivial and non-trivial modes become degenerate at the Brillouin zone edge. (c) Calculated group index curve from the measured ensemble averaged dispersion. The blue and red shaded regions depict the non-trivial and trivial modes separated by the degeneracy point given by the white dashed line at 0 THz. The dark blue and dark red regions indicate the slow light region for the non-trivial and trivial modes with a group index of $n_g > 15$, respectively and the grey dashed line denotes $n_g = 15$

imperfections such as surface and side wall roughness may cause backscattering and create intrinsic loss channels [150, 227]. The procedure that we follow for all spatial-spectral maps in this work includes obtaining an ensemble average of five realizations of bearded interface PhCs with the same magnitude of disorder, summed over modes with the same group velocity [228]. Due to slight variations in nanofabrication, the dispersion relation of individual PhCs may exhibit slight shifts in the degeneracy point ω_D (DP) of the trivial and non-trivial modes. We therefore shift all measurements to ensure that the DPs coincide before averaging. As a consequence, the vertical axis of Fig. 6.2 indicates modified units of frequency in terahertz denoting the frequency difference with respect to that of the DP ($\omega - \omega_D$). The spatial-spectral amplitude map displayed in Fig. 6.2(a) shows the ensemble-averaged electric field amplitude as a function of $\omega - \omega_D$ and interface length (in units of lattice constant a). To account for the excitation-dependent incoupling efficiencies, each horizontal line in the spatial-spectral map is normalized to the mean amplitude of the first four unit cells after the feed waveguide. The corresponding ensemble-averaged dispersion is shown in Fig. 6.2(b). The white dashed line denotes the DP of the trivial and non-trivial mode in the ensemble dispersion at the boundary of the Brillouin zone edge. By fitting a hexic polynomial function (polynomial of degree six) to the measured ensemble-averaged dispersion curve we determine the group velocity as a function of frequency. The extracted group index for the ensemble $n_g = c/v_g$, where c is the speed of light in vacuum and v_g is the group velocity of the measured edge state, is shown in Fig. 6.2(c). More information on this procedure is provided in Sec. III.

For qualitative scrutiny of the ensemble-averaged spatial-spectral map (Fig. 6.2(a)),

we separate the edge mode of the bearded interface into two regimes: fast dispersive ($n_g \leq 15$) and slow diffusive ($n_g > 15$). Below -0.66 THz (blue dashed line), the non-trivial mode has a group index of $n_g \leq 15$. Here, the non-trivial mode retains a nearly uniform amplitude distribution over the entire interface length consistent with unity transmission [150], and the corresponding dispersion shows a positive steep slope within $k_x < \pi/a$. Amplitude oscillations (with a spatial frequency of roughly $2\pi/3a$ and lower) in the spatial-spectral maps arise due to the interference of the backward and forward propagating Bloch modes. As the non-trivial mode enters the diffusive regime ($n_g > 15$) for larger frequencies, the mode nominally slows down further and the amplitude starts to rapidly decay with distance. In reciprocal space (Fig. 6.2(b)) more spatial frequencies appear around the DP. We observe that the non-trivial mode reaches a maximum group index of $n_g = 50$ at $\omega - \omega_D = -0.17$ (shown in Fig. 6.2(c)). Importantly, this maximum group index is found to occur not at the DP but at a lower frequency, i.e., in the frequency range of the non-trivial edge state (see Sec. 6.C.2 and ref. [201]). As we cross over to the trivial region, we observe a gradual decrease of n_g as the frequency is increased away from the BZ edge with a group index $n_g = 30$ at the BZ edge. The influence of unavoidable fabrication-induced disorder on the trivial mode is evident. A clear indication of light undergoing backscattering along the waveguide is visible in the frequency region around the DP. The local high-intensity features are characteristic of Anderson localized modes [229, 230]. Above the red dashed line, where the trivial mode has $n_g \leq 15$, the dispersion is roughly linear. However, multiple interference patterns along the interface are observed in the spatial-spectral maps with a distinct decay, in sharp contrast to the homogeneous distribution of the non-trivial mode with the same n_g range. Thus, from qualitative scrutiny, it is apparent that the trivial edge state suffers more backscattering than the non-trivial edge state.

6.2.3. INTRODUCING RANDOM INTENTIONAL DISORDER

To experimentally unravel the degree of protection that a trivial and non-trivial mode may offer against multiple scattering, we intentionally introduce disorder in the bearded interface PhC design. We engineer two types of intentional disorder: (a) random displacement of the holes and (b) hole size variations. We introduced several magnitudes of disorder for each type of disorder and fabricated five different PhC interface realizations per magnitude. The triangular holes are randomly displaced and deformed in accordance with a normal distribution with standard deviation σ as a measure of position and size disorder. The value of σ is scaled with the lattice constant a and the hole diameters L_1 and L_2 (which are also in units of a) for position disorder and size disorder, respectively. Figure 6.3 shows the ensemble-averaged spatial-spectral amplitude maps for position and size disorders with increasing disorder magnitude $\sigma = [0.0025, 0.005, 0.01, 0.02]$. To account for variations in in-coupling efficiency for different excitation frequencies, each horizontal line on the spatial-spectral maps is also normalized to the mean intensity at the feed waveguide. Qualitatively, the following observations can be made for the non-trivial (bottom) and trivial (top) modes as we increase the magnitude of the engineered disorder. Every ensemble-averaged spatial-spectral map in Fig. 6.3 reveals that the light in the fast non-trivial mode region (the limit denoted by the blue dashed line where $n_g = 15$) exhibits an almost homogeneous spatial profile. Interference of the forward and backward

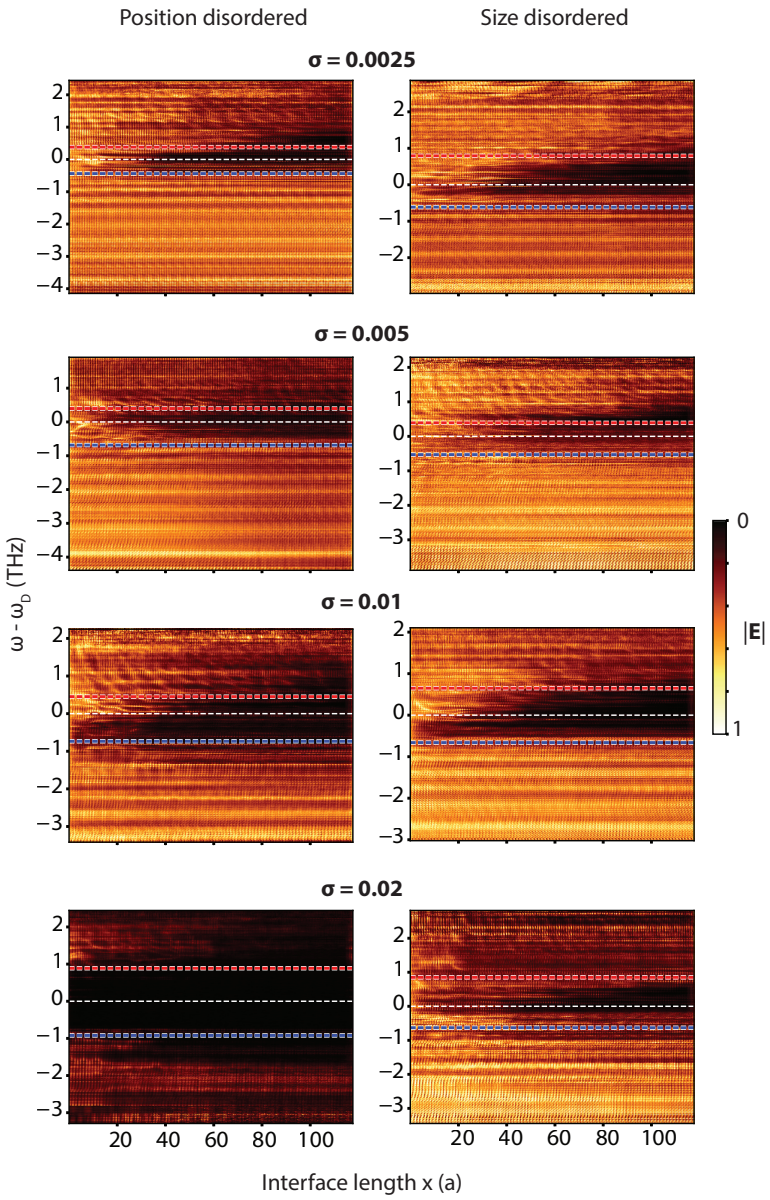


Figure 6.3: Spatial-spectral maps of the measured electrical field amplitude (normalized to the input waveguide) for various degrees of intentionally induced disorder averaged over five realizations of the disorder. The two columns represent position- and size-induced disorder, respectively, as a function of interface length in units of lattice constant $a = 510\,\text{nm}$. The white dashed line denotes DP of trivial and non-trivial mode. The red and blue dashed lines (with a white background for better visibility) denote the frequency away from DP where the trivial and non-trivial mode have a group index of $n_g = 15$, respectively.

modes due to back reflection at the end is evidenced by fast amplitude oscillations. As the frequency is increased into the slow non-trivial region close to the DP, the intensity along the interface rapidly decays to a negligible value. The propagation losses become prevalent and the penetration of the light along the interface decreases. Similar behavior is evident in the slow trivial region below the red dashed line where $n_g = 15$. However, the fast trivial region above the red dashed line looks different than that of the non-trivial mode, showing multiple interference patterns along the interface. In the vicinity of the DP, we observe high-intensity resonances that feature spectral and spatial dependence. These sharp features of intensities are fingerprints of localized states and they become more pronounced as the magnitude of the disorder increases. In general, we observe a rather sharp transition in propagation behavior for the non-trivial region as the mode slows down as the frequency increases, from an edge state that propagates along the entire interface to a state that is hardly able to penetrate the structure. In contrast, the transition in propagation behavior from fast to slow light in the trivial mode is more gradual with frequency. We scale the magnitude of both types of engineered disorder to the lattice constant in a linear fashion. If we use a similar scaling as was used in previous works for both two-dimensional and three-dimensional photonic crystals [42, 131, 231] to compare the effects of different types of disorder, it suggests that the influence of position disorder is more prominent on edge state propagation than size disorder, as evidenced by the slower onset of speckle-like interference patterns in trivial and non-trivial regions.

6.3. QUANTIFYING BACKSCATTERING

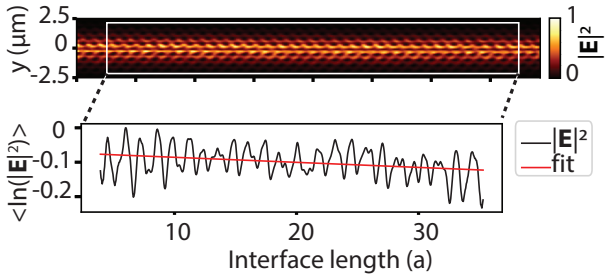


Figure 6.4: (a) Normalized ensemble-averaged electromagnetic field intensity map, averaged over 5 realizations of bearded interface without intentionally induced disorder of the non-trivial mode with integrated over fast light region. Inset: Ensemble-averaged field intensity profile fitted with a linear slope to obtain the backscattering mean free path.

To quantify the robustness to backscattering of the non-trivial mode in comparison to the trivial mode in the bearded interface, we use the backscattering mean free path (BMFP or ξ) as a figure of merit [232, 233]. It is defined as the absolute displacement along the bearded interface after which light suffers (multiple) scattering events in the absence of other loss channels such as absorption [234] or out-of-plane losses. We extract the backscattering mean free path along the interface for an exemplary waveguide as shown

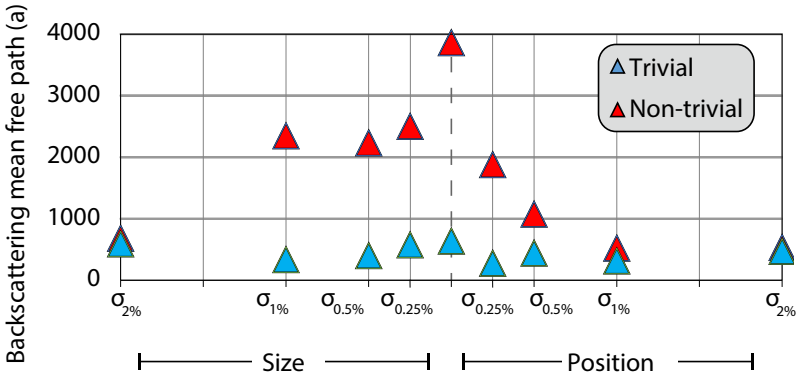


Figure 6.5: Measured backscattering mean free path as a function of intentionally induced disorder. The triangles indicate the measured BMFP from each ensemble averaged disorder realization for the fast non-trivial (red) and fast trivial (blue) modes. The left and right side of the graph represents the fabricated size and position-induced disorder respectively.

in the inset of Fig. 6.4 using the following relation [235]:

$$-\frac{x}{\xi(\omega)} = \left\langle \ln\left[\frac{I(\omega)}{I_0(\omega)}\right]\right\rangle \tag{6.1}$$

where x signifies the distance from the feed waveguide, $\frac{I}{I_0}$ is the normalized electric field intensity, and the brackets indicate the statistical ensemble average over different PhCs with the same type and magnitude of disorder. The frequency (ω) dependence of ξ is stated to differentiate between the contributions of disorder on the non-trivial and trivial modes.

The experimentally determined backscattering mean free path ξ as a function of induced disorder is plotted in Fig. 6.5. The red and blue triangles indicate the BMFP of fast dispersive regimes ($n_g \leq 15$) for trivial and non-trivial modes in the ensemble with an equal group index range, respectively (see Table 6.1 for BMFP values and mean group indices of the trivial and non-trivial regions). For the PhC ensemble with no intentionally engineered disorder (σ_0), the non-trivial mode is more robust to backscattering by an order of magnitude compared to the trivial mode. As the magnitude of the disorder increases, the BMFP for the non-trivial mode drops by almost an order of magnitude for the largest disorder. The decrease in BMFP is strongest for increases in positional disorder. Surprisingly, the trivial mode doesn't suffer a similar reduction and exhibits a BMFP that remains roughly constant with increasing disorder [131]. Importantly, we observe backscattering for all degrees of engineered disorder, and thus symmetry-induced protection partly breaks down due to the induced disorder. However, the non-trivial mode suffers less backscattering than the trivial mode of the waveguide without intentional disorder. This suggests that a certain degree of robustness of the non-trivial mode remains in effect for the studied types and magnitudes of disorder. Nevertheless, the rapid decrease in BMFP does suggest a rapid deterioration of the symmetry-induced protection [218].

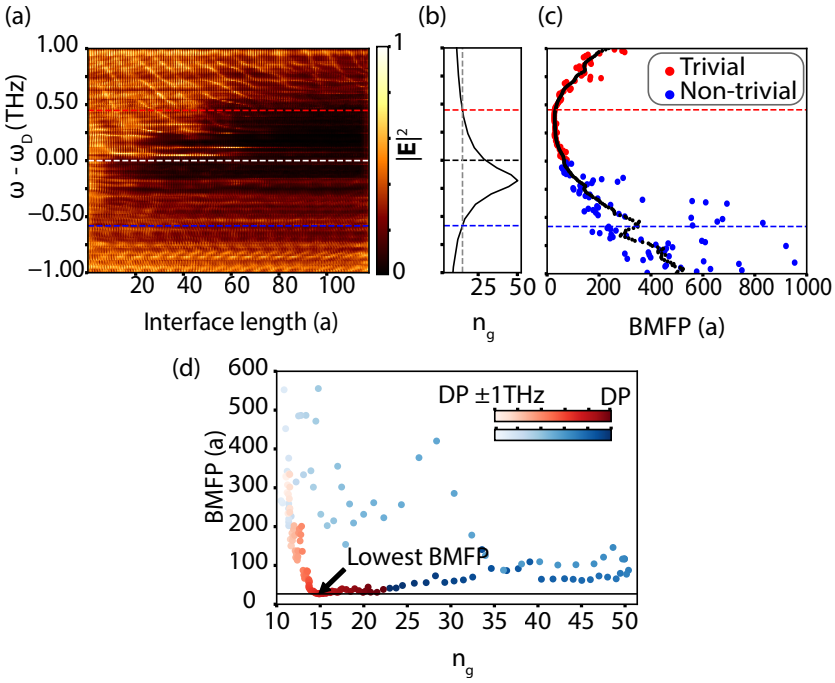


Figure 6.6: Qualitative analysis of the slow light region. a) Zoom-in of Fig. 6.2(a) denoting the spatial-spectral map confined to the slow light region of the two modes. b) Group index curve for the frequencies in the range $[-1,1]$, with the red and blue dashed line denoting the frequencies where $n_g = 15$ for the trivial and non-trivial region, respectively. c) Backscattering mean free path as a function of frequency away from DP. The red and blue points denote the measured BMFP, whereas the black curve denotes the non-trivial and trivial BMFP for a sliding window of width 0.17 THz. It is clear that the minimum BMFP neither occurs at the DP nor the region of the maximum group index. d) Backscattering mean free path as a function of n_g. The blue and red circles denote the non-trivial and trivial mode for a sliding window of width 0.17 THz, respectively. The increasing darkness of the filled circles indicates the relative frequency away from the DP where the darkest red and darkest blue denote the slow light region, whereas light red and light blue denote fast light of the trivial and non-trivial mode, respectively.

At the maximum value of induced disorder, for size and position (2%), the magnitude of the BMFP for the non-trivial and trivial mode is almost the same, suggesting that for the largest disorder, topological protection is destroyed to a greater degree. It is important to note that for the fast non-trivial and trivial mode without the engineered disorder, the deviation in the mean group indices of the two modes is within 1.05% (where $n_g \leq 15$). See Table S1 for BMFP values and mean group indices of the trivial and non-trivial regions of the ensemble. An upper limit of the deviation in the mean group indices of the trivial and non-trivial regions is within 13.39% and it occurs for size disorder 0.5% and does not directly dictate the trend in BMFP. The difference in BMFP observed in Fig. 6.5 of the two fast modes can therefore not be explained by differences in group velocity. The anomalous value of a low BMFP for both non-trivial and trivial mode at size disorder $\sigma_{0.25\%}$ is attributed to limited statistics. Our observation is in agreement with the work in

[131], where the initial introduction of disorder results in a quick reduction of BMFP, and thereafter the decay is slower with an increasing amount of disorder.

6.4. GROUP INDEX CONTRIBUTION TO BACKSCATTERING

A complete understanding of the edge mode's robustness also requires a detailed analysis of the extracted BMFP with respect to light slowing down as defined by the group index n_g. In Fig. 6.6, we show how the two modes' BMFP depend on n_g. For conventional waveguides, ξ is directly linked to the group index as $\xi \propto n_g^{-2}$ for ordinary light propagation [182, 209]. While the concept of a waveguide mode's group index falters in the slow-light regime due to multiple scattering and the diffusive nature of light [226, 233], the nominal n_g is typically still useful to describe the average behavior of the light propagation [202, 236]. From Fig. 6.6(a) we qualitatively investigate the slow diffusive behavior of the two distinct modes for the case without intentional disorder using the ensemble-averaged spatial-spectral mode profile. Around the DP (white dashed line in Fig. 6.6(a) and black dashed line in Fig. 6.6(b)), the propagation losses are significant as evidenced by the small penetration along the interface. The non-trivial mode above the blue dashed line where $n_g > 15$ suffers a discrete drop in intensity as a function of frequency, nonetheless maintaining a homogeneous distribution along the interface (See Fig. 6.12 for the central spatial-spectral map). In contrast, a gradual decay is observed in the trivial mode as we move from the fast to the slow light regime ($n_g > 15$). Figure 6.6(c) and Fig. 6.6(d) show the experimentally determined BMFP as a function of $\omega - \omega_D$ and n_g for the ensemble without the engineered disorder. It is important to note that the occasional occurrence of localization events for a single frequency along the length of the waveguide can result in meaningless values of the BMFP. To reduce the effect of such occurrences on our investigation of the role of slowdown on the BMFP, we use a sliding averaging window with a width of 0.17 THz to obtain a smooth curve denoted by the black circles in Fig. 6.6(c). For BMFP as a function of n_g in Fig. 6.6(d), the smoothed values in the non-trivial region are denoted as blue circles whereas the smoothed values in the trivial region are depicted in red. The increase in shade of the circles indicates the frequency concerning ω_D and therefore also indicates a transition from the fast to the slow light region, with the darkest shade of red and blue denoting the value at the DP. For a narrow range of $10 < n_g < 15$, the fast non-trivial mode has a higher BMFP than the fast trivial mode. It is interesting to note that the lowest BMFP ($\xi = 26.71a$) does not occur at the frequency of the largest group index in the non-trivial region below the DP but occurs when the edge mode lies in the trivial region with $n_g = 15$. When the frequency of the trivial mode decreases further and its slowdown increases as the DP is approached, the BMFP stays roughly constant, if anything increasing slightly. For frequencies lower than the DP where the modes becomes non-trivial a small increase of the BMFP is actually observed as the non-trivial modes slow down further towards the maximal slowdown. At the maximal slowdown of $n_g = 50$, we observe modes propagating through the entire structure with a relatively high BMFP suggesting a degree of robustness against backscattering, a factor of 3.3 larger than that of light in the comparatively faster trivial mode at $n_g = 15$. Beyond the maximal slowdown peak, the group velocity of the non-trivial mode increases again. For these frequencies, the non-trivial modes will have the same n_g as other modes, either trivial or non-trivial, at frequencies away from the DP. Two interesting

observations can be made for these non-trivial modes at frequencies lower than that of the maximal slowdown. First, the conventional relation between slowdown and degree of backscattering holds again. Second, the BMFP of all these modes is always higher than that of the modes above and around the DP with the same n_g, regardless of whether the latter are trivial or non-trivial. We suggest that part of the observed differences in BMFP for modes with the same slowdown could be attributed to an effect of the wavevector change on backscattering: the higher the required wavevector change, the smaller the backscattering. This could explain the differences in BMFP of non-trivial modes with the same group index.

Acknowledging the possible misinterpretation when comparing Fig. 6.6(a) and Fig. 6.6(c), we address the apparent contradiction between the spatial-spectral map and the measured BMFP. When quantifying the BMFP (shown in Fig. 6.6(c)) we find that the minimum BMFP occurs for frequencies just below the red dashed line around 0.39 THz. A cursory glance at the corresponding spatial-spectral map (Fig. 6.6(a)) seems to show a large penetration up to $\approx 55a$ for these frequencies. Conversely, frequencies around -0.08 THz, directly below the DP, seemingly exhibit the smallest penetration in the spatial-spectral map but show a comparatively high BMFP of $\xi = 70.14a$. However, the cursory, visual interpretation of a small penetration in the non-trivial region neglects a much longer intensity tail to the end termination of the PhC. In contrast, the trivial mode around $\omega - \omega_D = 0.39$ THz experiences a drastic reduction in intensity right after the first high-intensity region, even leading to a negligible intensity of light reaching the end termination. This is evident from the spatial-spectral map in the logarithmic intensity scale overlaid on the spatial-spectral amplitude map in Fig. 6.12. These findings emphasize the significance of employing appropriate normalization and background correction methods to accurately discern the true nature of backscattering.

In conclusion, a direct experimental evaluation of backscattering of fast and slow light propagating along a bearded interface between two topological photonic crystals emulating the quantum valley Hall effect has been performed. The spectral and spatial maps of the full interface enable us to completely visualize and probe the appearance of localized events caused by fabrication disorders. Induced disorder in terms of position and size variations affects the electric field distribution in different ways. For the slowest light, we find an indication of Anderson localization at increasing magnitude of disorder illustrated by the localized areas of high light intensity for both the non-trivial and trivial edge states. However, the sensitivity to disorder is found to be different for the two modes for the investigated range of disorder, with the non-trivial mode exhibiting more robustness than the trivial ones. This study sheds light on the potential relevance of topological crystals for on-chip photonic devices for practical applications. We find that all edge states undergo backscattering, regardless of whether they are trivial or non-trivial. Having said that, our observations do indicate that for the same slowdown, topologically non-trivial edge states can exhibit less backscattering than their trivial counterparts. However, the difference is less than an order of magnitude. Both types of edge states will exhibit multiple backscattering as the light is slowed down significantly or when the amount of disorder increases, ultimately leading to Anderson localization.

APPENDIX

6.A. ENGINEERED DISORDER FABRICATION

A total of 45 PhCs were fabricated, with 9 configurations of disorder as

$$\sigma(0) = \text{Without intentional disorder},$$
$$\sigma(pos) = [(0.0025,0),(0.005,0),(0.01,0),(0.02,0)]\,a,$$
$$\sigma(size) = [(0,0.0025),(0,0.005),(0,0.01),(0,0.02)]\,L_1 or L_2$$

where pos and size signify if the disorder induced was a position dislocation or size deformation. The position disorder scales with the lattice constant $a = 510\,\text{nm}$ and the size disorder scales with the relative hole size L_1 or L_2. For each degree of disorder in every bearded interface PhC, the random disorder is drawn using a normal (Gaussian) random number generator. To disregard large deviations in resist thickness, the 45 waveguides were fabricated in the central region of the SOI chip (20 mm × 10 mm), each separated by 100 μm.

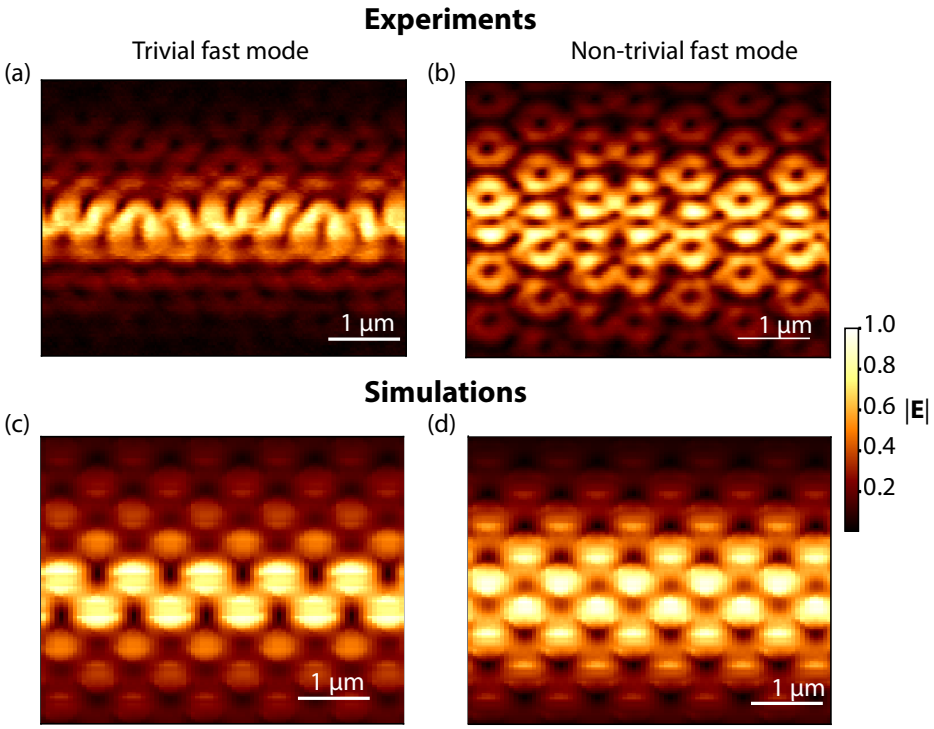


Figure 6.7: Electric field amplitude of (a) trivial and a (b) non-trivial fast mode of a pristine no disorder waveguide far away from the degeneracy point.Trivial mode at 1512 nm and nontrivial mode at 1580 nm. (c) and (d) show the corresponding numerically simulated electric field amplitude

6.B. ELECTRIC FIELD AMPLITUDE/INTENSITY

Fig. 6.7(a) and (b) show the experimentally measured in-plane field amplitude distribution for a trivial and non-trivial edge mode, respectively. It is important to note that the amplitude distribution shown here is from a different bearded interface PhC than discussed in the previous sections. Fig. 6.7(a) shows a trivial fast edge mode at an excitation wavelength $\lambda = 1512\,\text{nm}$ and a non-trivial fast mode at $\lambda = 1580\,\text{nm}$, both measured at an equidistant frequency from the degeneracy point at the edge of the Brillouin zone. For an illustrative k-point of $k_x = 0.40 \cdot 2\pi/a$, where the trivial and non-trivial modes have a linear dispersion with a group velocity of $\approx c/7$, we observe that the mode symmetries of the numerically determined eigenmode of the trivial and non-trivial edge mode match perfectly the experimentally measured mode profile.

6.C. GROUP VELOCITY FITS AND CENTER WAVELENGTHS

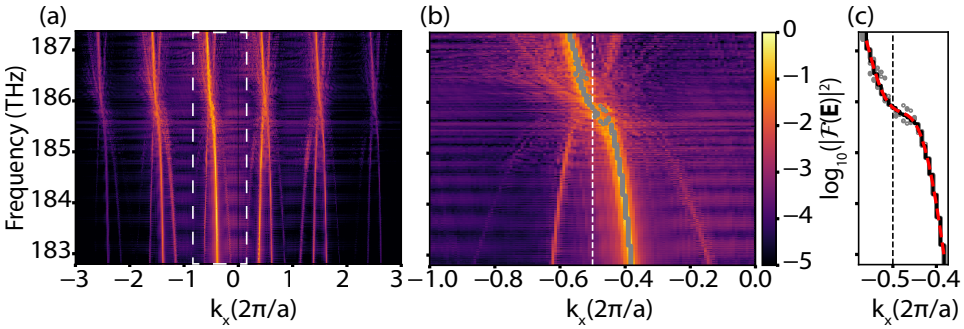


Figure 6.8: Dispersion and edge mode of an individual waveguide. (a) Experimentally retrieved dispersion of the edge mode. Bloch harmonics are separated by $2\pi/a$ with each a trivial and non-trivial edge mode degenerate at the Brillouin zone edge. The Fourier intensity is normalized to the maximum value and results in the $-\pi/a$ BH being the most prominent, as shown in (b). The grey points here denote the peak positions within this irreducible BZ. (c) The black line denotes the median filter applied to the peak positions. The red line denotes a polynomial fit of degree 6.

An ensemble average without engineered random disorder, shown in Fig. 6.2 is built using 5 individual bearded interface measurements. We use an exemplary individual interface, namely WG4 to discuss how the degeneracy points and group index curves were obtained. Using the near-field technique in collection mode, we raster-scan the probe over a length $x = 60\,\mu\text{m}$ along the propagation direction and in the transverse direction $y = 200\,\text{nm}$. We obtain a full dispersion relation of the edge mode by Fourier transforming the electric field intensity for each wavelength in the range $\lambda = [1480\,\text{nm} - 1640\,\text{nm}]$ with a fine step wavelength resolution of 0.1 nm, shown in Fig. 6.8(a). In the obtained spatial frequencies of the light, plotted on a logarithmic scale, we resolve at least six higher-order Bloch harmonics (BH). We obtain a signal-to-background ratio of $21.36\,\text{dB} \pm 0.9$. Since each higher-order BH carries a certain relative amplitude, we select the BH with the highest amplitude (in this case, it lies at $-\pi/a$). For each wavelength, we extract the corresponding wavevector to build the full mode shown as the overlaid grey circles in Fig.

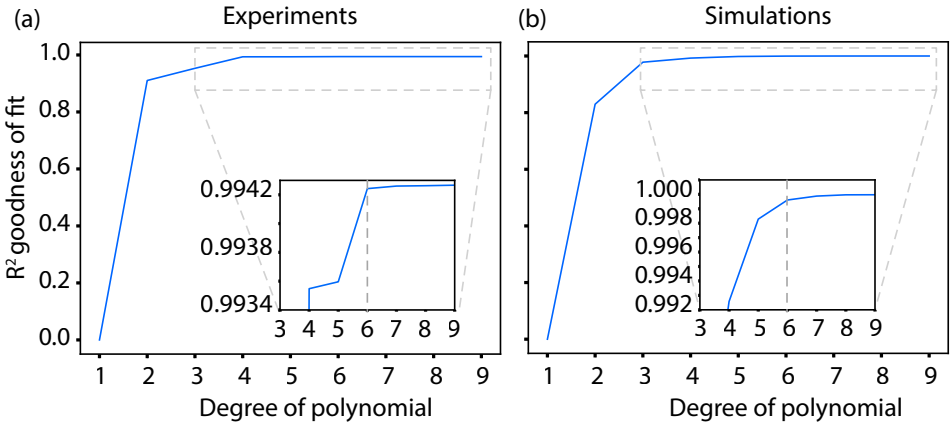


Figure 6.9: Calculated R^2 Goodness of fit for the polynomial fit of degrees 1 – 9 from (a) experimental and (b) numerically simulated dispersion. Inset: zoom-in of the R-squared for the polynomial degree range 3 – 9 to determine the best value for the degree of the polynomial for group velocity fits. The vertical dashed line for polynomial degree 6 shows the chosen value.

6.8(b).

Due to the resolution in k_x and an unclear dispersion around the degeneracy point, we find the median value of the peaks in the dispersion curve (black lines in Fig. 6.8). Since the non-trivial and trivial curves are not symmetric around the BZ edge, a higher degree polynomial is selected. The choice of polynomial undergoes rigorous treatment before a decision is made. We use the coefficient of determination (R^2) as a metric to determine the goodness of the polynomial fit and therefore any discrepancy between observed and modeled values for the polynomial (see Fig. 6.9a). We select a hexic polynomial (degree-6) for which the calculated $R^2 = 0.995$ and the corresponding polynomial fit to the mode's wavevector is shown as a red curve in Fig. 6.8(c). A similar treatment was undergone to the simulations for clarity and confidence (see Fig. 6.9b).

6.C.1. DEGENERACY POINT DETERMINATION

The frequency at which the trivial and non-trivial modes become degenerate slightly shifts in the measured dispersion of individual waveguides due to fabrication imperfection. We identify the degeneracy point, as the intersection where the polynomial converges to the vertical line signifying the end of the Brillouin zone at $k_x = 0.5 \cdot 2\pi/a$, where $a = 0.510$ is determined from SEM images for the fabricated photonic crystals (see Fig. 6.10). The inflection point of the fitted hexic polynomial assigns the wavelength where the sign of the fit undergoes a sign change, and therefore the wavelength at which maximum n_g occurs. This tends to drastically vary for disordered photonic crystals that do not have a clear dispersion curve in the region where the slowdown factor is highest and depends solely on the polynomial fit at the fast light region. We observe an average difference of $1.025\,\text{nm} \pm 0.46\,\text{nm}$ between the inflection and intersection point, for 5 waveguides without the engineered disorder.

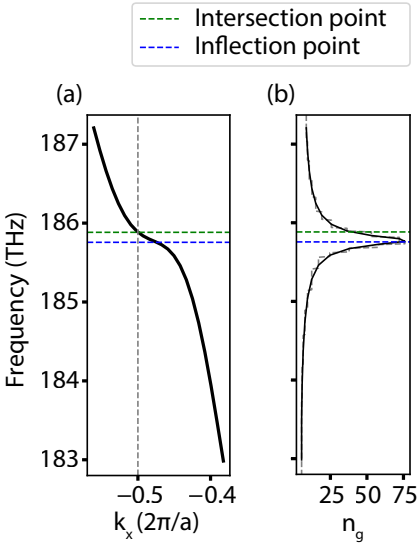


Figure 6.10: Determination of the degeneracy point. (a) 6-degree polynomial fit and the corresponding (b) group index curve. The horizontal green dashed line indicates the intersection point of the fit to $k_x = 0.5 \cdot 2\pi/a$ and the horizontal blue dashed line denotes the inflection point of the fit.

6.C.2. SUBTLETIES IN n_g DETERMINATION

Slight variations in the geometry such as rounding of the corners and the relative sizes of the holes result in changes in the dispersion and therefore variations in the n_g curves as a function of frequency. We find that therefore, the frequency range where the maximum group index occurs can be affected crucially. In Fig. 6.11, we show three numerically simulated dispersion curves and their corresponding group index curves. The parameters used for Fig. 6.11(a) and (b) were 512 nm $L1 = 1.35a/\sqrt{3} = 0.78a$ and $L2 = 0.76a/\sqrt{3} = 0.44a$ and fillet radius of 20 nm. The maximum $n_g = 41$ occurs in the trivial region given by the red curve. This coincides well with the observation reported in ref. [201]. On increasing the roundedness to a fillet radius of 40 nm, while ensuring that the edge modes remain single-mode and do not exhibit intermodal scattering, we observe that the DP shifts to lower frequencies and the edge modes become degenerate around 188 THz (see Fig 6.11(b)). The corresponding group index results in a maximum value very close to the DP with $n_g = 87$. In Fig. 6.11(c), the numerically simulated dispersion for a lattice constant $a = 508$ nm and $L1 = 0.6a$ and $L2 = 0.4a$ show a further reduction in the DP to lower frequencies and the corresponding group index curve features a maximum $n_g = 285$ in the topological region, consistent with the observation in ref. [195] and ref. [221]. It is clear that the relative hole sizes, and the rounding of the triangles due to fabrication variations can consistently shift the maximum n_g obtained and must be taken into account for experimentally realizing topological edge states in the slow-light region.

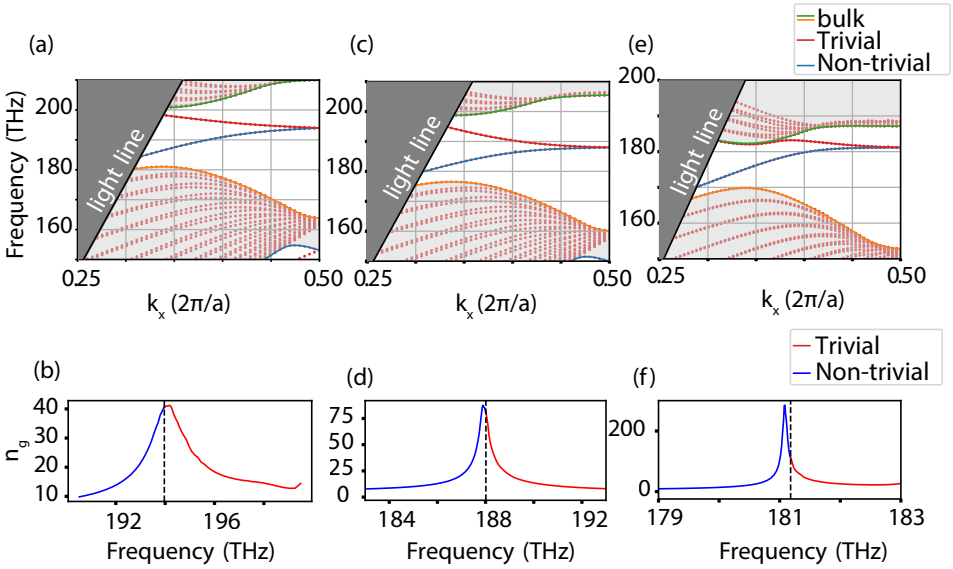


Figure 6.11: Group index curves in the slow light region. (a), (c), (e) Numerically simulated dispersion curves where the maximum group index lies in the (b) trivial region, (d) around the degeneracy point, and (f) non-trivial region, respectively. The parameters for the numerical simulation are $a = 512\,\text{nm}$, $L1 = 1.35a/\sqrt{3} = 0.78a$ and $L2 = 0.76a/\sqrt{3} = 0.44a$, (a) fillet radius $r = 20\,\text{nm}$ and (c) fillet radius $r = 40\,\text{nm}$, and (e) $a = 508\,\text{nm}$, $L1 = 1.04a/\sqrt{3} = 0.6a$ and $L2 = 0.7a/\sqrt{3} = 0.4a$ and , fillet radius $r = 1\,\text{nm}$.

6.C.3. SPATIAL MAP

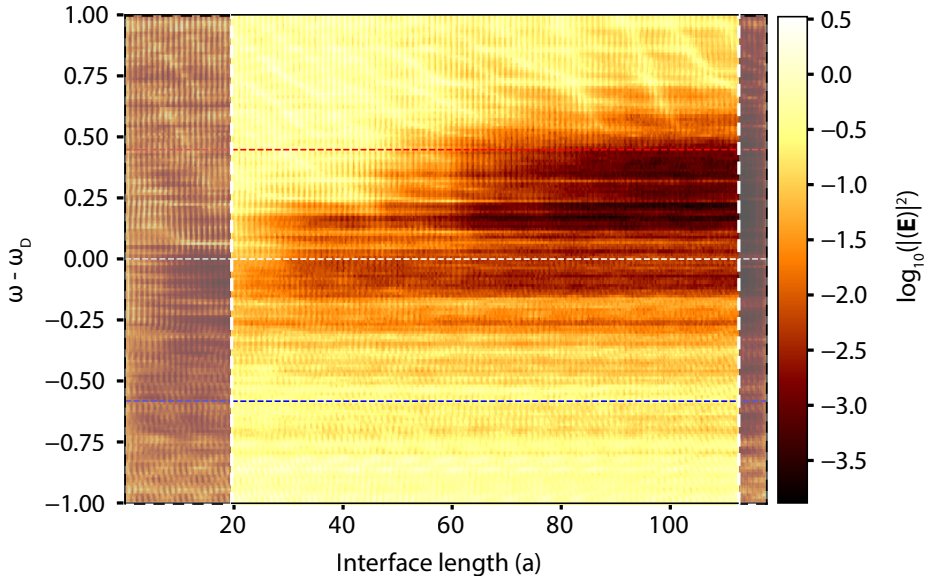


Figure 6.12: Slow light spatial-spectral map. A cropped normalized intensity map on a logarithmic scale is overlaid on top of the spatial-spectral amplitude map shown in Fig. 6a where the cropped interface length is in the range [19.61 – 112.64] in units of a.

6.C.4. CALCULATED BMFP AND MEAN GROUP INDICES

Disorder magnitude	Non-BMFP	Trivial BMFP	Non-trivial $\overline{n_g}$	Trivial $\overline{n_g}$	$\frac{\lvert\Delta n_g\rvert}{\frac{1}{2}(\overline{n_{g,T}}+\overline{n_{g,NT}})}(\%)$
0	3861.44	636.86	10.60	10.71	1.05
Position					
0.25%	1879.33	275.79	9.95	8.90	11.17
0.5%	1074.44	440.83	7.42	8.29	11.17
1 %	520.26	313.88	8.21	7.83	4.75
2 %	532.52	467.98	11.56	11.19	3.28
Size					
0.25%	2501.02	575.71	8.94	9.17	8.27
0.5%	2231.78	400.25	10.19	8.91	13.39
1 %	2346.43	334.34	9.04	9.61	6.07
2 %	680.49	591.04	7.68	6.97	9.70

Table 6.1: Overview of ensemble-averaged calculated BMFPs and group indices for 9 magnitudes of disorders. The columns denote (1) the magnitude of the engineered disorder (position or size), calculated BMFP for the fast (2) non-trivial (NT) and (3) trivial (T) region, mean group index of the fast light range for (4) non-trivial and (5) trivial region, and (6) the deviation of mean group indices.

7

Conclusion

I want to do something splendid... something heroic or wonderful that won't be forgotten after I'm dead. I don't know what, but I'm on the watch for it and mean to astonish you all someday.

[7]Louisa M. Alcott

This thesis delves into the fascinating realm of photonic modes and their behavior when symmetry is imposed on them. Our primary objective was to explore non-trivial photonic crystals, particularly those based on the photonic analog of topological insulators. The journey began in **Chapter 1** with the introduction of one-dimensional (1D) photonic crystals and the fundamental nature of Bloch waves, crucial for unraveling the intricate behavior of light in such crystals. Building upon this understanding, we gradually progressed to two-dimensional (2D) photonic crystals, wherein we discussed the intriguing concept of topological photonic insulators and their degrees of freedom. The focal point of our research lay in exploring topological phases mimicking the Quantum Spin Hall effect (Part I) and the Quantum Valley Hall effect (Part II). These topological phases unveiled novel aspects of light-matter interactions, encompassing spin, helicity, and chirality.

The fabrication of photonic crystals on a silicon-on-insulator platform allowed us to work with telecom wavelengths around 1550 nm (**Chapter 2**). Utilizing near-field experiments, we gained direct access to amplitude, phase, and polarization resolution. Through visualization of the complex and detailed field profile of the photonic edge states, we uncovered essential characteristics that underpin these states such as spin-momentum locking, robustness against sharp corners, valley-conserving defects, and protection to backscattering against engineered random disorder.

We first explore photonic platforms that emulate the quantum spin Hall effect and are characterized by a unique pseudospin. Each topological helical edge state in such systems is directly linked to its designated pseudospin and should unambiguously couple to the matched spin-polarized quantum emitters for on-chip quantum networks. However, as our experiments reveal in **Chapter 3**, the reality isn't so straightforward. The highly structured field of the edge state leads to a strongly spatially varying optical spin density, at subwavelength length scales. In Part II, we explore non-trivial photonic systems based on the valley degree of freedom that offer robust topology-protected transport of optical states along sharp corners, defects, and random disorder. In principle, these edge states occurring at different extremes of the Brillouin zone cannot undergo inter-valley scattering and have the potential of robust on-chip loss-free energy transport. But how robust is robust? In **Chapter 4**, we report an experimental study of quantified robustness in these topologically non-trivial eigenstates on a nanophotonic chip. We find through direct experimental comparison that the amount of back-scattering suffered along the interface in these non-trivial crystals is two orders of magnitude smaller compared to that in a conventional photonic crystal waveguide. This is the case in a zig-zag interface when the two semi-infinite lattices are mirror symmetric. However, this changes when adding a slight shift to the interface. In principle, a shift should not change the valley degree of freedom since the bulk-edge correspondence defining the bulk valley Chern number remains consistent. Even so, we discovered that introducing such a glide shift could disrupt valley-dependent transport, suggesting the *fragility* of such topological photonic systems which is discussed in **Chapter 5**. Furthermore, we explored the reduction in backscattering within topologically non-trivial photonic crystals, a crucial factor when dealing with slowed-down light and increased light-matter interaction. Our thorough analysis in **Chapter 6** demonstrated that adding scatterers affects topological modes more significantly than trivial ones. Nevertheless, for specific parameters, non-trivial modes

can still provide robustness, particularly in slow light systems.

The exploration of topological photonics for scientific curiosity enriches our fundamental understanding of light and its interactions but also paves the way for innovative ideas and breakthroughs in the field. Exploring the limits of topological protection and understanding the effects of disorder, imperfections, and nonlinearity in topological photonic systems are important areas for further inquiry. Studying the robustness of topological edge states against various types of perturbations and exploring strategies to mitigate the impact of imperfections could lead to the design of more resilient photonic devices and communication channels. Unique properties of topological edge modes, such as their strong localization and protection against backscattering, could enhance the efficiency of quantum light-matter interactions and enable the realization of robust quantum communication channels. Therefore, the pursuit of topological photonics for scientific curiosity offers a vast landscape of uncharted possibilities. By investigating exotic topological phases, non-Hermitian systems, quantum photonics, and the impact of the disorder, researchers can unlock new ideas and concepts that may revolutionize the way we manipulate light and harness its potential in future technologies.

Looking ahead, the potential applications of our research extend beyond the telecom regime. Future studies could delve into the optical regime, particularly visible light (400 nm – 700 nm), offering additional advantages such as the integration of two-dimensional semiconductors including molybdenum or tungsten-based dichalcogenides ($MoSe_2$, WSe_2, WSeTe). It is important to note that the choice of the best transition metal dichalcogenide for valleytronic applications depends on the excitonic band gap size and magnitude of spin-orbit splitting. This large splitting allows for selectively populating and manipulating excitons using circularly polarized light. By exploiting propagating optical modes at the interface of non-trivial photonic crystals, we can route the valley excitonic emission of these semiconductor monolayers. The chiral coupling mechanism and spin-momentum locking of polaritons in these topological photonic devices make them promising candidates for creating interface polaritons at room temperature. Investigating the light-matter interaction of topological edge polaritons and measuring the near-field optical spin can pave the way for groundbreaking advances in utilizing photonics and TMDs for novel applications.

BIBLIOGRAPHY

[1] J. K. Alberts, T. K. Nakayama, and J. N. Martin, *Human communication in society* (Allyn & Bacon Boston, MA, 2010) (cited on page 2).

[2] I. Djordjevic, W. Ryan, B. Vasic, I. Djordjevic, W. Ryan, and B. Vasic, *Channel coding for optical channels* (Springer, 2010) (cited on page 2).

[3] D. G. Davis, "The human web: a bird's eye view of world history", Libraries & Culture **40**, 568–569 (2005) (cited on page 2).

[4] M. Arumugam, "Optical fiber communication—an overview", Pramana **57**, 849–869 (2001) (cited on page 2).

[5] S. Kaur, P. Singh, V. Tripathi, and R. Kaur, "Recent trends in wireless and optical fiber communication", Global Transitions Proceedings **3**, 343–348 (2022) (cited on page 2).

[6] D. Kedar and S. Arnon, "Urban optical wireless communication networks: the main challenges and possible solutions", IEEE Communications Magazine **42**, S2–S7 (2004) (cited on page 2).

[7] E. De Tommasi, E. Esposito, S. Romano, A. Crescitelli, V. Di Meo, V. Mocella, G. Zito, and I. Rendina, "Frontiers of light manipulation in natural, metallic, and dielectric nanostructures", La Rivista del Nuovo Cimento **44**, 1–68 (2021) (cited on page 2).

[8] D. K. Gramotnev and S. I. Bozhevolnyi, "Plasmonics beyond the diffraction limit", Nature photonics **4**, 83–91 (2010) (cited on page 2).

[9] I. S. Amiri, S. R. B. Azzuhri, M. A. Jalil, H. M. Hairi, J. Ali, M. Bunruangses, and P. Yupapin, "Introduction to photonics: principles and the most recent applications of microstructures", Micromachines **9**, 452 (2018) (cited on page 2).

[10] G. P. Agrawal, *Fiber-optic communication systems* (John Wiley & Sons, 2012) (cited on page 2).

[11] T. Ozawa, H. M. Price, A. Amo, N. Goldman, M. Hafezi, L. Lu, M. C. Rechtsman, D. Schuster, J. Simon, O. Zilberberg, and I. Carusotto, "Topological photonics", Reviews of Modern Physics **91**, 15006 (2019) (cited on pages 2–3, 7, 54–56, 65).

[12] L. Lu, J. D. Joannopoulos, and M. Soljačić, "Topological photonics", Nature Photonics **8**, 821–829 (2014) (cited on pages 2, 6, 9, 36).

[13] A. B. Khanikaev and G. Shvets, "Two-dimensional topological photonics", Nature photonics **11**, 763–773 (2017) (cited on pages 2, 65).

[14] Y. Ota, K. Takata, T. Ozawa, A. Amo, Z. Jia, B. Kante, M. Notomi, Y. Arakawa, and S. Iwamoto, "Active topological photonics", Nanophotonics **9**, 547–567 (2020) (cited on page 2).

[15] Q. Yan, X. Hu, Y. Fu, C. Lu, C. Fan, Q. Liu, X. Feng, Q. Sun, and Q. Gong, "Quantum topological photonics", Advanced Optical Materials **9**, 2001739 (2021) (cited on page 2).

[16] Y. Wu, C. Li, X. Hu, Y. Ao, Y. Zhao, and Q. Gong, "Applications of topological photonics in integrated photonic devices", Advanced Optical Materials **5**, 1700357 (2017) (cited on page 2).

[17] M. Segev and M. A. Bandres, "Topological photonics: where do we go from here?", Nanophotonics **10**, 425–434 (2020) (cited on page 2).

[18] Z. Chen, H. Buljan, and D. Leykam, "Special issue on "topological photonics and beyond: novel concepts and recent advances"", Light: Science & Applications **9**, 203 (2020) (cited on page 2).

[19] M. Z. Hasan and C. L. Kane, "Colloquium: topological insulators", Rev. Mod. Phys. **82**, 3045–3067 (2010) (cited on pages 2, 6, 24, 65).

[20] X.-L. Qi and S.-C. Zhang, "Topological insulators and superconductors", Rev. Mod. Phys. **83**, 1057–1110 (2011) (cited on page 2).

[21] J. E. Moore, "The birth of topological insulators", Nature **464**, 194–198 (2010) (cited on page 2).

[22] M. Asorey, "Space, matter and topology", Nature Physics **12**, 616–618 (2016) (cited on page 3).

[23] L. Lu, J. D. Joannopoulos, and M. Soljačić, "Topological states in photonic systems", Nature Physics **12**, 626–629 (2016) (cited on page 3).

[24] J. D. Joannopoulos, S. G. Johnson, J. N. Winn, and R. D. Meade, *Molding the flow of light* (2008) (cited on pages 3, 5).

[25] I. S. Nefedov and M. Marciniak, "Photonic crystals", International Conference on Transparent Optical Networks (Cat. No. 99EX350), 133–136 (1999) (cited on page 3).

[26] X. Chen, M. M. Milosevic, S. Stanković, S. Reynolds, T. D. Bucio, K. Li, D. J. Thomson, F. Gardes, and G. T. Reed, "The emergence of silicon photonics as a flexible technology platform", Proceedings of the IEEE **106**, 2101–2116 (2018) (cited on pages 3, 54).

[27] M. Smit, K. Williams, and J. van der Tol, "Past, present, and future of InP-based photonic integration", APL Photonics **4**, 050901 (2019) (cited on page 3).

[28] L. Zhuang, C. G. Roeloffzen, M. Hoekman, K.-J. Boller, and A. J. Lowery, "Programmable photonic signal processor chip for radiofrequency applications", Optica **2**, 854–859 (2015) (cited on page 3).

[29] Y. Shen, N. C. Harris, S. Skirlo, M. Prabhu, T. Baehr-Jones, M. Hochberg, X. Sun, S. Zhao, H. Larochelle, D. Englund, and M. Soljačić, "Deep learning with coherent nanophotonic circuits", Nature photonics **11**, 441–446 (2017) (cited on page 3).

[30] N. C. Harris, D. Bunandar, M. Pant, G. R. Steinbrecher, J. Mower, M. Prabhu, T. Baehr-Jones, M. Hochberg, and D. Englund, "Large-scale quantum photonic circuits in silicon", Nanophotonics **5**, 456–468 (2016) (cited on page 3).

7

[31] M. Lipson, "Guiding, modulating, and emitting light on silicon-challenges and opportunities", Journal of Lightwave Technology **23**, 4222–4238 (2005) (cited on page 3).

[32] K. K. Lee, "Transmission and routing of optical signals in on-chip waveguides for silicon microphotonics", PhD thesis (Massachusetts Institute of Technology, 2001) (cited on page 3).

[33] Y. A. Vlasov and S. J. McNab, "Losses in single-mode silicon-on-insulator strip waveguides and bends", Optics express **12**, 1622–1631 (2004) (cited on page 3).

[34] S. K. Selvaraja and P. Sethi, "Review on optical waveguides", Emerging Waveguide Technology **95**, 458 (2018) (cited on page 3).

[35] C. Kittel, *Introduction to solid state physics* (John Wiley & sons, inc, 2005) (cited on pages 3–4).

[36] A. Szameit, T. Pertsch, S. Nolte, A. Tünnermann, U. Peschel, and F. Lederer, "Optical bloch oscillations in general waveguide lattices", JOSA B **24**, 2632–2639 (2007) (cited on page 3).

[37] D. N. Christodoulides, F. Lederer, and Y. Silberberg, "Discretizing light behaviour in linear and nonlinear waveguide lattices", Nature **424**, 817–823 (2003) (cited on page 3).

[38] U. Peschel, T. Pertsch, and F. Lederer, "Optical bloch oscillations in waveguide arrays", Optics letters **23**, 1701–1703 (1998) (cited on page 3).

[39] R. Morandotti, U. Peschel, J. Aitchison, H. Eisenberg, and Y. Silberberg, "Experimental observation of linear and nonlinear optical bloch oscillations", Physical Review Letters **83**, 4756 (1999) (cited on page 3).

[40] S. Longhi, "Quantum-optical analogies using photonic structures", Laser & Photonics Reviews **3**, 243–261 (2009) (cited on page 3).

[41] T. Schwartz, G. Bartal, S. Fishman, and M. Segev, "Transport and anderson localization in disordered two-dimensional photonic lattices", Nature **446**, 52–55 (2007) (cited on pages 3, 66).

[42] D. S. Wiersma, "Disordered photonics", Nature Photonics **7**, 188–196 (2013) (cited on pages 3, 71).

[43] Y. Bromberg, Y. Lahini, R. Morandotti, and Y. Silberberg, "Quantum and classical correlations in waveguide lattices", Physical review letters **102**, 253904 (2009) (cited on page 3).

[44] J. D. Joannopoulos, P. R. Villeneuve, and S. Fan, "Photonic crystals: putting a new twist on light", Nature **386**, 143–149 (1997) (cited on page 3).

[45] E. Yablonovitch, "Inhibited spontaneous emission in solid-state physics and electronics", Physical review letters **58**, 2059 (1987) (cited on page 3).

[46] E. Yablonovitch, "Photonic band-gap structures", JOSA B **10**, 283–295 (1993) (cited on pages 3, 5).

[47] L. Thylén, M. Qiu, and S. Anand, "Photonic crystals—a step towards integrated circuits for photonics", ChemPhysChem **5**, 1268–1283 (2004) (cited on page 3).

[48] C. M. Soukoulis, "The history and a review of the modelling and fabrication of photonic crystals", Nanotechnology **13**, 420 (2002) (cited on page 3).

[49] U. Biswas, C. Nayak, and J. K. Rakshit, "Fabrication techniques and applications of two-dimensional photonic crystal: history and the present status", Optical Engineering **62**, 010901–010901 (2023) (cited on page 3).

[50] J. D. Jackson, *Classical electrodynamics* (American Association of Physics Teachers, 1999) (cited on page 3).

[51] F. Bloch, "Über die quantenmechanik der elektronen in kristallgittern", Zeitschrift für physik **52**, 555–600 (1929) (cited on page 4).

[52] P. S. J. Russell, "Optics of floquet-bloch waves in dielectric gratings", Applied Physics B **39**, 231–246 (1986) (cited on page 4).

[53] S. G. Johnson, S. Fan, P. R. Villeneuve, J. D. Joannopoulos, and L. Kolodziejski, "Guided modes in photonic crystal slabs", Physical Review B **60**, 5751 (1999) (cited on page 5).

[54] E. Chow, S. Lin, S. Johnson, P. Villeneuve, J. Joannopoulos, J. R. Wendt, G. A. Vawter, W. Zubrzycki, H. Hou, and A. Alleman, "Three-dimensional control of light in a two-dimensional photonic crystal slab", Nature **407**, 983–986 (2000) (cited on page 5).

[55] L. Novotny and B. Hecht, *Principles of nano-optics* (Cambridge university press, 2012) (cited on page 5).

[56] N. Parappurath, F. Alpeggiani, L. Kuipers, and E. Verhagen, "Direct observation of topological edge states in silicon photonic crystals: spin, dispersion, and chiral routing", Science advances **6**, eaaw4137 (2020) (cited on pages 5, 7).

[57] S. Van Enk and G. Nienhuis, "Spin and orbital angular momentum of photons", Europhysics Letters **25**, 497 (1994) (cited on page 5).

[58] E. Hecht, *Optics* (Pearson Education, Incorporated, 2017) (cited on page 6).

[59] K. Y. Bliokh, F. J. Rodríguez-Fortuño, F. Nori, and A. V. Zayats, "Spin-orbit interactions of light", Nature Photonics **9**, 796–808 (2015) (cited on pages 6, 24).

[60] K. Y. Bliokh and F. Nori, "Transverse and longitudinal angular momenta of light", Physics Reports **592**, 1–38 (2015) (cited on pages 6, 27).

[61] L. W. T. Kelvin, *Baltimore lectures on molecular dynamics and the wave theory of light* (CUP Archive, 1904) (cited on page 6).

[62] N. B. M. Schröter, S. Stolz, K. Manna, F. de Juan, M. G. Vergniory, J. A. Krieger, D. Pei, T. Schmitt, P. Dudin, T. K. Kim, C. Cacho, B. Bradlyn, H. Borrmann, M. Schmidt, R. Widmer, V. N. Strocov, and C. Felser, "Observation and control of maximal chern numbers in a chiral topological semimetal", Science **369**, 179–183 (2020) (cited on page 6).

[63] H. Price, Y. Chong, A. Khanikaev, H. Schomerus, L. J. Maczewsky, M. Kremer, M. Heinrich, A. Szameit, O. Zilberberg, Y. Yang, B. Zhang, A. Alù, R. Thomale, I. Carusotto, P. St-Jean, A. Amo, A. Dutt, L. Yuan, S. Fan, X. Yin, C. Peng, T. Ozawa, and A. Blanco-Redondo, "Roadmap on topological photonics", Journal of Physics: Photonics **4**, 032501 (2022) (cited on page 6).

[64] S. A. H. Gangaraj, M. G. Silveirinha, and G. W. Hanson, "Berry phase, berry connection, and chern number for a continuum bianisotropic material from a classical electromagnetics perspective", IEEE journal on multiscale and multiphysics computational techniques **2**, 3–17 (2017) (cited on page 7).

[65] M. Berrry, "Quantal phase factors accompanying adiabatic changes", Proc R Soc Lond A Math Phys Sci **392**, 45 (1984) (cited on page 7).

[66] A. Shapere and F. Wilczek, *Geometric phases in physics*, Vol. 5 (World scientific, 1989) (cited on page 7).

[67] R. Jackiw and C. Rebbi, "Solitons with fermion number", Physical Review D **13**, 3398–3409 (1976) (cited on pages 7, 9, 54–55).

[68] Y. Hatsugai, "Chern number and edge states in the integer quantum hall effect", Phys. Rev. Lett. **71**, 3697–3700 (1993) (cited on pages 7, 9, 54).

[69] Y. Hatsugai, "Edge states in the integer quantum hall effect and the riemann surface of the bloch function", Phys. Rev. B **48**, 11851–11862 (1993) (cited on pages 7, 54).

[70] R. S. Mong and V. Shivamoggi, "Edge states and the bulk-boundary correspondence in dirac hamiltonians", Physical Review B **83**, 125109 (2011) (cited on pages 7, 54).

[71] J. E. Avron, R. Seiler, and B. Simon, "Homotopy and quantization in condensed matter physics", Phys. Rev. Lett. **51**, 51–53 (1983) (cited on page 7).

[72] D. J. Thouless, M. Kohmoto, M. P. Nightingale, and M. den Nijs, "Quantized hall conductance in a two-dimensional periodic potential", Phys. Rev. Lett. **49**, 405–408 (1982) (cited on page 7).

[73] Z. Wang, Y. Chong, J. D. Joannopoulos, and M. Soljačić, "Observation of unidirectional backscattering-immune topological electromagnetic states", Nature **461**, 772–775 (2009) (cited on pages 7, 54, 65).

[74] S. A. H. Gangaraj and F. Monticone, "Topological waveguiding near an exceptional point: defect-immune, slow-light, and loss-immune propagation", Physical review letters **121**, 093901 (2018) (cited on page 7).

[75] L. Yu, H. Xue, and B. Zhang, "Topological slow light via coupling chiral edge modes with flatbands", Applied Physics Letters **118**, https://doi.org/10.1063/5.0039839 (2021) (cited on page 7).

[76] A. Forbes, M. de Oliveira, and M. R. Dennis, "Structured light", Nature Photonics **15**, 253–262 (2021) (cited on page 7).

[77] D. J. Richardson, "Filling the light pipe", Science **330**, 327–328 (2010) (cited on page 7).

[78] P. Jiang, N. Ma, X. Qiao, and H. Zhang, "Recent progress in chiral topological quantum interface", Frontiers in Physics **10**, 22 (2022) (cited on page 7).

[79] Z. Wang, Y. Chong, J. D. Joannopoulos, and M. Soljačić, "Reflection-free one-way edge modes in a gyromagnetic photonic crystal", Physical review letters **100**, 013905 (2008) (cited on pages 7, 25–26, 36, 54).

[80] T. Ma, A. B. Khanikaev, S. H. Mousavi, and G. Shvets, "Guiding electromagnetic waves around sharp corners: Topologically protected photonic transport in metawaveguides", Physical Review Letters **114**, 127401 (2015) (cited on pages 7, 41, 54).

[81] B. Bahari, A. Ndao, F. Vallini, A. El Amili, Y. Fainman, and B. Kanté, "Nonreciprocal lasing in topological cavities of arbitrary geometries", Science **358**, 636–640 (2017) (cited on page 7).

[82] X. Cheng, C. Jouvaud, X. Ni, S. H. Mousavi, A. Z. Genack, and A. B. Khanikaev, "Robust reconfigurable electromagnetic pathways within a photonic topological insulator", Nature Materials **15**, 542–548 (2016) (cited on pages 7, 9, 36, 66).

[83] A. B. Khanikaev, S. Hossein Mousavi, W.-K. Tse, M. Kargarian, A. H. MacDonald, and G. Shvets, "Photonic topological insulators", Nature materials **12**, 233–239 (2013) (cited on pages 7, 9, 36, 65).

[84] A. K. Geim and K. S. Novoselov, "The rise of graphene", Nature materials **6**, 183–191 (2007) (cited on page 7).

[85] G. Cocco, E. Cadelano, and L. Colombo, "Gap opening in graphene by shear strain", Physical Review B **81**, 241412 (2010) (cited on page 7).

[86] M. Y. Han, B. Özyilmaz, Y. Zhang, and P. Kim, "Energy band-gap engineering of graphene nanoribbons", Physical review letters **98**, 206805 (2007) (cited on page 7).

[87] T. Ohta, A. Bostwick, T. Seyller, K. Horn, and E. Rotenberg, "Controlling the electronic structure of bilayer graphene", Science **313**, 951–954 (2006) (cited on page 7).

[88] L. H. Wu and X. Hu, "Scheme for achieving a topological photonic crystal by using dielectric material", Physical Review Letters **114**, 223901 (2015) (cited on pages 8–9, 24–25, 36, 54, 65).

[89] S. Barik, H. Miyake, W. DeGottardi, E. Waks, and M. Hafezi, "Two-dimensionally confined topological edge states in photonic crystals", New Journal of Physics **18**, 113013 (2016) (cited on pages 8–9, 24–25).

[90] J. K. Asbóth, L. Oroszlány, and A. Pályi, *A Short Course on Topological Insulators*, Vol. 919, Lecture Notes in Physics (Springer International Publishing, Cham, 2016) (cited on pages 9, 24).

[91] M. Hafezi, E. A. Demler, M. D. Lukin, and J. M. Taylor, "Robust optical delay lines with topological protection", Nature Physics **7**, 907–912 (2011) (cited on pages 9, 24, 66).

[92] R. O. Umucal ılar and I. Carusotto, "Artificial gauge field for photons in coupled cavity arrays", Phys. Rev. A **84**, 043804 (2011) (cited on page 9).

[93] C. L. Kane and E. J. Mele, "Quantum spin hall effect in graphene", Physical review letters **95**, 226801 (2005) (cited on page 9).

[94] F. Zhang, J. Jung, G. A. Fiete, Q. Niu, and A. H. MacDonald, "Spontaneous quantum hall states in chirally stacked few-layer graphene systems", Phys. Rev. Lett. **106**, 156801 (2011) (cited on page 9).

[95] T. Ma and G. Shvets, "All-Si valley-hall photonic topological insulator", New Journal of Physics **18**, 025012 (2016) (cited on pages 9, 25, 36, 41, 54–55, 60, 65–66).

[96] N. Goldman, G. Jotzu, M. Messer, F. Görg, R. Desbuquois, and T. Esslinger, "Creating topological interfaces and detecting chiral edge modes in a two-dimensional optical lattice", Physical Review A **94**, 043611 (2016) (cited on page 9).

[97] M. I. Shalaev, W. Walasik, A. Tsukernik, Y. Xu, and N. M. Litchinitser, "Robust topologically protected transport in photonic crystals at telecommunication wavelengths", Nature Nanotechnology **14**, 31–34 (2019) (cited on pages 9, 13, 15, 25, 36, 54–56, 59, 65–66).

[98] Y. Yang, H. Jiang, and Z. H. Hang, "Topological valley transport in two-dimensional honeycomb photonic crystals", Scientific reports **8**, 1588 (2018) (cited on page 9).

[99] X.-L. Qi, Y.-S. Wu, and S.-C. Zhang, "General theorem relating the bulk topological number to edge states in two-dimensional insulators", Phys. Rev. B **74**, 045125 (2006) (cited on pages 9, 54).

[100] C. Sun, M. T. Wade, Y. Lee, J. S. Orcutt, L. Alloatti, M. S. Georgas, A. S. Waterman, J. M. Shainline, R. R. Avizienis, S. Lin, B. R. Moss, R. Kumar, F. Pavanello, A. H. Atabaki, H. M. Cook, A. J. Ou, J. C. Leu, Y.-H. Chen, K. Asanović, R. J. Ram, M. A. Popović, and V. M. Stojanović, "Single-chip microprocessor that communicates directly using light", Nature **528**, 534–538 (2015) (cited on page 13).

[101] P. Kok, W. J. Munro, K. Nemoto, T. C. Ralph, J. P. Dowling, and G. J. Milburn, "Linear optical quantum computing with photonic qubits", Reviews of modern physics **79**, 135 (2007) (cited on page 13).

[102] Y. Ji, J. Zhang, Y. Zhao, X. Yu, J. Zhang, and X. Chen, "Prospects and research issues in multi-dimensional all optical networks.", Sci. China Inf. Sci. **59**, 101301–1 (2016) (cited on page 13).

[103] H. J. Caulfield and S. Dolev, "Why future supercomputing requires optics", Nature Photonics **4**, 261–263 (2010) (cited on page 13).

[104] M. Burresi, R. J. P. Engelen, A. Opheij, D. Van Oosten, D. Mori, T. Baba, and L. Kuipers, "Observation of polarization singularities at the nanoscale", Physical Review Letters **102**, 033902 (2009) (cited on pages 13–14, 17, 38).

[105] L. De Angelis, "The singular optics of random light: a 2d vectorial investigation", English, PhD thesis (Delft University of Technology, Dec. 2018) (cited on page 13).

[106] N. Rotenberg and L. Kuipers, "Mapping nanoscale light fields", Nature Photonics **8**, 919–926 (2014) (cited on pages 13, 18, 24, 36, 55, 66–67).

[107] M. L. M. Balistreri, J. P. Korterik, L. Kuipers, and N. F. van Hulst, "Local Observations of Phase Singularities in Optical Fields in Waveguide Structures", Physical Review Letters **85**, 294–297 (2000) (cited on pages 13, 37).

[108] M. L. M. Balistreri, D. J. W. Klunder, F. C. Blom, A. Driessen, H. W. J. M. Hoekstra, J. P. Korterik, L. Kuipers, and N. F. van Hulst, "Visualizing the whispering gallery modes in a cylindrical optical microcavity", Optics Letters **24**, 1829 (1999) (cited on page 14).

[109] M. Sandtke, R. J. P. Engelen, H. Schoenmaker, I. Attema, H. Dekker, I. Cerjak, J. Korterik, F. Segerink, and L. Kuipers, "Novel instrument for surface plasmon polariton tracking in space and time", Review of scientific instruments **79**, 013704 (2008) (cited on page 14).

[110] K. Karrai and R. D. Grober, "Piezoelectric tip-sample distance control for near field optical microscopes", Applied Physics Letters **1842**, 1842 (1995) (cited on page 14).

[111] R. Engelen, D. Mori, T. Baba, and L. Kuipers, "Subwavelength structure of the evanescent field of an optical bloch wave", Physical Review Letters **102**, 2–5 (2009) (cited on page 14).

[112] N. Rotenberg, B. le Feber, T. D. Visser, and L. Kuipers, "Tracking nanoscale electric and magnetic singularities through three-dimensional space", Optica **2**, 540 (2015) (cited on page 14).

[113] J. Sun, P. S. Carney, and J. C. Schotland, "Strong tip effects in near-field scanning optical tomography", Journal of Applied Physics **102**, 103103 (2007) (cited on page 14).

[114] A. V. Oppenheim, *Discrete-time signal processing* (Pearson Education India, 1999) (cited on page 17).

[115] B. le Feber, N. Rotenberg, D. M. Beggs, and L. Kuipers, "Simultaneous measurement of nanoscale electric and magnetic optical fields", Nature Photonics **8**, 43–46 (2014) (cited on pages 17–18).

[116] E. Devaux, A. Dereux, E. Bourillot, J.-C. Weeber, Y. Lacroute, J.-P. Goudonnet, and C. Girard, "Local detection of the optical magnetic field in the near zone of dielectric samples", Physical Review B **62**, 10504 (2000) (cited on page 18).

[117] R. L. Olmon, M. Rang, P. M. Krenz, B. A. Lail, L. V. Saraf, G. D. Boreman, and M. B. Raschke, "Determination of electric-field, magnetic-field, and electric-current distributions of infrared optical antennas: a near-field optical vector network analyzer", Physical review letters **105**, 167403 (2010) (cited on page 18).

[118] I. V. Kabakova, A. De Hoogh, R. E. Van Der Wel, M. Wulf, B. Le Feber, and L. Kuipers, "Imaging of electric and magnetic fields near plasmonic nanowires", Scientific Reports **6**, 22665 (2016) (cited on page 18).

[119] G. Valaskovic, M. Holton, and G. Morrison, "Parameter control, characterization, and optimization in the fabrication of optical fiber near-field probes", Applied optics **34**, 1215–1228 (1995) (cited on page 18).

[120] K. N. D. Pauline Stevic, "BOE / HF – Silicon dioxide Etching Standard Operating Procedure", https://d2k0ddhflgrk1i.cloudfront.net/TNW/Afdelingen/Quantum%20Nanoscience/Kavli%20Nanolab%20Delft/Equipment/BOE-HF%20SOP%20Silicon%20Etching.pdf (2018) (cited on page 18).

[121] J. A. Veerman, A. M. Otter, L. Kuipers, and N. F. Van Hulst, "High definition aperture probes for near-field optical microscopy fabricated by focused ion beam milling", Applied Physics Letters **72**, 3115–3117 (1998) (cited on page 18).

[122] C. Multiphysics, "Introduction to comsol multiphysics®", COMSOL Multiphysics, Burlington, MA, accessed Feb **9**, 32 (1998) (cited on pages 19, 56–57, 59).

[123] S. G. Johnson and J. D. Joannopoulos, "Block-iterative frequency-domain methods for maxwell's equations in a planewave basis", Optics express **8**, 173–190 (2001) (cited on page 19).

[124] S. Arora, T. Bauer, N. Parappurath, R. Barczyk, E. Verhagen, and L. Kuipers, "Breakdown of spin-to-helicity locking at the nanoscale in topological photonic crystal edge states", Physical Review Letters **128**, 203903 (2022) (cited on pages 23, 54).

[125] R. J. Coles, D. M. Price, J. E. Dixon, B. Royall, E. Clarke, P. Kok, M. S. Skolnick, A. M. Fox, and M. N. Makhonin, "Chirality of nanophotonic waveguide with embedded quantum emitter for unidirectional spin transfer", Nature Communications **7**, 1–7 (2016) (cited on page 24).

[126] I. Söllner, S. Mahmoodian, S. L. Hansen, L. Midolo, A. Javadi, G. Kiršanske, T. Pregnolato, H. El-Ella, E. H. Lee, J. D. Song, S. Stobbe, and P. Lodahl, "Deterministic photon-emitter coupling in chiral photonic circuits", Nature Nanotechnology **10**, 775–778 (2015) (cited on page 24).

[127] A. B. Young, A. C. T. Thijssen, D. M. Beggs, P. Androvitsaneas, L. Kuipers, J. G. Rarity, S. Hughes, and R. Oulton, "Polarization Engineering in Photonic Crystal Waveguides for Spin-Photon Entanglers", Physical Review Letters **115**, 153901 (2015) (cited on page 24).

[128] T. Van Mechelen and Z. Jacob, "Universal spin-momentum locking of evanescent waves", Optica **3**, 118 (2016) (cited on page 24).

[129] J. Borregaard, A. S. Sørensen, and P. Lodahl, "Quantum Networks with Deterministic Spin–Photon Interfaces", Advanced Quantum Technologies **2**, 1800091 (2019) (cited on page 24).

[130] H. Pichler and P. Zoller, "Photonic Circuits with Time Delays and Quantum Feedback", Physical Review Letters **116**, 1–6 (2016) (cited on page 24).

[131] B. Orazbayev and R. Fleury, "Quantitative robustness analysis of topological edge modes in C6 and valley-Hall metamaterial waveguides", Nanophotonics **8**, 1433–1441 (2019) (cited on pages 24, 65, 71–72, 74).

[132] M. Proctor, R. V. Craster, S. A. Maier, V. Giannini, and P. A. Huidobro, "Exciting Pseudospin-Dependent Edge States in Plasmonic Metasurfaces", ACS Photonics **6**, 2985–2995 (2019) (cited on page 24).

[133] M. Jalali Mehrabad, A. P. Foster, R. Dost, E. Clarke, P. K. Patil, A. M. Fox, M. S. Skolnick, and L. R. Wilson, "Chiral topological photonics with an embedded quantum emitter", Optica **7**, 1690 (2020) (cited on pages 24, 54, 65).

[134] L. Sapienza, M. Davanço, A. Badolato, and K. Srinivasan, "Nanoscale optical positioning of single quantum dots for bright and pure single-photon emission", Nature communications **6**, 7833 (2015) (cited on page 24).

[135] W.-M. Deng, X.-D. Chen, F.-L. Zhao, and J.-W. Dong, "Transverse angular momentum in topological photonic crystals", Journal of Optics **20**, 014006 (2018) (cited on page 24).

[136] H. Wang, S. K. Gupta, B. Xie, and M. Lu, "Topological photonic crystals: a review", Frontiers of Optoelectronics **13**, 50–72 (2020) (cited on page 24).

[137] Y. Mazor and A. Alù, "Routing Optical Spin and Pseudospin with Metasurfaces", Physical Review Applied **14**, 1 (2020) (cited on page 24).

[138] J. Petersen, J. Volz, and A. Rauschenbeutel, "Chiral nanophotonic waveguide interface based on spin-orbit interaction of light", Science **346**, 67–71 (2014) (cited on page 24).

[139] M. Proctor, X. Xiao, R. Craster, S. Maier, V. Giannini, and P. Arroyo Huidobro, "Near- and Far-Field Excitation of Topological Plasmonic Metasurfaces", Photonics **7**, 81 (2020) (cited on page 24).

[140] S. S. Oh, B. Lang, D. M. Beggs, D. L. Huffaker, M. Saba, and O. Hess, "Chiral Light-matter Interaction in Dielectric Photonic Topological Insulators", in Cleo pacific rim conference 2018 (2018), Th4H.5 (cited on page 24).

[141] D. G. Baranov, R. S. Savelev, S. V. Li, A. E. Krasnok, and A. Alù, "Modifying magnetic dipole spontaneous emission with nanophotonic structures", Laser & Photonics Reviews **11**, 1600268 (2017) (cited on page 24).

[142] S. Barik, A. Karasahin, C. Flower, T. Cai, H. Miyake, W. DeGottardi, M. Hafezi, and E. Waks, "A topological quantum optics interface", Science **359**, 666–668 (2018) (cited on pages 24–25, 36, 65).

[143] T. Pregnolato, X.-L. Chu, T. Schröder, R. Schott, A. D. Wieck, A. Ludwig, P. Lodahl, and N. Rotenberg, "Deterministic positioning of nanophotonic waveguides around single self-assembled quantum dots", APL Photonics **5**, 086101 (2020) (cited on page 24).

[144] R. E. Christiansen, F. Wang, O. Sigmund, and S. Stobbe, "Designing photonic topological insulators with quantum-spin-Hall edge states using topology optimization", Nanophotonics **8**, 1363–1369 (2019) (cited on page 24).

[145] H. Pichler, T. Ramos, A. J. Daley, and P. Zoller, "Quantum optics of chiral spin networks", Physical Review A **91**, 042116 (2015) (cited on page 24).

[146] S. Mahmoodian, P. Lodahl, and A. S. Sørensen, "Quantum Networks with Chiral-Light–Matter Interaction in Waveguides", Physical Review Letters **117**, 240501 (2016) (cited on page 24).

[147] P. St-Jean, V. Goblot, E. Galopin, A. Lemaître, T. Ozawa, L. Le Gratiet, I. Sagnes, J. Bloch, and A. Amo, "Lasing in topological edge states of a one-dimensional lattice", Nature Photonics **11**, 651–656 (2017) (cited on page 24).

[148] M. S. Rider, S. J. Palmer, S. R. Pocock, X. Xiao, P. Arroyo Huidobro, and V. Giannini, "A perspective on topological nanophotonics: current status and future challenges", Journal of Applied Physics **125**, 120901 (2019) (cited on page 24).

[149] N. Parappurath, F. Alpeggiani, L. Kuipers, and E. Verhagen, "Direct observation of topological edge states in silicon photonic crystals: Spin, dispersion, and chiral routing", Science Advances **6**, eaaw4137 (2020) (cited on pages 24–26, 28–29, 31, 36, 54, 65).

[150] S. Arora, T. Bauer, R. Barczyk, E. Verhagen, and L. Kuipers, "Direct quantification of topological protection in symmetry-protected photonic edge states at telecom wavelengths", Light: Science & Applications **10**, 9 (2021) (cited on pages 25, 35, 54–56, 59, 65, 67–69).

[151] X. T. He, E. T. Liang, J. J. Yuan, H. Y. Qiu, X. D. Chen, F. L. Zhao, and J. W. Dong, "A silicon-on-insulator slab for topological valley transport", Nature Communications **10**, 1–9 (2019) (cited on pages 25, 36, 41, 56, 65).

[152] J. W. Dong, X. D. Chen, H. Zhu, Y. Wang, and X. Zhang, "Valley photonic crystals for control of spin and topology", Nature Materials **16**, 298–302 (2017) (cited on pages 25, 54).

[153] M. A. Gorlach, X. Ni, D. A. Smirnova, D. Korobkin, D. Zhirihin, A. P. Slobozhanyuk, P. A. Belov, A. Alù, and A. B. Khanikaev, "Far-field probing of leaky topological states in all-dielectric metasurfaces", Nature communications **9**, 909 (2018) (cited on page 25).

[154] Y. Yang, Y. F. Xu, T. Xu, H. X. Wang, J. H. Jiang, X. Hu, and Z. H. Hang, "Visualization of a Unidirectional Electromagnetic Waveguide Using Topological Photonic Crystals Made of Dielectric Materials", Physical Review Letters **120**, 217401 (2018) (cited on pages 25–26).

[155] P. Kaspar, R. Kappeler, D. Erni, and H. Jäckel, "Relevance of the light line in planar photonic crystal waveguides with weak vertical confinement", Optics Express **19**, 24344 (2011) (cited on page 26).

[156] K. Busch, S. Lölkes, R. B. Wehrspohn, and H. Föll, *Photonic crystals: advances in design, fabrication and characterization* (John Wiley & Sons, 2006) (cited on page 26).

[157] P. S. J. Russell, "Optics of Floquet-Bloch waves in dielectric gratings", Applied Physics B Photophysics and Laser Chemistry **39**, 231–246 (1986) (cited on page 27).

[158] H. Gersen, T. J. Karle, R. J. P. Engelen, W. Bogaerts, J. P. Korterik, N. F. van Hulst, T. F. Krauss, and L. Kuipers, "Direct Observation of Bloch Harmonics and Negative Phase Velocity in Photonic Crystal Waveguides", Physical Review Letters **94**, 123901 (2005) (cited on pages 27, 30, 36, 66).

[159] A. Aiello, P. Banzer, M. Neugebauer, and G. Leuchs, "From transverse angular momentum to photonic wheels", Nature Photonics **9**, 789–795 (2015) (cited on pages 27–28).

[160] K. Y. Bliokh, D. Smirnova, and F. Nori, "Quantum spin Hall effect of light", Science **348**, 1448–1451 (2015) (cited on page 27).

[161] A. Y. Bekshaev, K. Y. Bliokh, and F. Nori, "Transverse spin and momentum in two-wave interference", Physical Review X **5**, 1–9 (2015) (cited on page 27).

[162] L. Xu, H.-X. Wang, Y.-D. Xu, H.-Y. Chen, and J.-H. Jiang, "Accidental degeneracy in photonic bands and topological phase transitions in two-dimensional core-shell dielectric photonic crystals", Optics Express **24**, 18059 (2016) (cited on page 29).

[163] H. Gersen, L. Novotny, L. Kuipers, and N. F. Van Hulst, "On the concept of imaging nanoscale vector fields", Nature Photonics **1**, 242 (2007) (cited on page 31).

[164] F. Haldane and S. Raghu, "Possible realization of directional optical waveguides in photonic crystals with broken time-reversal symmetry", Physical review letters **100**, 013904 (2008) (cited on pages 36, 54, 65).

[165] S. Raghu and F. D. Haldane, "Analogs of quantum-Hall-effect edge states in photonic crystals", Physical Review A **78**, 033834 (2008) (cited on pages 36, 54, 56, 65).

[166] Y. Plotnik, M. C. Rechtsman, D. Song, M. Heinrich, J. M. Zeuner, S. Nolte, Y. Lumer, N. Malkova, J. Xu, A. Szameit, Z. Chen, and M. Segev, "Observation of unconventional edge states in 'photonic graphene'", Nature Materials **13**, 57–62 (2014) (cited on page 36).

[167] M. Z. Hasan, "Colloquium : Topological insulators", Review of Modern Physics **82**, 3045 (2010) (cited on page 36).

[168] S. Klembt, T. H. Harder, O. A. Egorov, K. Winkler, R. Ge, M. A. Bandres, M. Emmerling, L. Worschech, T. C. Liew, M. Segev, C. Schneider, and S. Höfling, "Exciton-polariton topological insulator", Nature **562**, 552–556 (2018) (cited on page 36).

[169] I. Carusotto and C. Ciuti, "Quantum fluids of light", Reviews of Modern Physics **85**, 299–366 (2013) (cited on page 36).

[170] D. Smirnova, S. Kruk, D. Leykam, E. Melik-Gaykazyan, D. Y. Choi, and Y. Kivshar, "Third-Harmonic Generation in Photonic Topological Metasurfaces", Physical Review Letters **123**, 103901 (2019) (cited on page 36).

[171] M.-H. Lu, Z. D. Wang, H.-F. Wang, B.-Y. Xie, X.-Y. Zhu, and Y.-F. Chen, "Photonics meets topology", Optics Express **26**, 24531 (2018) (cited on page 36).

[172] Y. Kim, K. Choi, J. Ihm, and H. Jin, "Topological domain walls and quantum valley Hall effects in silicene", Physical Review B **89**, 085429 (2014) (cited on pages 36, 66).

[173] A. M. Dubrovkin, U. Chattopadhyay, B. Qiang, O. Buchnev, Q. J. Wang, Y. Chong, and N. I. Zheludev, " Near-field mapping of the edge mode of a topological valley slab waveguide at $\lambda = 1.55\ \mu$m ", Applied Physics Letters **116**, 191105 (2020) (cited on pages 36, 66).

7

[174] J. R. Schaibley, H. Yu, G. Clark, P. Rivera, J. S. Ross, K. L. Seyler, W. Yao, and X. Xu, "Valleytronics in 2D materials", Nature Reviews Materials **1**, 1–15 (2016) (cited on page 36).

[175] D. Xiao, W. Yao, and Q. Niu, "Valley-contrasting physics in graphene: Magnetic moment and topological transport", Physical Review Letters **99**, 236809 (2007) (cited on pages 36, 66).

[176] J. Zak, "Berrys phase for energy bands in solids", Physical Review Letters **62**, 2747–2750 (1989) (cited on page 36).

[177] R. J. P. Engelen, Y. Sugimoto, H. Gersen, N. Ikeda, K. Asakawa, and L. Kuipers, "Ultrafast evolution of photonic eigenstates in k-space", Nature Physics **3**, 401–405 (2007) (cited on page 38).

[178] T. F. Krauss, L. O'Faolain, S. Schulz, D. M. Beggs, F. Morichetti, A. Canciamilla, M. Torregiani, A. Melloni, S. Mazoyer, P. Lalanne, A. Samarelli, M. Sorel, and R. De La Rue, "Understanding the rich physics of light propagation in slow photonic crystal waveguides", Advances in Slow and Fast Light III **7612**, 76120L (2010) (cited on page 41).

[179] W. Kuang and J. D. O'Brien, "Reducing the out-of-plane radiation loss of photonic crystal waveguides on high-index substrates", OSA Trends in Optics and Photonics Series **96 A**, 1497–1498 (2004) (cited on page 42).

[180] E. Chow, S. Y. Lin, J. R. Wendt, S. G. Johnson, and J. D. Joannopoulos, "Quantitative analysis of bending efficiency in photonic-crystal waveguide bends at $\lambda = 1.55\ \mu$m wavelengths", Optics Letters **26**, 286 (2001) (cited on page 42).

[181] A. Chutinan, M. Okano, and S. Noda, "Wider bandwidth with high transmission through waveguide bends in two-dimensional photonic crystal slabs", Applied Physics Letters **80**, 1698–1700 (2002) (cited on page 42).

[182] R. J. P. Engelen, D. Mori, T. Baba, and L. Kuipers, "Two Regimes of Slow-Light Losses Revealed by Adiabatic Reduction of Group Velocity", Physical Review Letters **101**, 103901 (2008) (cited on pages 46, 52, 74).

[183] S. Mazoyer, P. Lalanne, J. Rodier, J. Hugonin, M. Spasenović, L. Kuipers, D. Beggs, and T. Krauss, "Statistical fluctuations of transmission in slow light photonic-crystal waveguides", Optics Express **18**, 14654 (2010) (cited on page 49).

[184] S. Johnson and J. Joannopoulos, "Block-iterative frequency-domain methods for Maxwell's equations in a planewave basis", Optics Express **8**, 173 (2001) (cited on page 50).

[185] A. Singh, G. Ctistis, S. R. Huisman, J. P. Korterik, A. P. Mosk, J. L. Herek, and P. W. H. Pinkse, "Observation of nonlinear bands in near-field scanning optical microscopy of a photonic-crystal waveguide", Journal of Applied Physics **117**, 033104 (2015) (cited on page 52).

[186] D. Yu, S. Arora, and L. Kuipers, "Impact of transforming interface geometry on edge states in valley photonic crystals", preprint arXiv.2310.00858 (2023) (cited on pages 53, 107).

[187] M. C. Rechtsman, J. M. Zeuner, Y. Plotnik, Y. Lumer, D. Podolsky, F. Dreisow, S. Nolte, M. Segev, and A. Szameit, "Photonic Floquet topological insulators", Nature **496**, 196–200 (2013) (cited on page 54).

[188] X. Xi, K.-P. Ye, and R.-X. Wu, "Topological photonic crystal of large valley chern numbers", Photonics Research **8**, B1–B7 (2020) (cited on page 54).

[189] R. J. Davis, Y. Zhou, J. B. Dia'aaldin, P. R. Bandaru, and D. F. Sievenpiper, "Topologically protected edge states in triangular lattices", Physical Review B **106**, 165403 (2022) (cited on page 54).

[190] X.-L. Qi, Y.-S. Wu, and S.-C. Zhang, "General theorem relating the bulk topological number to edge states in two-dimensional insulators", Phys. Rev. B **74**, 045125 (2006) (cited on page 54).

[191] N. Parappurath, "Chiral flow of light in photonic crystals with broken symmetries", PhD Thesis (Technische Universiteit Eindhoven, 2019) (cited on page 54).

[192] J. Noh, S. Huang, K. P. Chen, and M. C. Rechtsman, "Observation of photonic topological valley hall edge states", Physical Review Letters **120**, 63902 (2018) (cited on page 54).

[193] S. Wong, M. Saba, O. Hess, and S. S. Oh, "Gapless unidirectional photonic transport using all-dielectric kagome lattices", Physical Review Research **2**, 012011 (2020) (cited on page 54).

[194] H. Xue, Y. Yang, and B. Zhang, "Topological valley photonics: physics and device applications", Advanced Photonics Research **2**, 2100013 (2021) (cited on page 54).

[195] H. Yoshimi, T. Yamaguchi, Y. Ota, Y. Arakawa, and S. Iwamoto, "Slow light waveguides in topological valley photonic crystals", Optics Letters **45**, 2648 (2020) (cited on pages 54, 56, 65–66, 79).

[196] K. M. Devi, S. Jana, and D. R. Chowdhury, "Topological edge states in an all-dielectric terahertz photonic crystal", Optical Materials Express **11**, 2445–2458 (2021) (cited on page 54).

[197] B. L. Li, H. Y. Shi, W. E. Sha, J. J. Yi, G. Q. Li, A. X. Zhang, and Z. Xu, "Valley topological line-defects for terahertz waveguides and power divider", Optical Materials **126**, 10.1016/j.optmat.2022.112152 (2022) (cited on page 54).

[198] Y. J. Tan, W. Wang, A. Kumar, and R. Singh, "Interfacial topological photonics: broadband silicon waveguides for thz 6g communication and beyond", Optics Express **30**, 33035–33047 (2022) (cited on page 54).

[199] E. Wen, J. B. Dia'aaldin, R. J. Davis, X. Yang, and D. F. Sievenpiper, "Designing topological defect lines protected by gauge-dependent symmetry indicators", Physical Review Applied **17**, 064008 (2022) (cited on page 54).

[200] B. A. Bernevig, T. L. Hughes, and S.-C. Zhang, "Quantum spin hall effect and topological phase transition in HgTe quantum wells", science **314**, 1757–1761 (2006) (cited on page 54).

[201] C. Rosiek, G. Arregui Bravo, A. Vladimirova, M. Albrechtsen, B. Lahijani, R. Christiansen, and S. Stobbe, "Observation of strong backscattering in valley-hall photonic topological interface modes", Nature Photonics **17**, 1–7 (2023) (cited on pages 54, 65, 69, 79).

[202] T. F. Krauss, "Slow light in photonic crystal waveguides", Journal of Physics D: Applied Physics **40**, 2666 (2007) (cited on pages 56, 65, 74).

[203] A. A. Sukhorukov, S. Ha, A. S. Desyatnikov, A. V. Lavrinenko, and Y. S. Kivshar, "Slow-light vortices in periodic waveguides", Journal of Optics A: Pure and Applied Optics **11**, 094016 (2009) (cited on page 56).

[204] A. Mock, L. Lu, and J. O'Brien, "Space group theory and fourier space analysis of two-dimensional photonic crystal waveguides", Phys. Rev. B **81**, 155115 (2010) (cited on pages 60, 66).

[205] S. Arora, T. Bauer, R. Barczyk, E. Verhagen, and L. Kuipers, "Multiple backscattering in trivial and non-trivial topological photonic crystal edge states with controlled disorder", preprint arXiv.2310.02978 (2023) (cited on pages 63, 107).

[206] T. Baba, "Slow light in photonic crystals", Nature photonics **2**, 465–473 (2008) (cited on page 65).

[207] M. Notomi, K. Yamada, A. Shinya, J. Takahashi, C. Takahashi, and I. Yokohama, "Extremely large group-velocity dispersion of line-defect waveguides in photonic crystal slabs", Physical review letters **87**, 253902 (2001) (cited on page 65).

[208] C. Smith, H. Benisty, S. Olivier, M. Rattier, C. Weisbuch, T. F. Krauss, R. De La Rue, R. Houdré, and U. Oesterle, "Low-loss channel waveguides with two-dimensional photonic crystal boundaries", Applied Physics Letters **77**, 2813–2815 (2000) (cited on page 65).

[209] S. Hughes, L. Ramunno, J. F. Young, and J. Sipe, "Extrinsic optical scattering loss in photonic crystal waveguides: role of fabrication disorder and photon group velocity", Physical review letters **94**, 033903 (2005) (cited on pages 65, 74).

[210] J. Topolancik, B. Ilic, and F. Vollmer, "Experimental observation of strong photon localization in disordered photonic crystal waveguides", Phys. Rev. Lett. **99**, 253901 (2007) (cited on page 65).

[211] L. Sapienza, H. Thyrrestrup, S. Stobbe, P. D. García, S. Smolka, and P. Lodahl, "Cavity quantum electrodynamics with anderson-localized modes", Science **327**, 1352–1355 (2010) (cited on page 65).

[212] M. Hafezi, S. Mittal, J. Fan, A. Migdall, and J. M. Taylor, "Imaging topological edge states in silicon photonics", Nature Photonics **7**, 1001–1005 (2013) (cited on page 65).

[213] Y. Yang, Y. Poo, R.-x. Wu, Y. Gu, and P. Chen, "Experimental demonstration of one-way slow wave in waveguide involving gyromagnetic photonic crystals", Applied Physics Letters **102**, https://doi.org/10.1063/1.4809956 (2013) (cited on page 65).

[214] J. Lu, C. Qiu, L. Ye, X. Fan, M. Ke, F. Zhang, and Z. Liu, "Observation of topological valley transport of sound in sonic crystals", Nature Physics **13**, 369–374 (2017) (cited on page 65).

[215] Y. Poo, R. Wu, Z. Lin, Y. Yang, and C. T. Chan, "Experimental realization of self-guiding unidirectional electromagnetic edge states", Physical Review Letters **106**, 093903 (2011) (cited on page 65).

[216] M. Minkov and S. Fan, "Unidirectional light transport in dynamically modulated waveguides", Physical Review Applied **10**, 044028 (2018) (cited on page 65).

[217] G.-J. Tang, X.-T. He, F.-L. Shi, J.-W. Liu, X.-D. Chen, and J.-W. Dong, "Topological photonic crystals: physics, designs, and applications", Laser & Photonics Reviews **16**, 2100300 (2022) (cited on page 65).

[218] G. Arregui, J. Gomis-Bresco, C. M. Sotomayor-Torres, and P. D. García, "Quantifying the robustness of topological slow light", Physical Review Letters **126**, 027403 (2021) (cited on pages 65, 72).

[219] L. O' Faolain, T. P. White, D. O' Brien, X. Yuan, M. D. Settle, and T. F. Krauss, "Dependence of extrinsic loss on group velocity in photonic crystal waveguides", Optics express **15**, 13129–13138 (2007) (cited on page 65).

[220] L. C. Andreani and D. Gerace, "Light–matter interaction in photonic crystal slabs", Physica status solidi (b) **244**, 3528–3539 (2007) (cited on page 65).

[221] H. Yoshimi, T. Yamaguchi, R. Katsumi, Y. Ota, Y. Arakawa, and S. Iwamoto, "Experimental demonstration of topological slow light waveguides in valley photonic crystals", Optics Express **29**, 13441 (2021) (cited on pages 65–66, 79).

[222] P. W. Anderson, "Absence of diffusion in certain random lattices", Phys. Rev. **109**, 1492–1505 (1958) (cited on page 66).

[223] Z. Shi, M. Davy, and A. Z. Genack, "Statistics and control of waves in disordered media", Optics Express **23**, 12293–12320 (2015) (cited on page 66).

[224] J. Zak, "Berry's phase for energy bands in solids", Physical review letters **62**, 2747 (1989) (cited on page 66).

[225] B.-Y. Xie, H.-F. Wang, X.-Y. Zhu, M.-H. Lu, Z. Wang, and Y.-F. Chen, "Photonics meets topology", Optics Express **26**, 24531–24550 (2018) (cited on page 66).

[226] N. Le Thomas, H. Zhang, J. Jágerská, V. Zabelin, R. Houdré, I. Sagnes, and A. Talneau, "Light transport regimes in slow light photonic crystal waveguides", Physical Review B **80**, 125332 (2009) (cited on pages 67, 74).

[227] D. Melati, A. Melloni, and F. Morichetti, "Real photonic waveguides: guiding light through imperfections", Advances in Optics and Photonics **6**, 156–224 (2014) (cited on page 68).

[228] J. Topolancik, F. Vollmer, and B. Ilic, "Random high-q cavities in disordered photonic crystal waveguides", Applied Physics Letters **91**, 201102 (2007) (cited on page 68).

7

[229] S. Smolka, H. Thyrrestrup, L. Sapienza, T. B. Lehmann, K. R. Rix, L. S. Froufe-Pérez, P. D. García, and P. Lodahl, "Probing the statistical properties of anderson localization with quantum emitters", New Journal of Physics **13**, 063044 (2011) (cited on page 69).

[230] M. Spasenović, D. M. Beggs, P. Lalanne, T. F. Krauss, and L. Kuipers, "Measuring the spatial extent of individual localized photonic states", Physical Review B **86**, 155153 (2012) (cited on page 69).

[231] A. F. Koenderink, A. Lagendijk, and W. L. Vos, "Optical extinction due to intrinsic structural variations of photonic crystals", Phys. Rev. B **72**, 153102 (2005) (cited on page 71).

[232] M. Arcari, I. Söllner, A. Javadi, S. L. Hansen, S. Mahmoodian, J. Liu, H. Thyrrestrup, E. H. Lee, J. D. Song, S. Stobbe, and P. Lodahl, "Near-unity coupling efficiency of a quantum emitter to a photonic crystal waveguide", Physical review letters **113**, 093603 (2014) (cited on page 71).

[233] P. García, S. Smolka, S. Stobbe, and P. Lodahl, "Density of states controls anderson localization in disordered photonic crystal waveguides", Physical Review B **82**, 165103 (2010) (cited on pages 71, 74).

[234] S. Skipetrov and J. H. Page, "Red light for anderson localization", New Journal of Physics **18**, 021001 (2016) (cited on page 71).

[235] Beer, "Bestimmung der absorption des rothen lichts in farbigen flüssigkeiten", Annalen der Physik **162**, 78–88 (1852) (cited on page 72).

[236] L. O Faolain, S. A. Schulz, D. M. Beggs, T. P. White, L. Spasenovic Kuipers, F. Morichetti, A. Melloni, S. Mazoyer, J. P. Hugonin, P. Lalanne, and T. F. Krauss, "Loss engineered slow light waveguides", Optics express **18**, 27627–27638 (2010) (cited on page 74).

CURRICULUM VITÆ

Sonakshi ARORA

27-05-1993	Born in Kolkata, India.

EDUCATION

2011	La Martiniere For Girls Kolkata, India
2014	**Bachelors in Physics (Honours)** Ramjas College, Delhi University, India
2015	**Masters in Physics & Electronics** Punjab University, India
2018	**Masters in Physics** Freie Universität Berlin, Germany
Thesis:	Probing engineered excitons at the interface of transition metal dichalcogenides
Promotor:	Prof. dr. K. I. Bolotin
2023	**Ph.D. Physics** Technische Universiteit Delft, The Netherlands
Thesis:	Photonic topological edge states: A nanoscale investigation
Promotor:	Prof. dr. L. Kuipers

AWARDS

2023	Best Poster Award Pecs-XIII in Tokyo, Japan

LIST OF PUBLICATIONS

7. **S. Arora**, T. Bauer, R. Barczyk, E. Verhagen, L. Kuipers, *Multiple backscattering in trivial and non-trivial topological edge states with controlled disorder, in preparation* [205].

6. D. Yu*, **S. Arora***, L. Kuipers, *Impact of transforming interface geometry on edge states in valley photonic crystals, in submission* [186].

5. R. Barczyk, N. Parappurath, **S. Arora**, T. Bauer, L. Kuipers, and E. Verhagen, *Interplay of leakage radiation and protection in topological photonic crystal cavities*, Laser & Photonics Reviews **16** (9), 2200071 (2022).

4. **S. Arora**, T. Bauer, N. Parappurath, R. Barczyk, E. Verhagen, L. Kuipers, *Breakdown of spin-to-helicity locking at the nanoscale in topological photonic crystal edge states*, Physical Review Letters **128** (2022).

3. **S. Arora***, T. Bauer*, R. Barczyk*, E. Verhagen, L. Kuipers, *Direct quantification of topological protection in symmetry-protected photonic edge states at telecom wavelengths*, Light: Science & Applications **10**, 9 (2021).

2. K. Greben, **S. Arora**, M. G. Harats, K. I. Bolotin *Intrinsic and extrinsic defect-related excitons in TMDCs*, Nano Letters **20** , 2544-2550 (2020).

1. J. P Bonacum, A. O'Hara, D. Bao, O. S. Ovchinnikov, Y. Zhang, G. Gordeev, **S. Arora**, S. Reich, J. Idrobo, R. F. Haglund, S. T. Pantelides, K. I. Bolotin. *Atomic-resolution visualization and doping effects of complex structures in intercalated bilayer graphene*, Physical Review Materials **3**, 064004 (2019).

*These authors contributed equally to this work

QUOTES BIBLIOGRAPHY

1. Isaac Newton & Robert Hooke, *Isaac Newton letter to Robert Hooke* (1675)
2. Christopher and Jonathan Nolan, *The Prestige*, (Burbank, California, Touchstone Home Entertainment (2007))
3. J.K. Rowling, *Harry Potter and the Order of the Phoenix*(London: Bloomsbury 16 (2003))
4. Dr. Margaret Mead, cultural anthropologist and writer (New York, 1901-1978)
5. Amanda Gorman *The Hill We Climb* (Viking Press, Penguin Random House, New York, 2021)
6. Charlie Chaplin, My Autobiography (New York, Simon and Schuster, (1964))
7. Louisa M. Alcott, Little Women (Roberts Brothers, Boston, (1868))
8. Jane Austen, Northanger Abbey (London: Little, (2007))

ACKNOWLEDGEMENTS

"There is nothing I would not do for those who are really my friends. I have no notion of loving people by halves."

[8]Jane Austen

This section is my favorite part of the thesis and the only one that truly defines the prominence of these last years.

Call it being in the right place at the right time; I stumbled upon the opportunity to meet **Kobus** during a Casimir Open Day event, and a 15-minute conversation was all it took for me to know that I wanted to be a part of this journey. Thank you for not only welcoming me into the group but also for the invaluable life lessons you've imparted. Your unwavering belief in people and your constant effort to make them realize their potential have left an indelible mark. From Fourier analysis to choosing the right kind of Belegen (oud!), our one-on-one meetings and your teaching moments have been enriching experiences. I admire your deep understanding and eloquence, not only in the intricacies of physics but also in the complexities of human emotions. I appreciate that we shared a mutual understanding and a safe space where we could openly discuss innumerable challenges and experiences in our lives. **Ewold**, your wisdom and rigorous approach to scientific problems have been a constant source of inspiration. I am grateful for our weekly meetings that have molded me into a better scientist, teaching me never to stop asking questions. **Andrea**, thank you for being my promotor and I am grateful for our scientific discussions during the yearly review meetings.

Rene, our journey began around the same time, and now, we're concluding it together. Your relentless commitment to fabricating beautiful samples reflects your incredible skills as a physicist. Best of luck with your defense and your future endeavors.

I owe immense gratitude to **Heleen** for her tireless support, even on her tough days. **Etty**, your strength is truly admirable, and I'm grateful to have been a witness to it. Conversations with you, be it about life or boxing, have been a highlight. To **Anita** and **Lidewij**, I trust you're doing an excellent job, and I wish you all the best. **Marije**, thank you for allowing me to be part of the Open Day event and for all the support in the days after I joined the department.

The Dream Team, also known as The **NanoOptics group**, has been my pillar of support. **Thomas**, I consider myself fortunate to have you as my mentor, and I owe a lot of who I am as a scientist to you. I am incredibly grateful for the patience with which you answer my silly questions, and your openness and support in difficult times. We were put together to work on Phantom, but our common interests in Asian cuisine, love for Japan, and Gin will always be special to me. Starting in this group with you as my mentor gave me the

chance to achieve more than I could have on my own, and a great deal of this book is dedicated to you. **Felipe**, thank you for the laughter and camaraderie in the early years of my Ph.D. I miss your presence as both a colleague and a friend. I hope you're doing well. **Javi**, your passion for all burning and laser-related things has been truly inspiring, and I'm grateful for the moments we've shared. **Irina**, your outspokenness and your ability to navigate complex scenarios with ease have been a great support. Thanks for listening to my rants and offering your support, in your twisted scary way. **Nikhil**, your timing in passing on the project was impeccable, and it couldn't have been in a better place for me. Your warm welcome and support have left an indelible mark, and I'm immensely grateful to you. Even during your final days, you took the time to teach me about topological photonics; thank you for that! **Martin**, you've been an exceptional office mate, and I appreciate your beautiful pictures and the GitLab cheat sheet. **Fillipo**, thanks for taking the time to explain spin helicity and chirality as if I were a child. I wish you and Irina the best in your new chapter. **Aron**, your knowledge and passion for everything technical are inspiring. I wish you all the very best and hope to see you soon for drinks. **Thijs**, I always enjoyed your company and just sitting and chatting about random things during Friday borrels, or lunch table chats. You've seen some tough times but I'm certain you'll deliver an incredible thesis! **Daniel**, mentoring you has been a pleasure. Thanks for helping with proofreading the thesis. I'll miss our unfunny jokes and your hearty laughter. I have no doubt you'll excel in your future Ph.D. journey. The youngest member of the group, **Onima**, I wish you the best for the coming years. I am certain you'll do a great job. I had the privilege of witnessing two incredible master's student projects, and both individuals are doing remarkably well. **Di**, I hope you find your way back to academia; you have the potential to be an incredible scientist. **Margaret**, I wish you all the best in the Taminiau lab.

7

To the Bestest Menschen **Marc** and **Louis**. Marc, We started this together, and I am happy that our shared trauma turned into a friendship and, in some cases, a partner in crime. You are an amazing scientist, and your talents and love for physics have always been something I look up to (also because you're tall). You've taught me a lot at work, and I am always in awe of the crazy ideas you have, from wanting a fish to telling me all the interesting things about chess. I will always still blame you for the coffee spots in the lab. Thank you for introducing me to **Jessie**, who is such a kind and caring soul who always has the craziest stories from her work that I love listening to. **Luigi**, our first conversation about your broken finger in the mountains of Courchevel immediately told me I was going to be in this friendship for a very long time. I found in you my confidant and a dear friend, and I hope you find your way back to the flatlands in one piece without any stabs. I am lucky to have found a true contender who appreciates Dutch courage just as much as I do, and I can't wait to share one or two, or maybe more, soon.

The Kavli nanolab, one of the cleanest of all cleanrooms, has played a crucial role in my journey. I extend my gratitude to the staff tirelessly working to ensure its success. **Eugene**, thank you for bearing with me and always being ready with solutions to the unbeknownst problems. **Charles**, **Pauline**, **Marc**, **Arnoud**, **Bas**, **Hozanna**, **Roald**, all your hard work and dedication is deeply appreciated.

The *QN C&C* - In hindsight, we could've come up with a better name for ourselves. However, I think we've done an incredible job to ensure the department is a safer and

more collaborative space. **Gary**, I am inspired by your vigor and readiness to take on work and your conviction. Thank you, **Sonia**, your enthusiasm and ability to uplift others have been a source of positivity. I am grateful for your sincere interest in my well-being and the regular check-in visits to my office. You are an incredible source of inspiration for me. **Victoria**, **Lizzy**, **Jean-Paul**, **Maurits**, and **Maz**, I had an amazing time organizing some fun activities, and I am grateful for your company.

There are times that I still pass by work for lunch. It has nothing to do with the food trucks and everything to do with the incredible people I have the privilege of sharing a table with. This group especially became the one and only human contact during strenuous pandemic times. **Sabrya**, **Maarten**, **Samer**, **Chris**, **Philip**, **Yashoda**, I've always cherished our lunchtime conversations. **Abel**, also a big thank you for taking the time out to give a demo of lamella preparation. **Iacopo**, I know you appreciate the attention, so here's a special mention for you. Thank you for always inviting me for drinks and offering support during my job search. **Brecht**, you were so kind to me in Courchevel when you ensured I didn't feel lonely. Thank you for always meeting me with a smile and for your kind words. Thanks to my amazing office mates **Annick, Pim, and Kars** for enduring all the times I've forgotten to get my ID card or when the door didn't work. Thanks to **Matthijs, Sarwan, Mattias, Lukas, Laetitia, Rasa, Ulderico, Micheal, Chunwei, Yufan, Serhiy, Alex, Thierry**, and all the others in the department that I had some great times with. **Yaroslav**, thank you for always having your door open and for assisting me when I randomly entered your office seeking help. I appreciate your and **Toeno**'s efforts in organizing the werkbepsrekings. **Anne-Marije**, you've been the kindest and most heartwarming senior PhD I could have asked for. I'm thankful for our chats about blogs, social media, and how to navigate life as a PhD in the department. Thank you **Simon** for always being so kind to offer help, and those lifesaving SOI chips during times of dire need are gestures I won't forget. To my two invaluable mentors during my early years, starting with my previous office mate **Rob** – thank you for your support and for being the sole laughter at my jokes during the Veldhoven conference when nobody else dared to. **Moritz**, your incredible patience and willingness to guide me, even during your final days as a Ph.D., have been priceless. Thanks **Pim** for lending a helping hand, even during the chaotic times of COVID and holidays. **Liu**, a big shout out for introducing us to the most delectable restaurants. Those random corridor encounters and cheerful greetings will be greatly missed. Our pending Indian dinner still awaits, along with a whole lot of shared memories, **Gaia**, **Alex**, and **Nina**. I also extend my gratitude to **Alex, Yong, Jin, Xiong** for the memorable times spent. Your camaraderie added a wonderful touch to our journey together. We meet again in another country **Jan**. I'm excited to see you be part of such an amazing group; I'm certain you'll have a great time here. Prof. **Tom**, even though our taste in music is poles apart, I had an amazing time with you in Sziget, year after year. I can't wait for the next time we go again and I'm so proud of you! Through thick and thin, I've had the fortune of having these two beautiful souls around me. **Praanshu**, thank you for always being there for me. You know I love you, in and out. **Meenakshi**, you're the only reason Chandigarh was bearable for me. Thank you for all your love and care.

Journal club members - **Parsa**, we started as colleagues, and I'm delighted that you've become not only a close friend but also my first patient. I wish you all the very best for your thesis and look forward to witnessing your defense. To the young Ph.Ds, my heartfelt

wishes for a promising future. I hope you continue to uphold the integrity of the group in the years to come. **Emanuele**, I'll miss our delightful gossip breaks. **Chris**, never doubt your remarkable talent as a scientist; you're truly exceptional. **Jana**, you bring a breath of fresh air, and I'm excited about your journey. You've got this! To **Lorenzo**, it's been a pleasure getting to know you, and your passion for science is truly inspiring. **Belen** (with the beautiful **Bart**) and **Nicoletta**, even though we've recently crossed paths, it feels like you've already become an integral part of my life in Delft. I can't wait to see you both soon.

Now, the *Malakamazing*, an extraordinary group with unique personalities. **Jo**, you were my first friend here who embraced my quirks and added your own to the mix. **Stefano**, your passion for everything, be it science, cooking, or dancing, is truly inspiring. **Kostas**, despite our ups and downs, I'm glad we're still friends, and your intense passion for quantum computing and its potential to change the world continues to inspire me.

The family away from home - Those who know me have probably heard the word "Bebop" from me at least once. This place gave me my family away from home. It started from us being Boppers to you all becoming an enormous part of my life, one that I'm certain will stay with me for years to come. It all began with the OGs: **Raj**, thank you for being my khara khara sauda. **Deniz**, your self-discipline is inspiring. **GJ**, I admire your pun-making skills, and **Will**, thank you for introducing me to so many incredible people. **Stephan**, my favorite, I'm confident you'll excel in whatever you set your mind to. **Nicole**, my sister in a far, far away land, I am grateful for all the love and support you have for me. **Tina**, your grace and patience during difficult moments amaze me. Ladies' nights have become a must when I need a pick-me-up. **Quentin** NANCY! I'm always surprised by how similar we are, and I'm thrilled you made the effort to come to Delft and find friends in us. **Milan**, buddy! I'm so proud of the relentless and dedicated person you are. We are almost there! **Nina**, you are a force in the cleanroom, and I'm certain you'll do an excellent Ph.D. **Stefan**, your passion for all things science and your evident enjoyment of your work make you truly amazing at it. **Deepika**, **Naveena**, I'm delighted we found our way back to each other, and I hope we'll continue no matter what comes our way. **Kristie** and **Kate**, you are so far away, but the moments we shared together starting from a random meeting at Boterhuis, I won't forget. I hope we see each other soon! **Mitasha**, thank you for welcoming me into your home and treating me like your sister from day one. **Grazia** and **Francesco**, thanks to our common love for tasty food (and Luca) I had the opportunity of meeting you two. I wish both of you the very best for the future, wherever it may be! **Norman**, you and I have shared many moments, and I'm ever grateful for the love and respect you've shown me. Thank you for the bestest baby in the world.

The family that chose me - Everything I am, everything I achieve, and my sole reason for being here is thanks to you, **Mumma** and **Papa**. You shielded me from harm, and I'm grateful you chose me. I may not say it often, but I love you and aim to always make you proud. **Daddy ji**, there isn't a day that goes by when I don't thank you for always looking out for me. **Wadhawans**, you have no business loving me the way you do. I still stand by the fact that I am blessed to have three maa - **Nani Ma, Daisy Masi, and Neetu Masi**. My not-so-little babies, **Shourya, Suyash, Sachishth, and Biba**, I can't wait to witness the incredible people you will grow up to be. **Shatakshi**, thank you for being such an incredible and supportive sister.

It's important to realize that the presence of **Garlic** and **Juniper** in my life is a constant dose of serotonin, and even though they won't ever read this, they ought to be mentioned. **Luca**, through my best and worst days, you've stood by me, embracing all the craziness that comes with. I'm excited about our future together, and I'll just leave it at - Se so cos'è l'amore, è grazie a te.

—- Sonakshi Arora,
November 2023, Delft.